Probabilistic Modeling Approach to Crack Nucleation from Forging Flaws

Zur Erlangung des akademischen Grades eines
DOKTORS DER INGENIEURWISSENSCHAFTEN (Dr.-Ing.)

von der KIT-Fakultät für Maschinenbau des
Karlsruher Instituts für Technologie (KIT)
angenommene

DISSERTATION

von

MSc. Francesco Radaelli

Tag der mündlichen Prüfung: 25. Januar 2023
Hauptreferent: Prof. Dr. rer. nat. Peter Gumbsch
Korreferent: Prof. Dr.-Ing. habil. Volker Schulze

Abstract

The process of crack nucleation from forging flaws has barely been described in literature. In this work it has been thoroughly investigated through an extensive testing campaign and various modeling approaches. It is a continuation of the Probabilistic Fracture Mechanics (*ProbFM*) code, that enables a conservative risk assessment of large heavy duty gas turbines due to fatigue crack growth from inherent forging flaws.

The focus of the testing campaign was to characterize the typical forging flaws and to quantify the nucleation life due to cyclic loading of the material. The nucleation life is defined as the amount of load cycles needed to initiate a sharp crack from an initial flaw. This part of the life-cycle is normally ignored in design and conservatively assumed to equal zero cycles. From the experiments we know that this is not true and that often around 50 % of the lifetime is spend in the nucleation process after which the crack starts propagating.

The main objective of the research is to develop an effective modeling approach for quantifying the nucleation life of flaws under varying loading conditions. This approach must then be embedded in an engineering tool ready for the design of real life components. Three different approaches are presented, of which one was incorporated in *ProbFM*.

In the first approach, the flaw is modeled as an embedded ellipsoid within the matrix material using a Finite Element Method. The strain field around the ellipsoid resulting from the applied stresses and temperatures serves as input to the local probabilistic Low Cycle Fatigue (LCF) assessment. In this assessment the probability for crack initiation is computed as a surface integral of local hazard densities. The underlying model assumption is that the local LCF life is Weibull distributed.

The second and third approaches are based on a flaw modeled as a flat surface area. Also here the local probabilistic LCF life is computed and corrected with a life multiplication factor w in one case and with a stress concentration factor K_t in the other case.

The area-based model with the calibrated stress concentration factor fits best the experimental results and is the one proposed for implementation. Conservatism has been dealt with throughout the analysis in order to ensure a reliable model, fit for its engineering application.

The resulting model has been showcased in a reliability assessment of a real life rotor disk design. The obtained probabilities of failure are lower when including the nucleation life and the components design life can potentially be extended.

Zusammenfassung

Der Prozess der Rissbildung aus Schmiedefehlern ist in der Literatur kaum beschrieben. In dieser Arbeit wurde dies durch umfangreiche Experimente und verschiedene Modellierungsansätze gründlich untersucht. Sie ist eine Fortsetzung des Probabilistic Fracture Mechanics (ProbFM) Projektes, welches eine konservative Bewertung des Versagensrisikos basierend auf dem Wachstum von Ermüdungsrissen aus inhärenten Schmiedefehlern in großen Hochleistungsgasturbinen ermöglicht.

Der Fokus der Versuchsreihe lag auf der Charakterisierung von typischen Schmiedefehlern und der Quantifizierung der Nukleationslebensdauer durch zyklische Belastung des Materials. Die Nukleationslebensdauer wurde definiert als die Anzahl der Belastungszyklen, die erforderlich sind, um einen scharfen Riss aus einem anfänglichen Fehler zu erzeugen. Dieser Teil des Lebenszyklus wird normalerweise beim Design ignoriert und konservativ gleich null Zyklen angenommen. Aus den Experimenten wissen wir, dass dies nicht stimmt und dass oft etwa 50 % der Lebensdauer auf den Nukleationsprozess entfallen.

Das Hauptziel der Untersuchungen ist die Entwicklung eines effektiven Modellierungsansatzes zur Quantifizierung der Nukleationslebensdauer von Fehlern unter variierenden Belastungsbedingungen. Dieser Ansatz muss dann in ein Engineering-Tool eingebettet werden, welches zum Design realer Komponenten verwendet wird. Es wurden drei verschiedene Modellierungsansätze untersucht, von denen einer in ProbFM implementiert wurde.

Im ersten Ansatz wird der Fehler als eingebettetes Ellipsoid innerhalb des Matrixmaterials mit einer Finite-Elemente-Methode modelliert. Das Dehnungsfeld um das Ellipsoid, das sich aus den angelegten Spannungen und Temperaturen ergibt, dient als Eingabe für die lokale probabilistische LCF Bewertung. Bei dieser Bewertung wird die Wahrscheinlichkeit für Rissbildung als Oberflächenintegral der lokalen Hazarddichte berechnet. Die zugrunde liegende Modellannahme ist, dass die lokale LCF-Lebensdauer Weibull verteilt ist.

Der zweite und dritte Versuch basieren auf der Annahme eines Fehlers, der als flacher Oberflächenbereich modelliert ist. Auch hier wird die lokale probabilistische LCF-Lebensdauer berechnet und, in einem Fall, mit einem Lebensdauermultiplikationsfaktor w und, in dem anderen Fall, mit einem Spannungskonzentrationsfaktor K_t korrigiert.

Das flächenbasierte Modell mit dem kalibrierten Spannungskonzentrationsfaktor passt am besten zu den experimentellen Ergebnissen und wird zur Implementierung vorgeschlagen. Der Konservatismus wurde während der gesamten Analyse berücksichtigt, um ein zuverlässiges Modell zu gewährleisten, das für eine technische Anwen-

dung geeignet ist.

Das resultierende Modell wurde in einer Zuverlässigkeitsbewertung eines realen Rotorscheibendesigns vorgestellt. Die erhaltenen Ausfallwahrscheinlichkeiten sind geringer, wenn die Nukleationslebensdauer berücksichtigt wird, und die Lebensdauer der Komponenten kann potenziell verlängert werden.

Acknowledgments

This thesis is the result of my work as Doctoral candidate at the Institute of Applied Materials at the Karlsruhe Institute of Technology from July 2017 until April 2022. It would not have been possible without the support of many people that crossed my way, or accompanied me along it.

I would like to thank my supervising professor Peter Gumbsch, for his important advice and suggestions throughout the research.

During this time I have been working at Siemens Energy in the department of Probabilistic Design. My special thanks and gratitude go to my supervisors Christian Amann and Kai Kadau for their continuous support, advice, collaboration and friendship. I would also like to thank the entire team of researchers, fellow PhD candidates and all the other experts at Siemens for many fruitful discussions, cool projects and exciting coffee talks. Naming them all would be long, naming few would be too short!

I also worked in strong collaboration with our Fraunhofer IWM partners in Freiburg. Thank you Igor Varfolomeev and Ali Aydin, together with all the nice researchers I had the chance to meet in Freiburg!

Finally, and most importantly I thank my wife and children for being there, always. I dedicate this work to them.

Publications and Intellectual Property

Publications

- Radaelli, F., Kadau, K., Amann, C., and Gumbsch, P. Probabilistic fracture mechanics framework including crack nucleation of rotor forging flaws. In *Proceedings of ASME Turbo Expo 2019*, pages GT2019–90418, 2019. doi:10.1115/GT2019-90418
- Radaelli, F., Amann, C., Aydin, A., Varfolomeev, I., Gumbsch, P., and Kadau, K. A probabilistic model for forging flaw crack nucleation processes. *Journal of Engineering for Gas Turbines and Power*, 143(10):185, 2021. ISSN 0742-4795. doi:10.1115/1.4051426
- Radaelli, F., Amann, C., Aydin, A., Varfolomeev, I., Gumbsch, P., and Kadau, K. A probabilistic model for forging flaw crack nucleation processes for heavy duty gas turbine rotor operations. In *Proceedings of ASME Turbo Expo 2022*, pages GT2020–14606, 2022
- Rezaul Karim, M., Kadau, K., Narasimhachary, S., Radaelli, F., Amann, C., Dayal, K., Silling, S., and Germann, T. C. Crack nucleation at forging flaws studied by non-local peridynamics simulations. *Mathematics and Mechanics of Solids*, 1961:108128652110572, 2021. ISSN 1081-2865. doi:10.1177/10812865211057211
- Rezaul Karim, M., Kadau, K., Narasimhachary, S., Radaelli, F., Amann, C., Dayal, K., Silling, S., and Germann, T. C. Crack nucleation from non-metallic inclusions in aluminum alloys described by peridynamics simulations. *International Journal of Fatigue*, 153:106475, 2021. ISSN 01421123. doi:10.1016/j.ijfatigue.2021.106475

Intellectual Property

- Radaelli, F., Amann, C., Kadau, K., Schmitz, S., and Vöse, M. Computer-implemented method for the probabilistic estimation of a probability of failure of a component, a data processing system, a computer program product

and a computer-readable storage medium, 2019. URL patentscope.wipo.int/search/en/detail.jsf?docId=WO2020089402. Patent WO/2020/089402

Contents

List of Figures

List of Tables

Nomenclature

Latin Symbols

ΔK	Stress intensity range	$[\,\mathrm{MPa}\sqrt{\mathrm{m}}\,]$
$\frac{da}{dN}$	Crack growth rate	$[\,\mathrm{m/cycle}\,]$
$\hat{l}(\theta \mid x_1, \ldots, x_n)$	Log likelihood estimation for parameter θ, conditional to observing $x_1, \ldots, x_n$	
a	Semi-minor axis of the crack	$[\,\mathrm{m}\,]$
A_j	Surface partition	$[\,\mathrm{m}^2\,]$
A_{cs}	Cross-sectional area of the ellipsoid in the xy-plane or measured area of the flaw on the fracture surface	$[\,\mathrm{m}^2\,]$
b	Fatigue strength exponent of the CMB equation	
C	Paris parameter	
c	Fatigue ductility exponent of the CMB equation	
c	Semi-major axis of the crack	$[\,\mathrm{m}\,]$
d	Distance to the surface	$[\,\mathrm{m}\,]$
E	Young's modulus	$[\,\mathrm{MPa}\,]$
h	Hazard rate, probability of crack initiation within the next cycle	
$H(n)$	Cumulative hazard function	
K	Plastic hardening parameter of the Ramberg-Osgood equation	
k	Total amount of integration points on surface $\partial\Omega$	
k	Ultrasonic flaw size conversion factor	
K_t	Stress concentration factor	

K_{cr}	Critical toughness limit	[MPa$\sqrt{\text{m}}$]
K_{Ic}	Mode I fracture toughness	[MPa$\sqrt{\text{m}}$]
m	Paris exponent	
m	Weibull shape parameter	
m_{eff}	Effective Weibull shape parameter	
N	Number of cycles	[cycles]
n	Plastic hardening parameter of the Ramberg-Osgood equation	
N_F	Number of cycles to failure	[cycles]
N_i	Number of cycles to crack initiation	[cycles]
N_p	Number of cycles in crack propagation life	[cycles]
N_{calc}	Calculated number of cycles to failure	[cycles]
N_{flaw}	Number of cycles in the lifetime of a flaw	[cycles]
N_{FM}	Number of fracture mechanics cycles of a flaw	[cycles]
$N_{i,1\text{mm}^2}$	Number of cycles to crack initiation for a 1 mm^2 equivalent flaw	[cycles]
$N_{i_{det}}$	Deterministic number of cycles to crack initiation	[cycles]
N_{inc}	Number of cycles of incubation	[cycles]
N_{LC}	Number of cycles to a long crack	[cycles]
N_{MSC}	Number of cycles to a microstructurally small crack	[cycles]
N_{Nuc}	Number of nucleation cycles of a flaw	[cycles]
N_{PSC}	Number of cycles to a physically small crack	[cycles]
N_{test}	Observed number of cycles to failure	[cycles]
P_{SWT}	Smith, Watson and Topper parameter	[MPa]
R	Load ratio ($R = \sigma_{min}/\sigma_{max}$)	
r_1,r_2	Major and minor radii of ellipse	[m]

r_x,r_y,r_z	x-,y- and z-radii of the ellipsoid used to model a forging flaw	[m]
S	Total number of simulated MC samples	
T	Temperature	[℃]
T_1	Temperature 1 ($> T_{RT}$)	[℃]
T_2	Temperature 2 ($> T_1$)	[℃]
T_{RT}	Room temperature (≈ 25℃)	[℃]
V_{comp}	Volume of a component	[m^3]
w	Life correction factor	
x_i	Observed amount of nucleation cycles for a specific flaw	
Y	Geometry factor	

Greek Symbols

α	Orientation angle of ellipse or rectangle	[deg]
$\Delta\sigma$	Stress range	[MPa]
η	Weibull scale parameter	[cycles]
η_{eff}	Effective Weibull scale parameter	[cycles]
$\partial\Omega$	Boundary surface	[m^2]
$\rho(n;\varepsilon_a(\mathbf{x}),T(\mathbf{x}))$	Local hazard density for crack initiation	
ρ_{all}	Volume flaw density	[$1/m^3$]
σ	Stress	[MPa]
σ'_f	Fatigue strength coefficient of the CMB equation	[MPa]
σ_a	Stress amplitude	[MPa]
σ_m	Mean stress	[MPa]
σ_y	Yield stress	[MPa]
σ_{max}	Maximum applied uni-axial stress on a specimen or flaw	[MPa]

$\sigma_{membrane}$	Membrane stress or uni-axial load applied as boundary condition	[MPa]
σ_{min}	Minimum applied uni-axial stress on a specimen or flaw	[MPa]
σ_{vm}	Von Mises stress	[MPa]
θ	Parameter to be optimized with the MLE	
ε	Strain	[m/m]
ε'_f	Fatigue ductility coefficient of the CMB equation	[m/m]
ε_a	Strain amplitude	[m/m]

Abbreviations

AM	Additive Manufacturing
BSE	Backscattered Electrons
CMB	Coffin-Manson-Basquin
CT	Compact Tension
DARWIN	Design Assessment of Reliability with Inspection
EBSD	Electron Backscatter Diffraction
ECDF	Empirical Cumulative Distribution Function
EDX	Energy Dispersive X-ray Spectroscopy
FAD	Failure Assessment Diagram
FEA	Finite Element Analysis
FEM	Finite Element Method
HPC	High Performance Computing
IWM	Fraunhofer-Institut für Werkstoffmechanik
KSR	Disk shaped reflecor, from German *Kreisscheibenreflektor*
LCF	Low Cycle Fatigue
LEFM	Linear Eleastic Fracture Mechanics

MC Monte Carlo

MLE Maximum Likelihood Estimation

MPI Magnetic Particle Inspection

NDT Non-Destructive Testing

NMI Non-Metallic Inclusion

PoD Probability of Detection

PoF Probability of Failure

ProbFM Probabilistic Fracture Mechanics High-Performance Computing Methodology and Tool

RT Room Temperature

SAFT Synthetic Aperture Focusing Technique

SE Secondary Electrons

SEM Scanning Electron Microscopy

SIF Stress Intensity Factor

TFS True Flaw Size

UT Ultrasonic Testing

XCT X-ray Computed Tomography

1. Introduction

An important challenge in designing engineering components is data uncertainty, data scatter, or even the lack of data. Be it uncertainty at the loading side: varying loading profiles, different boundary conditions, temperature etc., or be it at the material side: scatter in strength, resistance, component geometry or material imperfections. No component is identical, nor is the loading condition on that component. In the increasingly volatile energy market, focusing on flexible, heterogeneous, decentralized, and efficient energy production, gas turbines need to adapt accordingly. One major challenge is to design gas turbines for the increasing number of start-stop and intermediate cycles. The development and application of reliable lifetime assessment methodology and tools for critical components, such as rotor disks, can support the reliable application of gas turbines in this emerging energy landscape.

Heavy-duty gas turbines, especially if in a combined cycle configuration, can reach efficiencies above 63% and an output of almost 600 MW. The working principle of gas turbines is the Brayton thermodynamic cycle. Fresh air is introduced in a compressor, where it is pressurized. Then it runs in a combustion chamber where the air is heated. The hot air expands and brings the turbine blades in motion — this same torque also moves the compressor blades and the generator rotor, producing electricity. The heat is released in the atmosphere — or, in case of a combined cycle configuration, it is used to drive a steam turbine. Raising the turbine inlet temperature or its pressure, increases the thermal efficiency. Blades and vanes are subjected to maximum temperatures of more than 1000 ℃. They are normally superalloy castings with a protective coat and eventually even bore-holes for cooling air. Rotor disks are typically produced as large steel forgings and are not coated; they reach temperatures of up to 500 ℃. Figure 1.1a illustrates a gas turbine rotor assembly with a stack of 13 compressor disks before the combustion chamber and 4 turbine disks in the hot part. The forged rotor disk arrives in a pre-machined state at the shop floor where it is machined to its end-contour, see Figure 1.1b. The disks have diameters ranging from 1 to 2 m and weight several tonnes. In most countries engines are operated at 50 Hz, a handful (e.g. Brazil, US, Saudi Arabia and Taiwan) use 60 Hz. Depending on the application, the disks are forged from different steel materials. For disks with a central hole in it, the principal loads are the hoop stresses which consist of tension in tangential direction, which may locally approach the yield stress.

Figure 1.1.: (a) Assembly of the SGT5-8000H at the Siemens Energy gas turbine plant in Berlin. (b) A worker with a finished disk for a gas turbine. With permission by Siemens Energy.

1.1. Forging Flaws

Unavoidable flaws in forged rotor components are particularly challenging to describe with engineering methods. Figure 1.2 shows a Scanning Electron Microscopy (SEM) image of a flaw on a fracture surface of a specimen. Such flaws do not occur often and are normally so small that they are not relevant for design. But, when they are large enough and positioned in critically loaded regions, they can nucleate into cracks and further grow incrementally after each load change of the machine. Once the crack reaches a critical length, the large centrifugal forces in the disk make it expand rapidly until burst occurs. Severe asset losses and even fatalities may follow from such accidents. Accidents such as in Irsching, Germany, in 1987 are caused by crack initiation from undetected forging flaws, see Figure 1.3. This flaw was almost the size of a palm of a hand and located in the center of the 28NiCrMoV 85 rotor. It was a large void, probably originated as secondary shrinkage in radial orientation, which could not be detected with the ultrasonic testing (UT) procedures of that time. During 15 years of operation, 728 warm starts and 110 cold starts, the flaw nucleated, further propagated and led to failure of the entire engine. Two smaller fragments of about 1 ton flew a distance of more than one kilometer [2]. The fact that such a large flaw did not lead to burst earlier, speaks for the significance of its nucleation life, i.e. the time it needed to develop a sharp, growing crack. Mayer et al. [49] reported over 15 rotor burst in the last century caused by forging defects and others are documented by Nakao [57; 58], Nitta et al. [60; 61] or by the U.S. NTSB [97; 98].

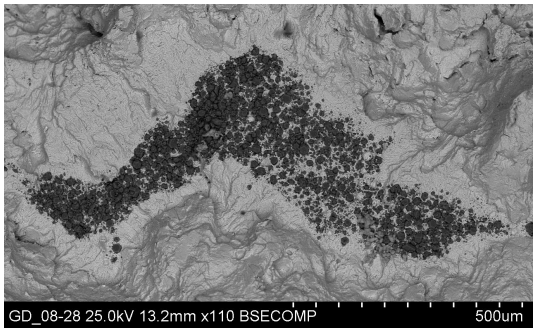

Figure 1.2.: SEM image of a forging flaw on the fracture surface of a specimen.

Figure 1.3.: Fragment of Irsching burst steam turbine rotor. There were no fatalities [2].

Such accidents increased the awareness of the need to investigate on forging flaws and to develop tools enabling engineers to safely design engineering components. Ever since, UT methods have been refined and improved. Rotor disks, e.g., are scanned from all the surfaces and in several directions in an automatic fashion. This increases the probability of detection (PoD) of flaws at all locations of the disk (both near the inner hole and near the outer surface) and in all orientations. New methods such as the Synthetic Aperture Focusing Technique (SAFT), already applied in medical ultrasonics, are taking off also in the field of heavy machinery. Zimmer et al. [111] presented a review of the changes in testing procedures at one of the major rotor forgings manufacturers in Germany, Saarschmiede GmbH. Figure 1.4 shows the rough surface of the pancake shaped disk after forging and heat treatment (left). It is then polished into a smooth geometry, suitable for extensive UT inspection (center). After UT it is further machined into a rough contoured shape (right).

Also from the manufacturing side things have improved. Forging large components remains a matter of manual craftsmanship. In the melting process impurities, such as oxides can be introduced in the material. The process can be optimized such to reduce them or they can be crashed into smaller (insignificant) particles during the forging procedure. In general we refer to all kind of imperfections found in forged components as 'forging flaws', which is not completely fair w.r.t. the smith, since impurities are not introduced during forging — where they are rather reduced — but in the casting process. Nevertheless, we will consequently refer to them as 'forging flaws' in this thesis. In effect, if the forging process is not properly balanced (e.g. the workpiece gets too cold), shear stresses may cause rupture of the matrix material. Such discontinuities, or separations, would be 'forging flaws' in the true sense of the word. A good overview of the different typologies of flaws is given by Vrana et al. [101]. Many of them are significantly reduced by optimizing all the involved steel-making

Figure 1.4.: Heavy-duty gas turbine rotor disk forgings at different manufacturing stages: after forging and heat treatment (left), ultrasonic contour (middle), rough machining contour (right). From Zimmer et al. [111].

processes, increasing the overall quality of the final products.

1.2. Fracture Mechanics

Yet, there are still flaws present in forgings, some of which are detected by UT and others which are not. Since the flaw cannot be removed, if the indication exceeds a set criterion, the entire forging is discarded. This minimizes the presence of large flaws in the accepted components, but even this small eventuality must be accounted for in design by describing the entire failure mechanism. Normally the flaws are considered as sharp cracks and modeled by Linear Elastic Fracture Mechanics (LEFM), with some extensions to account for plasticity effects. A stress intensity factor range at the crack tip drives the Paris law equation where the grack growth rate per cycle, $\frac{da}{dN}$, is computed. Longer cracks have higher stress intensities, which in turn result in higher growth rates. This iterative process — which is a differential equation, discretized per cycle — is repeated until the intensity factor reaches the material's fracture toughness, K_{Ic}, and the material fails. LEFM has been long applied on forging flaws, see e.g. [10; 31; 62; 80].

In the late 1980s and 1990s it was acknowledged that the rare occurrence of manufacturing anomalies in titanium forged aero-engine rotor disks cannot be designed for in a deterministic, or so called safe-life approach. Consequently, a probabilistic fracture mechanics approach was developed by the aero-engine community, including the Federal Aviation Administration, in the early 1990s to address rare anomalies in such disks [96]. Southwest Research Institute collaborated with the aero-engine community to implement the methodology and software tool called DARWIN (Design Assessment of Reliability with Inspection) [18; 22–24]. Also for other applications, such as nuclear reactor pressure vessels, probabilistic fracture mechanics methodologies have

been developed, see Chapter 4 in [25].

In the last decade Siemens Energy developed *ProbFM*, which is a probabilistic fracture mechanics high-performance computing methodology and tool [4–7; 38; 39; 102]. This tool was specifically designed for stationary heavy-duty gas turbine rotors in the energy sector. It utilizes very efficiently parallel computing platforms with thousands of CPUs or GPUs to solve direct simulation Monte Carlo (MC) schemes involving up to billions of individual fatigue crack growth simulations. Depending on the problem size and involved number of processors the numerical solution can be obtained within minutes, even on state-of-the-art engineering workstations.

1.3. Crack Nucleation

All the above mentioned methods apply LEFM under the assumption that the flaw is an initiated crack with a dimension that can be deduced from UT. Considering only the crack propagation phase is a conservative approach, because flaws are not immediately initiated cracks, as they first go through a crack nucleation phase. The significance of this nucleation phase has been demonstrated by low cycle fatigue (LCF) tests of specimens including forging flaws [99]. The crack nucleation life is found to be a significant fraction of the total life until specimen failure. This was already recognized by Scarlin et al. [80], where it was referred to as 'incubation time'; it was, however, never quantified as such.

Since advanced designs and higher temperatures increase demand on material life and capability, also the engineering methods need to be revised and conservatisms reliably reduced. Adding the crack nucleation life to the already captured propagation life offers a good opportunity to fulfill those needs.

In this thesis, I present a model which quantifies the nucleation life in which a forging flaw develops into a sharp, initiated crack, as already presented in [69–71]. Experiments were conducted on 56 specimens taken from large forgings including flaws as detected by UT. Based on a thorough analysis of the fracture surfaces of those defective specimens, geometrical and chemical features of the flaws could be understood. By alternating the cyclic loads on the specimens in high amplitude and low amplitude loading blocks, beach marks were formed on the fracture surface. They are used as a means for back-tracing the amount of cycles contributing to crack propagation and determining the amount of cycles till crack initiation; similar as to counting annual rings of wood growth in trees.

The observed amount of load cycles for nucleation put the basis for the model. Since there is a strong correlation between load amplitude, temperature and especially flaw size, we looked into an approach where the statistical size effect could be accounted

for: a small area with given stress amplitudes should be less likely to initiate a crack than its larger counterpart at the same number of cycles. We postulated that the local probabilistic LCF approach developed by Schmitz et al. [46; 82–85], intended for component design, may also be used for quantifying the crack initiation rate within a forging flaw. Based on the morphology of the flaws and the observed amount of cycles until crack nucleation several models have been calibrated using the Maximum Likelihood Estimation (MLE) method.

The obtained calibrated model has been embedded in the above mentioned *ProbFM* engineering tool. The results and implications are evaluated in order to better quantify the reliable lifetime of these critical components.

2. Background and Theory

In this chapter I present some elements of theory needed to better understand the modeling approach proposed to describe the nucleation of forging flaws. It goes from understanding micro-mechanical properties of materials, how the forging process takes place, what has to be considered in UT, how is nucleation modeled at present, what are the fundamentals behind *ProbFM* and also how the local probabilistic LCF approach works, which puts the basis for the proposed nucleation models.

2.1. Forging Process

Rotor disks of large gas turbines are manufactured in an open die forging process. This is one of the world oldest metalworking processes. The several steps are schematically illustrated in Figure 2.1. The melted material is cast into a large ingot to chemical composition. Before forging, the ingot is often remelt, in order to reduce impurities such as Non-metallic inclusions (NMI) from the mold walls. Sometimes, if the ingot is a long cylinder, it is cut into disks. They are then forged using a die and a hammer. During forging, the workpiece goes repeatedly back into the oven, in order to keep it within the forging temperature range. After final deformation, it is quenched and tempered, to achieve martensitic transformation. This series of processes ensures hardening of the steel by creating contoured grain flow and fine microstructures with small grain sizes that could otherwise not be achieved in castings, where grains are not mechanically altered.

In the casting process, impurities may end up into the ingot. Oxides and ceramic inclusions are typical, but also chemical segregation, ingot pipes, porosity or high hydrogen content. The majority of those imperfections can be avoided or reduced by proper ingot dimensioning, controlled pouring and casting. E.g., a large part of the slag is removed from the mold in liquid state since the larger pieces float to the surface. While the ingot cools down from the outside and grains are progressively formed, residual dirt is transported to the center. The temperature gradient also causes thermal tension stresses at the center, which produce porosity.

During forging the defects are smashed and teared apart with shear stresses and porosity is consolidated. The remelt operation also ensures that the clusters of smashed particles spread and dissipate. At the other hand, while the workpiece is

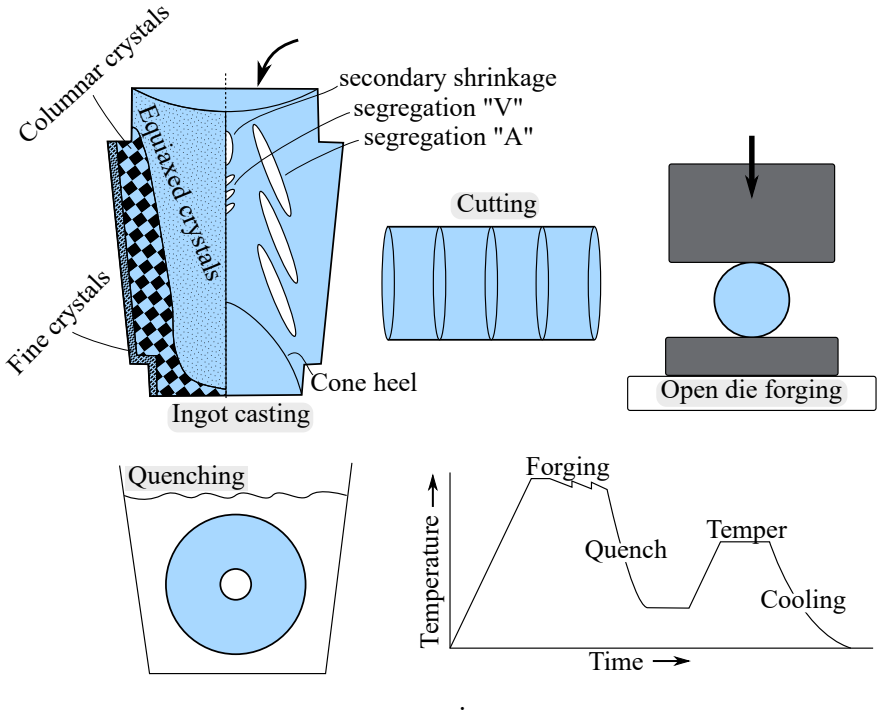

Figure 2.1.: Several processes involved in the production of foged components: ingot casting, eventually cutting, forging, quenching and heat treatment. The temperature plays a key role and needs to be controlled at all time of the process. During forging the workpiece may be repeatedly put in the oven to increase its forgeability.

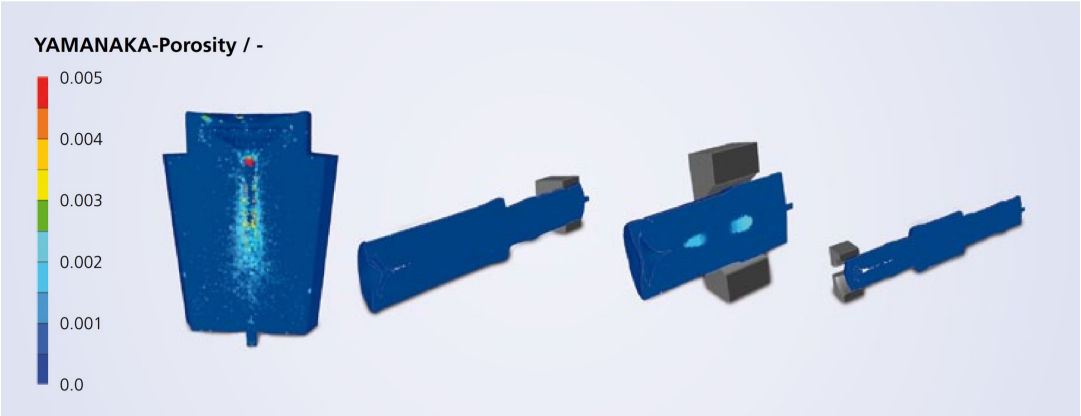

.

Figure 2.2.: Example of a linked casting with forging simulation where porosities are followed within a 1.6 ton ingot during stretching operations.[100]

getting colder, and mechanical shear stresses tear the steel apart, separations due to lack of fusion may appear near the surface. This delicate balancing and optimization of the microstructure in the matrix material and minimizing the presence of detrimental flaws requires a lot of know-how. With specialized software the workpiece is modeled and both the casting and the forging processes are simulated in sequence in order to trace flow lines in the grain structure and analyze the segregation behavior while the workpiece is stretched and deformed in changing temperature and stress gradients. Typical segregations are shrinkage cavities at the top of the ingot and the already mentioned centerline porosity and carbon segregation. A good example of how the forging processes can be simulated sequentially is described in [100], where Figure 2.2 is taken from. The figure shows how the stretching process helps removing centerline porosity. Disks with a central tie bold design are finally pierced, in order to create the central hole. This procedure also helps removing large part of the defects around the centerline.

Despite major improvements in the manufacturing process by forges and all the efforts being made to grant a high quality standard, there is still a probability to have manufacturing defects within the forging which is inherent to its production process. NMIs can be reduced and dissipated, but not completely avoided. Inclusions in finished forgings can be single, compact indications or even groups of inclusions (probably originating from one larger single inclusion). Often they are idealized as circles or ellipses, but in reality they have random shapes, see Figure 2.3. From the left figure it becomes clear how the flow lines of the casting and forging processes play a significant role also in deforming and dissipating flaws; the flaw looks basically like

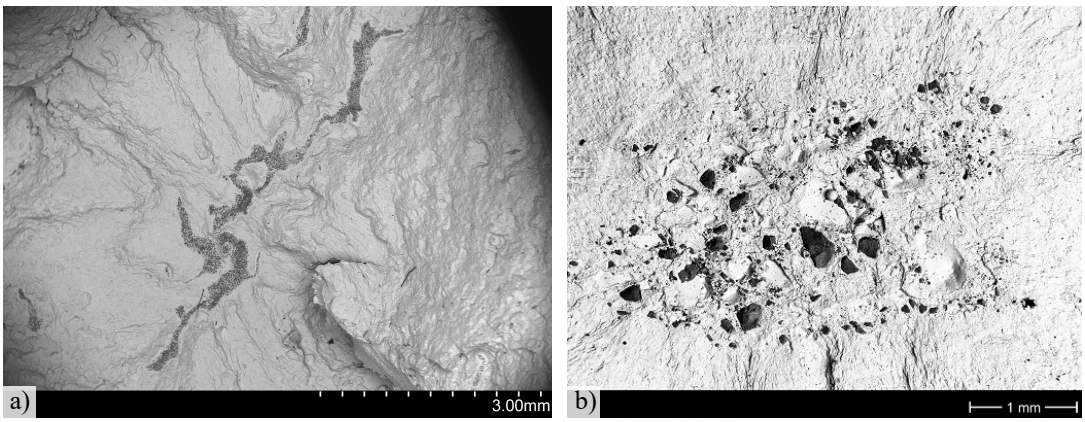

Figure 2.3.: SEM images of flaws on the fracture surface of specimens from different forging procedures resulting in different fragmentation and dissipation of the particles. (a) An elongated NMI with highly fragmented and dissipated particles. (b) A sparsely packed cluster with relative large, poorly fragmented particles.

a dissolved particle in a viscous liquid. The right figure shows a flaw from a different forging procedure, where the larger millimeter sized flake is only poorly fragmented into rather large sparsely packed particles. The exact fragmentation depends on the specifications of the forging process including the temperature and applied stresses. The chemical composition of inclusions depends a lot of the used steel material. They may originate externally, from the surface of the ingot mold or dust in the workshop that reacts with oxygen and creates oxides, or internally, due to inhomogeneities in the crystallization process or from deoxidation of slag, see Rathi et al. [73] for a brief overview. Typical types of inclusions are alumino silicas, Al_2O_3, MnS, MgO, CaO or (MnCa)S particles [62][10]. By looking at the processes in real life, one could actually wonder how only so little defects exist!

2.2. Ultrasonic Inspection

A rotor disk in its final shape (with blade attachments, cooling holes etc.) has a complex geometry with many edges, holes and curvatures. Inspecting it with UT is often not practicable and especially not reliable to find volumetric indications. Eventual indications near boreholes and other edges may be overlooked. For this reason quality control requires the disks to be tested in their totality before they are machined. They are in the so-called pancake shape and therefore much easier to inspect and, more importantly, it is less probable to overlook significant flaws. In addition, it is cheaper to scrap a disk in this production state than in the final shape. Flaws can potentially be located in all parts of the component and in all orientations.

In order to increase the probability to detect them, the UT must be planned in a way that the component is examined from different directions, such that at least one of them gets the ultrasound wave reflected properly. This entire procedure is normally automated and takes place at the forge before the material is shipped. If some flaws are detected, one could consider to still purchase the piece and machine the component such that the flaw would end-up being machined-out of the final shape or located in a mildly loaded area of the component, where crack growth is negligible.

UT inspection strategies for large forgings used in the energy sector are documented by Schwant and Timo [87; 88], Jestrich et al. [35], Heinrich et al. [31], Mayer et al. [48–50] and more recently resumed by Zimmer et al. [111]. These authors focused mainly on how to improve the inspection methods to reliably find forging flaws and propose ways to relate the observed indication to true flaw sizes (TFS), which serve as input for the fracture mechanical calculations.

Raw data from UT signals is translated into a so-called disk shaped reflector size or KSR (from the German *Kreisscheibenreflektor*). This is an effective measure that compares the echoed signal from a flaw with a preset calibration signal from a disk shaped reflector. The discrepancy between this value and the TFS has been studied by Kern et al. [40]. The TFS is referred to as WEFG (from the German *Wahre Ersatz Fehler Größe*). A correction factor, k, based on his findings can be defined as:

$$k = \frac{TFS}{KSR} \tag{2.1}$$

Using UT simulation software, the physical testing is simulated on a large amount of flaw samples with different locations, shapes and orientations. Based on this type of simulations we are able to define a PoD for a given testing setup, which may vary in signal frequency, angle of incidence, different scanning faces etc. Guan et al. [29] described how this approach can be embedded into a probabilistic framework for structural integrity assessments. Applying a PoD implies that one may expect flaws to be present in the component even if they were not observed. The PoD is size dependent: small flaws have small PoD's and large flaws have PoD values close to one. The thorougher the inspection strategy, the higher the PoD values in general. This entire procedure is concisely described by Vrana et al. [102]. Observed KSR sizes, KSR_{obs}, are transformed into TFS_{obs} using k. The expected TFS, TFS_{exp}, is obtained by dividing TFS_{obs} over the PoD. TFS_{exp} can than be used for the integrity assessment.

In recent years there have been studies on the application of SAFT in large forged components. This technique is basically reducing random noise by combining the signals from different scans. It improves the sizing of indications, defect localization

and the separation of close defects (group indications). The component's volume is split into voxels and, by superposition of echo signals from several scan positions, a local response amplitude is calculated. Experience of Siemens Energy's newly developed SAFT software applied to forgings at Saarschmiede confirms these benefits as reported by Mooshofer et al. [54; 55; 86; 103; 104]. This state-of-the-art inspection procedure is already implemented for new design turbines.

On specimen scale, it would be useful to perform also X-ray computed tomography (XCT) testing on flaws. This has been reported by Naragani et al. [59] for inclusions in Ni-based superalloys. Using high energy synchrotron x-rays, a full 3D characterization of the flaw was obtained. For the steels used within this thesis, it might be problematic to obtain high resolution XCT images, due to the high density of the steel. Nevertheless, it has been tried to perform some tests at different institutes on very small specimens (ca. 2 mm diameter) with forging flaws, eroded from the fracture surface of previously tested material. Unfortunately, these tests were not successful. This testing procedure can obviously not be applied on component scale.

2.3. Fatigue

The focus of this study is to describe the main structural failure mechanism that originates from forging flaws. When the component is loaded, the flaws work as stress enhancers as they locally influence the redistribution of the stress flow in comparison to a situation without a flaw. When cyclically loaded, those stress hot-spots induce fatigue, which is a century old problem in steel components. In the middle of the nineteenth century steel bridges and railway components failed under repeated loading. The German railway engineer, August Wöhler, developed a method correlating the fatigue lifetime — expressed in number of load cycles — to the stress range of the applied alternating load, often referred to as SN-curve or Wöhler curve. He also introduced the concept of endurance limit. His method was further refined in order to correlate the lifetime, N, to the (plastic) strain, ε, and also to account for mean stress effects. Fatigue has been divided into high cycle fatigue, which is mainly driven by small, elastic strain amplitudes at high amount of cycles (about $10^4 - 10^8$ load cycles), and low cycle fatigue, which is driven by plastic deformation and smaller amount of cycles (below 10^4). Today the Wöhler curve is often described by the plastic model of Coffin and Manson [17; 47] combined to the elastic model of Basquin, which goes by the name Coffin-Manson-Basquin (CMB) equation. It relates the number of cycles until crack initiation N_i to the strain amplitude ε_a in the log-log scale:

$$\varepsilon_a = \frac{\sigma'_f}{E}(2N_i)^b + \varepsilon'_f(2N_i)^c \tag{2.2}$$

where the parameters σ'_f and ε'_f are called fatigue strength and ductility coefficients and b and c are fatigue strength and ductility exponents. There are several ways to include the mean stress effect to the fatigue life. The approach used in this thesis, also known as the modified Morrow approach, also accounts for the mean stress σ_m. It was proposed by Socie et al. [92] with the following strain-life equation:

$$\varepsilon_a = \frac{\sigma'_f - \sigma_m}{E}(2N_i)^b + \varepsilon'_f(2N_i)^c \tag{2.3}$$

At this point we need to make a distinction between the different stages of the fatigue crack growth. Generally a microcrack initiation stage is separated by the macrocrack propagation phase. This separation is not based on physics based concepts, it is more of a practical approach. The limitations of detecting initiated cracks using Non-Destructive Testing (NDT) often sets a lower limit to the definition of crack initiation life in specimens. Cracks smaller than ca. 1 mm are not easily detected. The fatigue life of smooth specimens is defined by the amount of cycles needed until a crack of a certain length is detected or until the stress amplitude drops below a certain level. At the other hand also the crack propagation stage has its limitations. LEFM assumptions do not apply below the millimeter size in most materials. Global isotropic material properties in steels are not given at local microstructural level; only at larger scale we can apply continuum-based fracture mechanics models to bulk properties. In practice this all comes down to the stress intensity factor concept, which defines the stress situation at the crack tip. Paris and Erdogan [63] developed an empirical crack growth equation based on the stress intensity range, ΔK:

$$\frac{da}{dN} = C\Delta K^m \tag{2.4}$$

where $\frac{da}{dN}$ is the crack growth rate and C and m are calibrated material parameters. The stress intensity range depends on the applied stress and temperature, but also on the actual crack length a; this turns Eq. (2.4) into a differential equation discretized in cycles.

The entire fatigue life of a component can be roughly resumed by the CMB equation which models the crack initiation stage until a millimeter crack is formed followed by the propagation stage where the Paris equation defines the crack growth rate per cycle. Failure is often defined when reaching a critical toughness limit, K_{cr}. Figure 2.4 illustrates this sequence, as Chaboche [13] elegantly resumed. The various phases of the crack growth come from the 'total life concept' of Jeal [34].

Cracks originate in the atomic scale. Following the law of energy conservation,

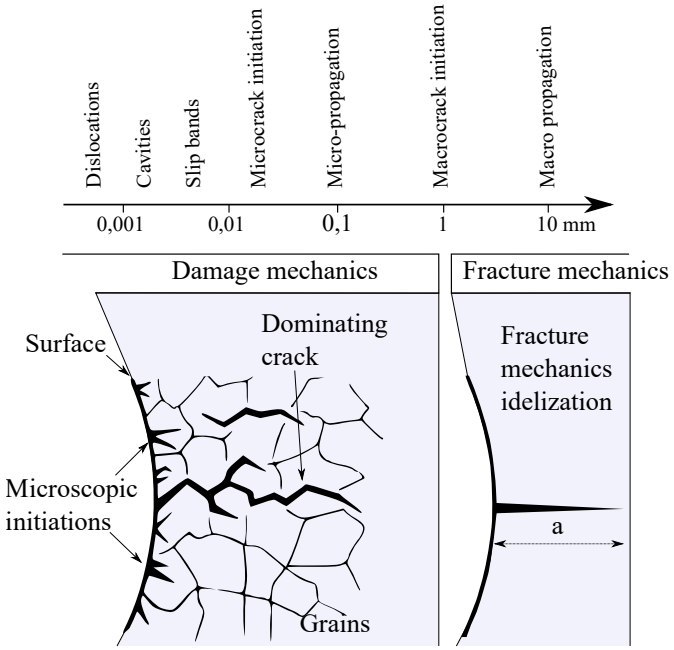

Figure 2.4.: Conceptual sketch of a macroscopic crack initiation, which is a multi-scale problem. Adapted from [13].

applying work on atoms such to bring the atomic bond out of equilibrium, causes fracture. After debonding, two new surfaces are created with a surface energy per unit area equaling the fracture energy that was needed to move the atoms away from each other. By a similar mechanism also the lattice structure of grains is plastically deformed. The cyclic deformations within slip bands lead to dislocation nucleation or piling up of dislocations to the surface and cause extrusions and intrusions. Microscopic fatigue cracks initiate at these intrusions. Several modeling approaches have been proposed by Gumbsch et at. [30], Bitzek and Gumbsch [12], Lin and Ito [44] Tryon and Cruse [95], Kadau et al. [37] and Polak et al. [65; 66], just to name a few; or good overviews have been written by Riemelmoser et al. [76] and Sangid [79]. Such approaches, however, are not practical for the larger scale. On the microscopic scale, the variation in grain structure and chemical composition, the presence of inclusions or other stress intensifiers, result in a significant statistical scatter between the highest and lowest amount of cycles to crack initiation between testing samples at macroscopic scale. It is not feasible to precisely predict how, where and when microcracks will initiate. Many researches that focus on the microscopic scale have increased the understanding of crack mechanisms in a qualitative manner, but struggle in giving quantitative solutions for practical engineering problems. For this reason the CMB

approach is so powerful, because it does not pretend to describe the micromechanical phenomenon in detail, it considers it as a kind of black box and effectively quantifies the life including the scatter. We could say that at macroscopic scale the scatter in life can be considered an aleatoric uncertainty, inherent to the random crack formation phenomenon.

Recognizing the size scale at which the crack growth is taking place is key to model it properly. Multi-scale approaches arose out of the need to model each stage of the crack growth with the correct mechanisms valid for that stage. Important factors are the length of the crack (if at all initiated), the grain size, the size of defects etc. The next section reviews crack growth techniques especially focused on crack nucleation from inclusions.

2.4. Nucleation from Inclusions

In this thesis we focus on fatigue crack initiation caused by the presence of forging defects. This section gives an overview of methods to evaluate crack nucleation from inclusions in general and then, given the specificity of the current project, we narrow the choice to one approach. I will not make an exhaustive narrative of all the research made on this subject, but only point out some interesting projects from where I picked ideas or which have similar approaches as the one proposed in this work. Recently, Zerbst et al. [106] wrote a good review of literature on fatigue failure from NMIs.

Just as for normal fatigue assessments, also when referring to the fatigue life of inclusions, this life is split into two or more stages, see Pineau and Antolovich [64]. One could conventionally divide the total fatigue life (N_F) into an initiation life (N_i) and a propagation life (N_p):

$$N_F = N_i + N_p \tag{2.5}$$

These stages can be further divided, see McDowell et al. [51]:

$$N_F = N_{inc} + N_{MSC} + N_{PSC} + N_{LC} \tag{2.6}$$

where the life is split into an amount of cycles of incubation (N_{inc}) followed by microstructurally small cracks (N_{MSC}), physically small cracks (N_{PSC}) and long cracks (N_{LC}). Probably also for the case of our studied forging flaws we could make this fine distinction where single particles incubate independently and through a process of successive particle encounters and intermittent percolation the entire flaw region coalesces into an entirely weakened area from where the long crack starts growing. The

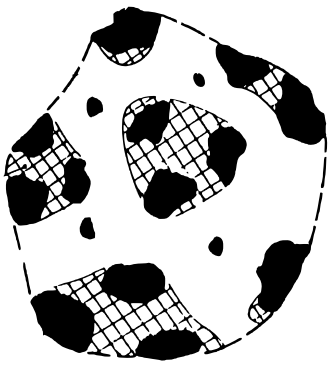

Figure 2.5.: Conceptual sketch of the nucleation process of forging flaws. The single particles coalesce together by fracturing the matrix material. Once this process is finished and the interstitial matrix is collapsed, the crack starts growing outside of the defect region. Adapted from [27].

idea of coalescing particles is sketched in Figure 2.5, from Foth and Oberparleiter [27]. For the purpose of modeling and especially for the limited experimental information, we need to combine the several stages and stick to a two-phase approach: a crack nucleation phase within the microcrack regime and a crack propagation phase in the sense of long initiated macrocracks which can be computed with fracture mechanics.

2.4.1. Other Approaches

Asquith [9] proposes to cover the entire life of a turbine disk probabilistically with a 3-parameter Weibull. The reasoning behind this approach is that crack propagation in the steady growth phase is captured pretty well and does not cause much scatter. The main source of scatter is what happens before, all the way back to the crack nucleation. Therefore it can be said that a component has a minimum life (especially dictated by the 'known' propagation rate) after which the probability of failure starts increasing following the Weibull curve. This is a particular approach which was proposed on the basis of experiments from component testing of small aero-engine rotor disks. The model can evidently not be applied to component design based on specimen experiments; but the idea of applying a minimum life to a component or a specimen or even to a single flaw, is a realistic one. After all, there are no components being produced that fail at the first load cycle. Despite this being true, it is also not easy to find physical or experimental evidence for fixing the threshold at a certain minimum life. As will be discussed later, not applying a threshold parameter to the Weibull approach has mathematical convenience.

Huron and Roth [33; 78] studied the influence of inclusions in nickel-base disks manufactured by powder metallurgy. For the strain controlled tests they artificially

seeded the material with ceramic inclusions. They observed that the fracture mechanic calculations underestimated the observed fatigue life of the seeded specimens significantly and attributed the difference to the incubation time. Even if they did not propose a specific method to quantify this nucleation time, they observed that it highly depended on the size of the flaw and its position (being it a surface or volume seed), the testing temperature and the stress range. The latter is interesting, since the fracture mechanics predictions were rather driven by maximum stresses for negative R-ratios. Similar findings are confirmed by Hu et al. [32].

Chapetti and Guerrero [14] proposed to model inclusions as simple notches. Fatigue strength is related to sharpness of notches — modeled as very blunt, blunt or sharp notches — and their length. The fatigue model is based on LEFM and has a size effect defined by a size dependent elastic stress concentration factor, k_t. Below a certain k_t value there is no propagation taking place, above the threshold value microcrack propagation occurs. The entire procedure is also put in dependence of the size of microstructural barriers (e.g. grain boundaries). In this thesis we will apply a similar approach. Instead of using a size dependent k_t, we will apply a local LCF approach accounting for the statistical scatter, which also captures the size effect.

Zhang et al. [15; 16; 36; 107; 108] performed experiments on a nickel-based superalloy sample with a NMI on a grinded and polished surface. Based on high (angular) resolution Electron Backscatter Diffraction (EBSD) images, the grain structure and the geometry of the NMI where faithfully modeled with a crystal plasticity Finite Element Method (FEM). These simulations were able to represent the process of interfacial decohesion at the matrix-inclusion boundaries as observed in the experiments and the subsequent development of cracks into the neighboring grains. Such methods require thorough knowledge of the particular metallographic situation around the flaw, which is normally not given for real life components. Besides, this approach has been applied to NMIs which are smaller than the average grain size, which is generally not the case for the rotor steels studied in this thesis.

A recent, similar study was done by Schäfer et al. [81] on NMIs in martensitic steels using crystal plasticity models with the non-local Fatemi-Socie parameter to quantify the nucleation potential. In a very ordered fashion they analyzed different types of inclusions by varying the defect properties: interface between NMI and surrounding matrix (perfectly bonded, detached, cracked defects and voids), defect size, shape and load level.

Also Murakami dedicated numerous publications to the effects of NMIs. His book on metal fatigue [56], focusing on small defects and NMIs, is a very good starting point for entering into the subject. In Section 6.2 he indicates that “once an inclusion is debonded at its interface, the interface can no longer sustain the applied stress, and

the inclusion becomes mechanically equivalent to a stress-free pore. This concept is extremely important in the solution of inclusion problems."

In this thesis we will apply this assumption, since any alternative of modeling an inclusion as a second phase particle, necessitates additional information on material hardness, bonding properties etc. of that particle, which are not available for the material at hand. Modeling it as a void is the next most feasible approach. The modeling approach presented in this thesis does not pretend to be a detailed description of all the stages in the nucleation process. It will rather be an effective approach suitable for direct application within engineering design tools. The concrete tool on which we build, *ProbFM*, is briefly described in the next section and the LCF-based method envisaged for quantifying the nucleation life is described thereafter.

2.5. Probabilistic Fracture Mechanics

The development of *ProbFM* arose from the need to probabilistically describe the failure mechanism originating from cyclically loaded forging flaws in large rotor disks for the energy sector. This approach is similar to DARWIN [18; 22–24] but with some important enhancements that are listed by Amann [4] in Chapter 1.

Recently also Romano et al. [77] developed a probabilistic post-processor based on the Kitagawa-diagram concept to assess component fatigue on Additive Manufacturing (AM) parts for the aerospace industry. This approach is very different from *ProbFM*, since it is not explicitly performing crack growth simulations using $\frac{da}{dN}$ with, e.g. the Paris law. It is rather assessing zone risks based on the probability of occurrence of large defects in the zone and coupling the zones based on the weakest link theory.

ProbFM is a high-performance computational framework able to execute billions of MC simulations of fatigue crack growth using LEFM methods. A forging flaw is modeled as a sharp crack with a size a, and a specific location within the disk. Siemens Energy is currently running more than 1000 gas turbines in its fleet. All the inspection data obtained during production of the rotor parts is stored in a proprietary database. From this database statistical information is retrieved about the amount of inspected disks with their sizes and volumes but especially the observed KSR sizes and their locations within the forgings. Together with the PoD for the used UT technique and the conversion factor, k, the TFS is found. Within a MC loop, flaw samples are drawn at random positions and of random sizes according to their real-life appearances. Also the variability in material properties (e.g. fracture toughness and crack growth rate) are stochastically sampled from measurements in material tests.

Based on transient FEM calculations of the components, the driving loading conditions at the sampled flaw location are derived. The LEFM calculations are performed using implementations of the standard design tools IWM Verb and NASGRO. To solve the stress intensity factors (SIF) one typically needs size parameters a and c and the distance to the surface d in order to distinguish between surface, near-surface and volume cracks. The stress intensity range, ΔK, is computed using the SIF solution, Y , together with the largest principal stress range and crack size a:

$$\Delta K = \Delta\sigma\sqrt{\pi a}Y \tag{2.7}$$

ΔK is fed into Eq. (2.4) where the crack growth rate is iteratively computed until failure. Failure is defined either by reaching the fracture toughness, K_{Ic} or using the Failure Assessment Diagram (FAD) (with the basic level assessment from SINTAP [90]). Also the Irwin plastic zone extension can be used to account for plasticity induced effects, either in the crack growth definition or as failure criteria.

For the considered type of components, flaw occurrence is so small that the probability of two flaws interacting with each other can be neglected:

$$\rho_{all} * V_{comp} \ll 1 \tag{2.8}$$

where ρ_{all} is the total volume occurrence flaw rate and V_{comp} is the volume of the component. Therefore, crack interaction is currently not accounted for in *ProbFM*. Interesting literature on crack formation from interacting flaws, though, has been written by Weichert [105].

The formulation of the crack growth model is resumed in high-performance numerical look-up tables, which are read by the brute-force MC in a very efficient way. The differential equation is discretized using the higher order Runge-Kutta integration scheme, which ensures overestimation of the crack growth [5], thus a conservative approach.

The results of *ProbFM* are fundamentally expressed in the two graphs of Figure 2.6. The left graph is a voxel-based risk map of the component, where the colors indicate how many simulated flaws led to failure in the specific voxel at a fixed amount of cycles. The right graph shows the Probability of Failure (PoF) vs. the amount of load cycles. As soon as the PoF exceeds a predefined safety criteria, the component is deemed unsafe and should be inspected/replaced. The example shows realistic results for a rotor component. The same results are the base-case for the case-study presented in Chapter 5.

One important conservatism in this approach is that is does not account for the crack nucleation phase: flaws are assumed to be sharp cracks from the beginning.

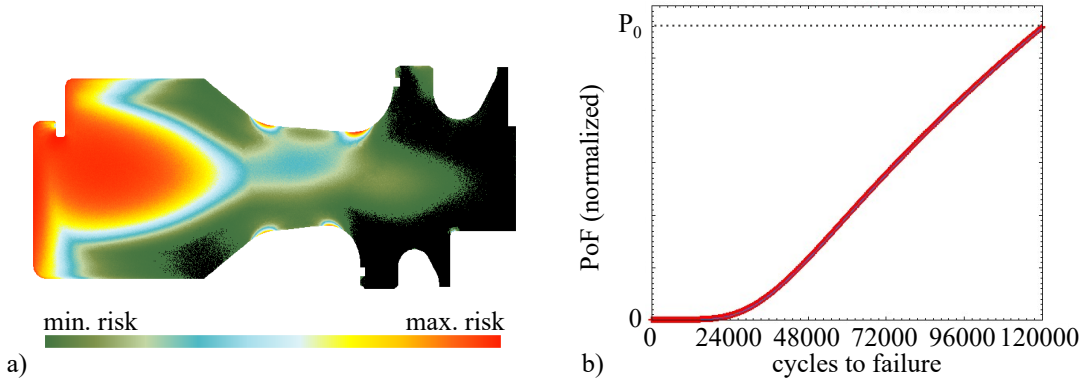

Figure 2.6.: Results from a *ProbFM* calculation on a gas turbine rotor disk. (a) Voxel-based risk contour plot shown on a linear scale. (b) Normalized PoF vs. load cycles.

This assumption led to very conservative results, which were a good basis to start from. In this thesis we propose the addition of the nucleation phase to this already existing probabilistic framework.

2.6. Local Probabilistic LCF

Based on experimental findings we know that the nucleation process is significantly influenced by the temperature, the local stress range, the flaw size and its vicinity to the surface. These properties also define the minimum requirements for the envisaged modeling approach for crack nucleation. Besides, it has to be a probabilistic method, in order to be fully integrated in the *ProbFM* framework. In the literature there are several probabilistic methods claiming to capture the statistical size effect, see e.g. Deyber et al. [19] or Zhu et al [3; 109; 110]. We decided to build upon the work presented by Schmitz et al. [45; 46; 82–85], which was developed to assess the fatigue crack initiation originally intended for the reliability assessment of nickel-based superalloy blades and vanes of gas turbines. It is a local probabilistic LCF method defining the probability of crack initiation on the surface of a component. The basic idea in this thesis is to transfer this methodology from the component size to the flaw size and apply the same concept on the small surface of a forging flaw. In this section we present the general methodology, following the description of Schmitz [82]. In Chapter 4 we present its application on forging flaws.

The process of crack initiation depicts the time for dislocations along slip bands to grow into larger intrusions and extrusions at the locations marked by intense loading. These are often locations near sharp geometrical notches with the most detrimental loading conditions in terms of temperature and stress intensity. This movement and

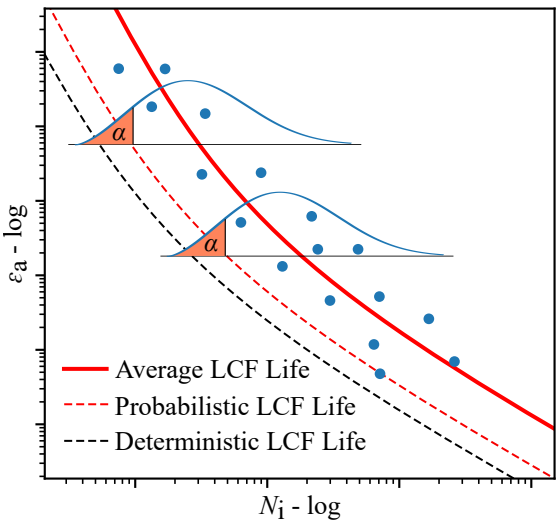

Figure 2.7.: The ε-N scatter is represented by a Weibull distribution. The red solid line represents the average LCF life. The red dashed line indicates the LCF initiation life for a certain probability α. The black dashed line represents a deterministic LCF life including safety factors with unknown failure probability. Adapted from [85].

accumulation of dislocations is statistical in nature. Due to this aleatory uncertainty the location of the first crack is not known *a priori*, nor is the exact amount of cycles. A common way to handle this uncertainty is by the so called safe-life approach. Rather than considering the statistical scatter as such, this approach defines a deterministic design curve for the lifetime of the material. This approach is made conservative, thus 'safe', by laying the curve at (typically) two standard deviations from the average measured lifetime of the specimens. This should implicitly account for the improbable events laying in the tail of a normal distribution. But, in reality the rare events are not explicitly accounted for and the risk is not quantified. This makes the deterministic approach effective, but not safe per se.

The LCF life is defined using the CMB formulation, Eq. (2.3). This equation is schematically plotted in Figure 2.7. The local approach assumes that the number of cycles to crack initiation N_i on each partition $\{A_j\}_{j=1...k}$ of boundary surface $\partial\Omega$ are independent from each other. This, because the initiated microscopic cracks only cover few grains. Given this independence, the PoF for the entire boundary surface of a component can be treated as the PoF of the weakest link. Schmitz' approach uses the so-called hazard rate h:

$$h(n) = \lim_{\Delta n \to 0} \frac{P(n < N_i < n + \Delta n | N_i > n)}{\Delta n} = \frac{f_{N_i}(n)}{1 - F_{N_i}(n)} \tag{2.9}$$

where $F_{N_i}(n)$ and $f_{N_i}(n)$ are the cumulative distribution function and the probability density functions of the random variable N_i. In other words, the hazard rate is the probability of crack initiation within the next cycle. It is assumed that the cycles to crack initiation N_i are Weibull distributed

$$F_N(n) = 1 - \exp\left[-\left(\frac{n}{\eta}\right)^m\right] \tag{2.10}$$

with Weibull shape and scale parameters m and η. The sum of the hazard rates for each surface partition A_j gives the hazard rate for the entire boundary surface $\partial\Omega$. Since the crack initiation is a local functional of the strain and temperature field, we introduce the local hazard density $\rho(n; \varepsilon_a(\mathbf{x}), T(\mathbf{x}))$ — $\mathbf{x}$ indicates that the variable is local and varies in space — and reformulate the hazard rate by integration over the component's surface

$$h(n) = \int_{\partial\Omega} \rho(n; \varepsilon_a(\mathbf{x}), T(\mathbf{x}))dA. \tag{2.11}$$

With its cumulative function

$$H(n) = \int_0^n h(t)dt \tag{2.12}$$

which, combined with Eqs. (2.9) and (2.10) gives

$$F_N(n) = 1 - \exp(-H(n)) \tag{2.13}$$

If we chose the following hazard density function

$$\rho(n; \varepsilon_a(\mathbf{x}), T(\mathbf{x})) = \frac{m}{N_{i_{det}}(\varepsilon_a(\mathbf{x}), T(\mathbf{x}))}\left(\frac{n}{N_{i_{det}}(\varepsilon_a(\mathbf{x}), T(\mathbf{x}))}\right)^{m-1}, \tag{2.14}$$

then Eq. (2.10) can be solved with

$$\eta = \left(\int_{\partial\Omega} \frac{1}{N_{i_{det}}(\varepsilon_a(\mathbf{x}), T(\mathbf{x}))^m} dA\right)^{-\frac{1}{m}} \tag{2.15}$$

$N_{i_{det}}$ is the deterministic number of cycles to crack initiation valid for strain amplitude ε_a and temperature T. It is obtained by calibrating the CMB equation (2.2) with test results using a Weibull distribution with shape parameter m. Scale parameter $N_{i_{det}}$ is defined for a unit surface area. This is done by considering the gauge areas of the specimens used for LCF testing. Since the temperature and the stresses at the gauge area are usually uniformly distributed, the same probability of crack initiation applies to the entire gauge area. In principle, the larger this area, the higher

the total probability of crack initiation. Dividing the hazard rate by the gauge area, results in a hazard density per unit area. This characteristic makes this approach so powerful: applying $\rho(n)$ to larger components with uniform stress and temperature fields results in higher probabilities of crack initiation. This is how the size-effect is accounted for. But it also allows to apply $\rho(n)$ to a non-uniformly distributed stress- (or temperature-) field. Lower density areas will still contribute to the cumulative risk of failure, as long as their areas are large enough. The other way around, high density spots, if very tiny in surface, may contribute less. These considerations open a world of opportunities for design optimization, and holistic risk assessments of engineering components. With deterministic calculations one would normally only consider the maximum density spots, without correcting for the area they act on. Often this results in overly conservative designs.

The size-effect is very much influenced by shape parameter $m \in (0, \infty)$. It is a material parameter characterizing the scatter in LCF life. A small m indicates a large scatter in fatigue life; for $m \to \infty$ the scatter reduces and falls back into the deterministic case where the size-effect does not play any role.

This entire approach is integrated in a post-processing tool based on Finite Element Analysis (FEA) results. Since locations with high stress concentration result in high gradients of hazard densities, we need to consider higher non-linearities in the integrand of Eq. (2.11). This is achieved by using higher order quadrature formulae with sufficiently many integration points, as described by Schmitz et al. [83] in Section 2.2. Figure 2.8 illustrates the application of the approach on a vane component of a gas turbine, as presented by Mäde et al. [45]. Figures a and b are respectively the input stress- and temperature fields of the component. Figure c is the resulting hazard density field, highlighting the most sensitive parts of the component. Based on the results, a component design may be adjusted or optimized. In the present study we consider the inner-surfaces of forging flaws as surface of interest. These relatively small areas — compared to the component- or specimen sizes — result in relatively small PoF due to the size effect. But if we consider the notch effect of such forging flaws, we expect significant local stress enhancements. Despite the very small areas, the local hazard may not be neglected.

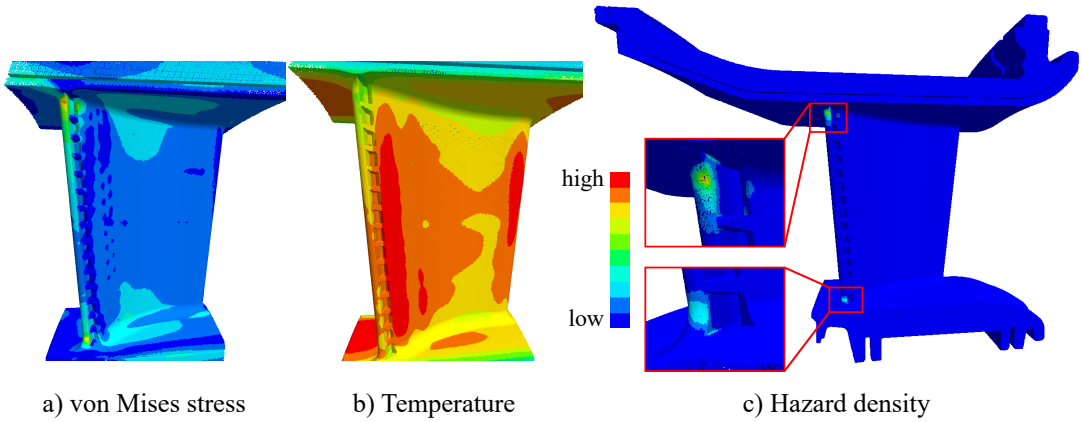

Figure 2.8.: Example of the use of the local probabilistic LCF approach on a real-life vane component. FEA results for the (a) von Mises stresses and (b) temperatures. (c) The hazard density with hot-spot regions resulting from post-processing. Integration of the hazard densities results in a Weibull distribution for the overall probability of crack initiation on the component. From [45].

3. Experiments

3.1. Introduction

One of the main challenges in developing a nucleation model for forging flaws is the lack of experimental data. Obtaining specimens including flaws is not trivial. In general, rejected forgings that did not pass quality control are remelted and used again as raw material in order to reduce costs. Technical, strategic and cost aspects play an important role in finding suited testing material. Another aspect is the testing procedure itself. The purpose is to capture the nucleation phase and separate it from the crack propagation phase. Once the specimen is loaded, the fracture surface reveals the relevant results for the nucleation time assessment, which serve as input for calibrating the nucleation model. All the aspects of the experiments, the uncertainties in the various steps, the assumptions and the difficulties are presented and discussed in this chapter.

3.2. Previous Testing Campaigns

In the '80s and early '90s there have been two major European testing campaigns (FVV-project and COST-project) where specimens were machined from rejected large steel forgings for the energy sector, see [10; 11; 35; 48–50; 80]. A total of 22 forgings, featuring individual as well as resolvable and non-resolvable group indications from UT were used for cyclic testing. Main target was to investigate the fracture mechanics behavior of the flaws. Based on the size of the flaws, LEFM was successfully applied to predict the crack propagation. A fatigue crack growth curve was measured with compact tension (CT) specimens without defects. Especially Scarlin et al. [80] reported that from the comparison between the actual number of loading cycles N_{test} and calculated amount useing Paris-law N_{calc} one can postulate that an incubation time is required to justify the longer observed lifetime N_{test} of some specimens.

Despite the fact that this discrepancy between N_{test} and N_{calc} is known, it is common practice to model the crack propagation of a flaw by LEFM, assuming that the development from a flaw into a sharp crack is instantaneous or, in other words, that the flaw is a sharp crack from the beginning. The first attempt to quantify the nucleation time of a forging flaw was reported in 2013 in an internal report of

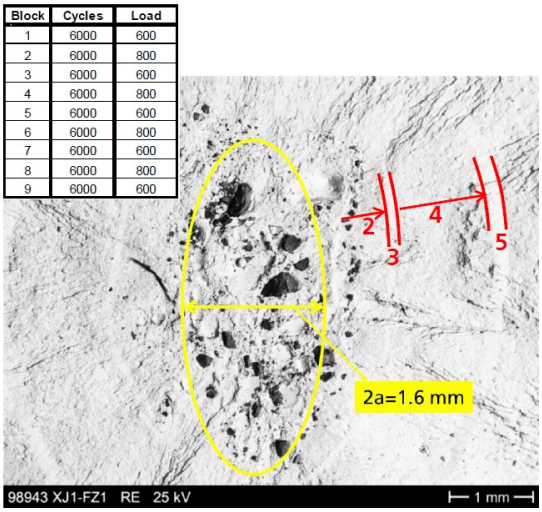

Figure 3.1.: SEM image of NMI field on the fracture surface with visible beach marks around the defects. The beach marks are used to back-trace the nucleation time of the flaw and the crack propagation rate per loading block. From [89]

Fraunhofer-Institut für Werkstoffmechanik (IWM) in Freiburg, Germany [89]. In a project partnered by Siemens Energy, three test specimens were taken from a large rotor forging with defects. The defects were clusters of NMI which were previously detected by UT. Subjecting the specimens to load blocks of alternating amplitudes produced beach marks on the fracture surfaces. Figure 3.1, taken from the internal report, illustrates how the beach marks were used to back-trace the load history of the specimen and therewith deduce the nucleation time of the flaw in which the crack front did not yet exist or propagate. One important result from these experiments, also reported by Varfolomeev et al. [99], is that they suggest a considerable amount of load cycles to be consumed in the nucleation process.

These findings motivated to further look into this phenomenon and start a thorougher testing campaign on forged rotor materials with manufacturing defects involving two different specimen geometries, three testing temperatures and various specimen batches from different forgings. The experimental setup and the results are discussed in the next sections.

3.3. Ultrasonic Inspection

Since it is both expensive and difficult to find appropriate testing material for specimens with inclusions, for the sake of this study, disks were selected that failed quality control for having too many UT indications. Three of such scrap disks provided the

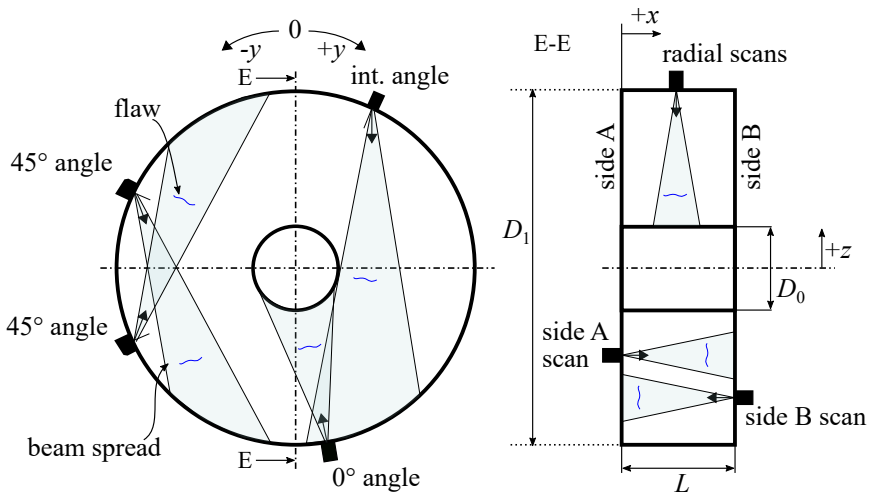

Figure 3.2.: Axial and radial UT scanning directions on a rotor disk. The marked areas are the focus areas of each scan. The sketched flaws show the ideal flaw orientation captured by each scanning direction.

opportunity to obtain many specimens which include manufacturing related forging flaws. All three were produced with the same high strength nickel-chrome steel alloy ($26NiCrMoV14-5$, see Table 3.1) and forged at Saarschmiede GmbH in Völklingen, Germany.

Element	Fe	Ni	Cr	Mo	V	Mn	C	Si
Weight [%]	min. 93.5	3.7	1.5	0.35	0.1	0.28	0.27	0.05

Table 3.1.: Chemical composition of $26NiCrMoV14-5$.

The locations of the indications could be determined by combining the c-scan images of inspections from different directions. Figure 3.2 shows how different scanning directions are typically applied on rotor disks. Depending on the orientation of the flaws, one direction may capture more reflected waves than other. The KSR sizes of the different scans for the same flaw coordinates are compared. It is assumed that the largest size comes from the scan oriented orthogonal to the main flaw orientation. This should be the weakest direction of the flaw when loaded. The specimen preparation aims at orienting the specimen in this same direction in order to hit the flaw from its most vulnerable flank and preserving conservatism in the later modeling approach.

Beside the classical UT methodology, on one disk also 3D SAFT was applied. With this technique the defect localization is improved but also the signal-to-noise reduction allows for better separation of group indications. These qualities were very useful for a

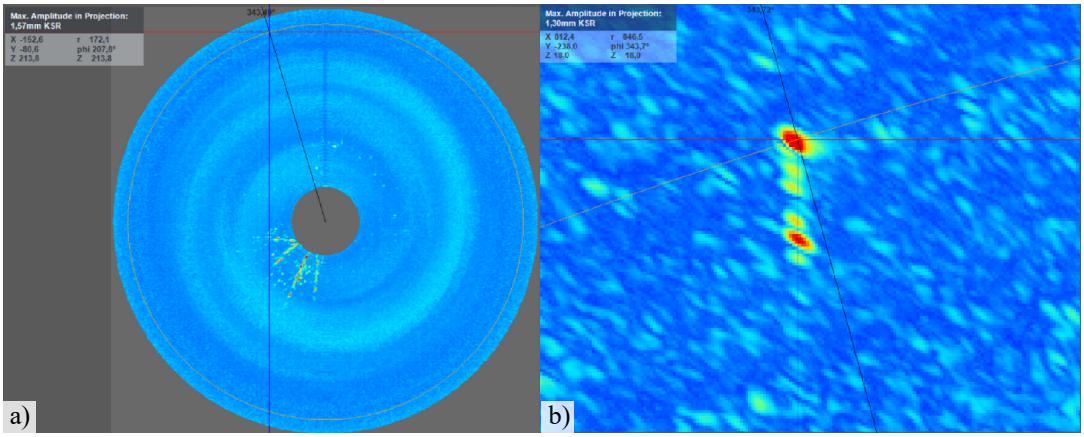

Figure 3.3.: Example of a 3D SAFT scan on a rejected disk with many UT indications. (a) Entire disk with axial projection view. (b) Detail of a group indication where different indications could be distinguished. The resolution and localization of the flaws are improved w.r.t. classic UT.

more precise specimen preparation. Figure 3.3 illustrates the outcome of a 3D SAFT scan, where the single inclusions can be better distinguished and the resolution is higher w.r.t. classical UT.

3.4. Specimen Preparation and Loading

The UT indications help to distinguish clean material areas and areas with defects. From the clean regions, specimens for the base material characterization are taken. These test results are then compared with the Siemens Energy internal database for this specific material and the proprietary material design models. From the areas with defects, specimens appositely designed for this campaign were extracted.

3.4.1. Base Material Characterization

Over 100 specimens of clean material were tested to obtain information on the following aspects.

Orientation

The influence of the orientation within the forged component — being it radial, tangential or longitudinal, see Figure 3.4 — has been examined with both static tension tests and cyclic LCF tests. Since the orientation seems to have little influence on the σ-ε curves, it can be concluded that the mechanical behavior of this material is isotropic.

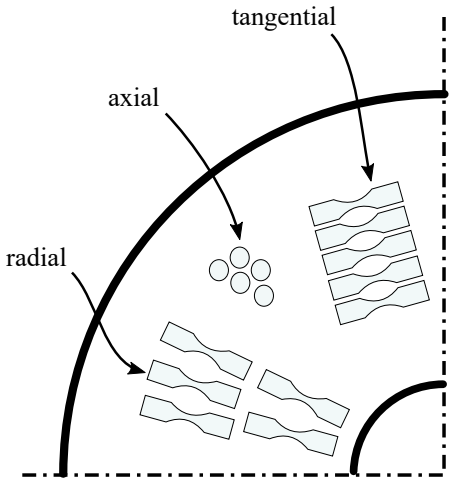

Figure 3.4.: Orientation of the specimen within the rotor disk.

Temperature

The testing temperature was varied from room temperature ($T_{RT} \approx 25\,^{\circ}\mathrm{C}$) up to ca. 500 °C, in two steps. These temperatures are selected based on the minimum and maximum operating conditions of this material within the gas turbine. Without giving away proprietary information, we call them T_{RT}, T_1 and T_2.

The temperature seems to have little influence on the fatigue life. This is in line with the thorougher Siemens Energy proprietary material database; the material shows a small temperature influence, even though not negligible. Figure 3.5a shows the results of the LCF tests at different temperatures. The lines are obtained from a Weibull fit of the CMB curve (see Eq. (2.2)) using a MLE approach. In this probabilistic approach we included the temperature correlation in the $\sigma - \varepsilon$ curves described by the Ramberg-Osgood formulation:

$$\varepsilon = \frac{\sigma}{E} + K \left(\frac{\sigma}{E} \right)^{1/n} \tag{3.1}$$

with $\frac{\sigma}{E}$ being the elastic part of the strain defined by the Young's modulus and $K \left(\frac{\sigma}{E}\right)^{1/n}$ the plastic part with K and n describing the hardening behavior at each temperature. The fitted parameters for the three temperatures are resumed in Table 3.2.

We assume that the scatter in the life — captured in the shape parameter of the Weibull distribution — is the same for all strain amplitudes and all temperatures. This leads to a constellation of Weibull distributions where the shape is identical and

Temperature	Ramberg-Osgood			Coffin-Manson-Basquin			
	E [MPa]	K [-]	n [-]	σ'_f [MPa]	b [-]	ε'_f [m/m]	c [-]
RT	2.000e5	1168	0.0757	2040	-0.104	0.8315	-0.795
T_1	1.690e5	929.7	0.0602	1351	-0.0808	0.8936	-0.770
T_2	1.526e5	730.8	0.0540	774.6	-0.0717	1.157	-0.760

Table 3.2.: Fitted material model parameters from Ecoflex base material characterization. Temperature dependent E, K and n for the Ramberg-Osgood equation and σ'_f,b, ε'_f and c for the Coffin-Manson-Basquin equation.

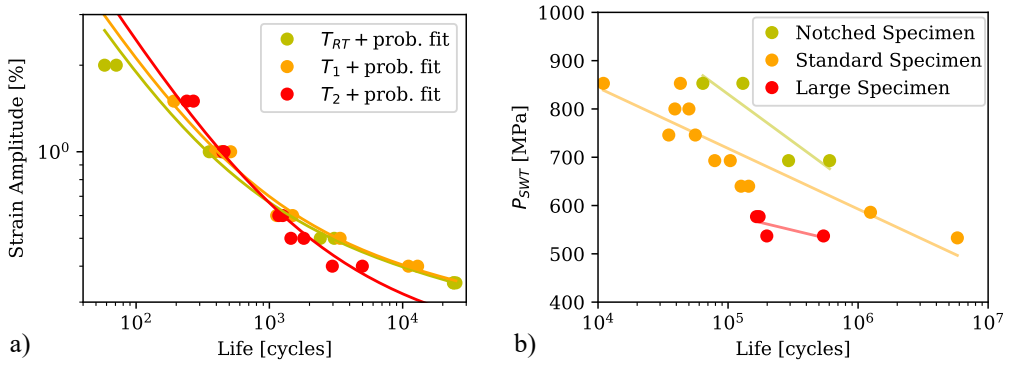

Figure 3.5.: (a) The influence of the temperature on the LCF life is plotted. (b) The influence of the specimen's size on the LCF life is plotted.

the scale is strain and temperature dependent, see Figure 2.7 for reference. This is an assumption that is often made in literature [46] but could definitely be improved; especially when more test points are available for defining particular scatter at varying strain and temperature and eventually even adding a minimum threshold value with the location parameter of the Weibull distribution.

Within this thesis we applied the 2-parameter Weibull distribution fitted to the above mentioned data points and obtained a shape parameter $m \approx 7$. For most steels this value lies between 2 and 10. A value of 7 can be considered at the high end. This might be due to the fact that the curves are based only on specimens from one forging; there is no batch effect influencing the scatter. The fitted parameters obtained from these test results are later used as material model at the basis of the nucleation model described in Chapter 4.

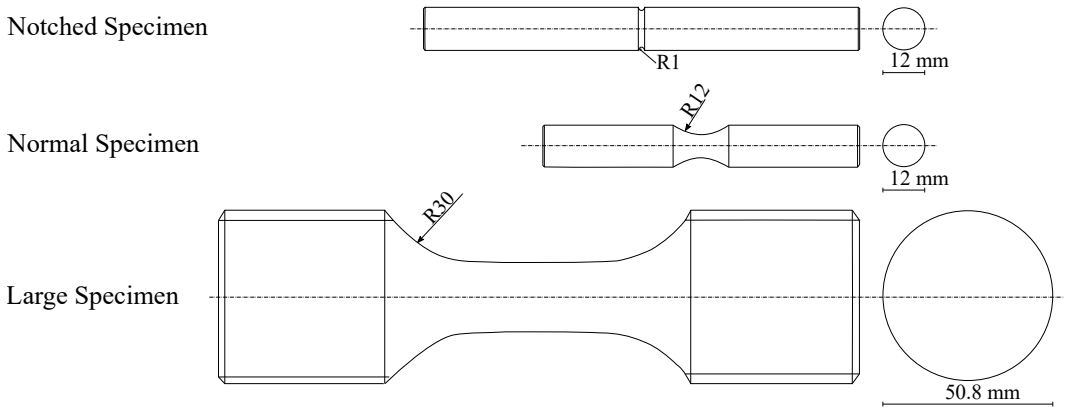

Figure 3.6.: The size-effect is tested with specimens of different sizes and stress concentrations.

Size

The statistical size-effect has been evaluated by performing stress-controlled LCF tests on large, normal and notched specimens. Figure 3.6 shows the specimen sizes for the three geometries used. The 'notched' and the 'normal' specimens are tested with a load ratio $R = -1$ ($R = \sigma_{min}/\sigma_{max}$). This means that no mean stress correction is needed. The 'large' specimens are tested at $R = 0.1$ and need a mean stress correction in order to be compared to the other results. This was done by applying the Smith, Watson and Topper equation [91] as recommended by the FKM guidelines [26] for linear-elastic stresses:

$$P_{SWT} = \sqrt{(\sigma_a + \sigma_m) \cdot \varepsilon_a \cdot E} \tag{3.2}$$

with σ_a being the stress amplitude.

The results are plotted in Figure 3.5b, where larger specimens result in a shorter LCF life. At low stress levels the curves seem to converge. This plot reflects well the weakest-link theory described with the probabilistic, local LCF approach from Section 2.6.

Load ratio R

The hysteresis loops have been examined with strain-controlled cyclic tests at different load ratios. Also these results were used to feed the material characterization curves.

3.4.2. Specimens with UT Indications

The actual goal of the testing campaign is to obtain data regarding the nucleation time of forging flaws. In order to do so, it is key to obtain specimens where the flaws

are located at the desired, central position of the sample. It is not trivial to obtain specimens by correctly cutting the large forged component at millimeter precision based on the UT indications only. For this reason some measures are taken to increase the accuracy of the cuts:

- providing the component of radial engravings every 5 degrees,
- performing a rough cut before inspecting again with UT and subsequently do the fine machining to obtain the final specimen geometry,
- where near-surface flaws were desired, applying Magnetic Particle Inspection (MPI) on the roughly cut specimens helped localizing the flaws.

Despite these measures, it was still difficult to locate the flaws exactly at the center of cylindrical tension tests or central, near the surface of 4-point bending tests. The actual position of the flaw within the specimen is only revealed by examining the fracture surface after testing. Another difficulty in obtaining appropriate specimens was the presence of secondary flaws within the specimen. Since these are normally at a distance from and always smaller than the principal ones, they should not interfere with them: the specimen should still break at the location of the principal flaws, since these weaken the material the most. Unfortunately, it was often not possible to impede to cut through these secondary flaws when machining the specimens out of the forging. This led to having small surface flaws in the specimen that often became significant to the failure mechanism of the specimen, as we will analyze further on.

The specimens are cut in two different geometries, depending on the location of the flaw: cylindrical tension tests and 4-point bending tests.

Cylindrical Tension Tests

This specimen typology has been applied to different testing temperatures. At higher temperatures, the specimen geometry must be longer in order to grant a homogeneous temperature field at the gauge area and for cooling down rapidly at the screw region (such that the machine is not over-heated), see Figure 3.7. The temperature is kept constant and homogeneous in the gauge area through a heating coil around it. This procedure has first been tested and verified on dummy specimens without UT-indications.

By cyclically loading the specimens in axial direction they exhibit a uni-axial, uniform stress distribution in the gauge-section (neck-region), where the flaw is located (approximately in the middle). The flaw is, where possible, oriented orthogonal to the loading direction. This way, the most disadvantageous condition is represented.

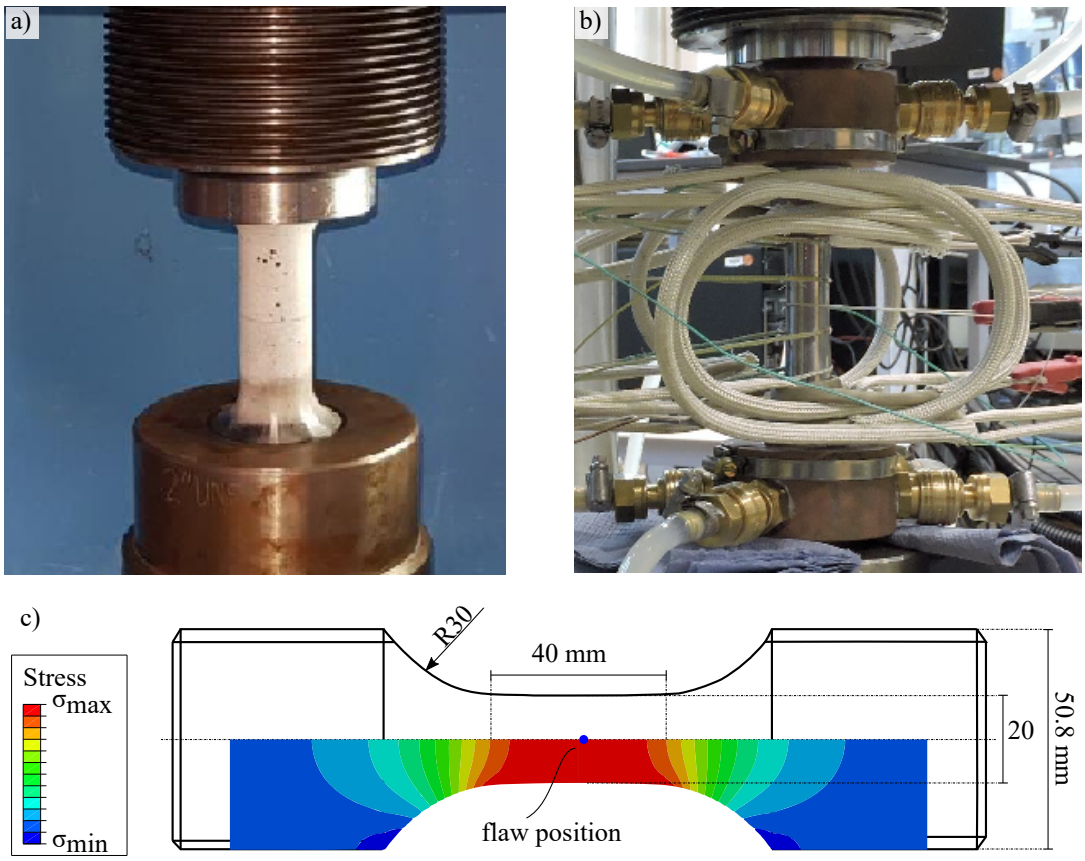

Figure 3.7.: Cylindrical tension test specimen in testing configuration (a) at T_{RT} and (b) at high temperatures T_1 and T_2. (c) Size of the principal features and stress field relative to the applied load obtained with Abaqus.

Unfortunately, it was not always possible to extract the specimens in this orientation due to the geometrical boundaries of the forging. When this was the case, the results should be critically analyzed and separated from the other.

As already mentioned above, one problem that appeared especially with this specimen type was the presence of secondary flaws at the borders. It has been tried to prevent those flaws from becoming the principal cause for crack formation by shot peening the specimen's surface. This cold working process introduces compressive residual stresses near the surface. By doing so the local tension load should relax and the flaws at (and near) the surface become insignificant to the crack formation. Despite successful application in other projects (e.g. [33; 64]) shot peening did not prove to be as effective in this testing campaign, where it was applied to 3 specimens: cracks were still initiated from small surface defects. Besides, shot peening introduces

additional complexity to the loading condition of the flaw which in turn becomes more difficult to be modeled faithfully. For this reason it has been decided not to apply the shot peening to the surfaces any further.

Another way to minimize the influence of the surface flaws is to try to prevent them in the first place. By applying SAFT inspection to the disks, there is a better chance to detect and localize the secondary flaws. This enables to better prepare the specimens by moving them some millimeter in one or the other direction in order to avoid cutting through small flaws. This method has been successfully applied to one of the three tested rotor disks, and produced a number of specimens that had less disturbing surface flaws.

4-Point Bending Tests

Alternative to the cylindrical tension tests there are the rectangular 4-point bending tests, see Figure 3.8. The reason for applying 4-point bending tests is a pragmatical one. Some of the flaws were found near the surface of the 'pancake' disk. Cylindrical specimens require the flaws to be at some distance from the border in order to locate them central w.r.t. the cylinder. 4-point bending tests offer a good alternative, because the desired location of the flaws in exactly near the surface. The 4-point bending setup was only possible at room temperature due to difficulties in setting up a heating device around the more complex geometry. There were also no furnaces available big enough for this setup.

The flaws are positioned central in longitudinal direction but near the surface w.r.t. the long side, as depicted in Figure 3.8b. That is the position where the local tension caused by bending is maximum. The figure shows a significant stress gradient in the gauge-section which makes the knowledge of the exact location of the flaw crucial. The stresses are uni-axial though. These particularities must be taken into account when modeling the samples.

Figure 3.9 illustrates how the specimens configuration within a disk segment is prepared based on c-scans of UT indications.

Beach Marks

Independent of the specimen typology, the experiments are run in alternating load blocks and beach mark blocks. Figure 3.10a illustrates how high load amplitude cycles with $\sigma_{max} = 800\,\mathrm{MPa}$ and stress ratio $R = 0.1$ are run in alternation with low amplitude cycles with same σ_{max} but $R = 0.6$. The low amplitude load cycles barely contribute to crack propagation and only leave a visible beach mark on the fracture surface when fatigue crack propagation takes place, Figure 3.10b.

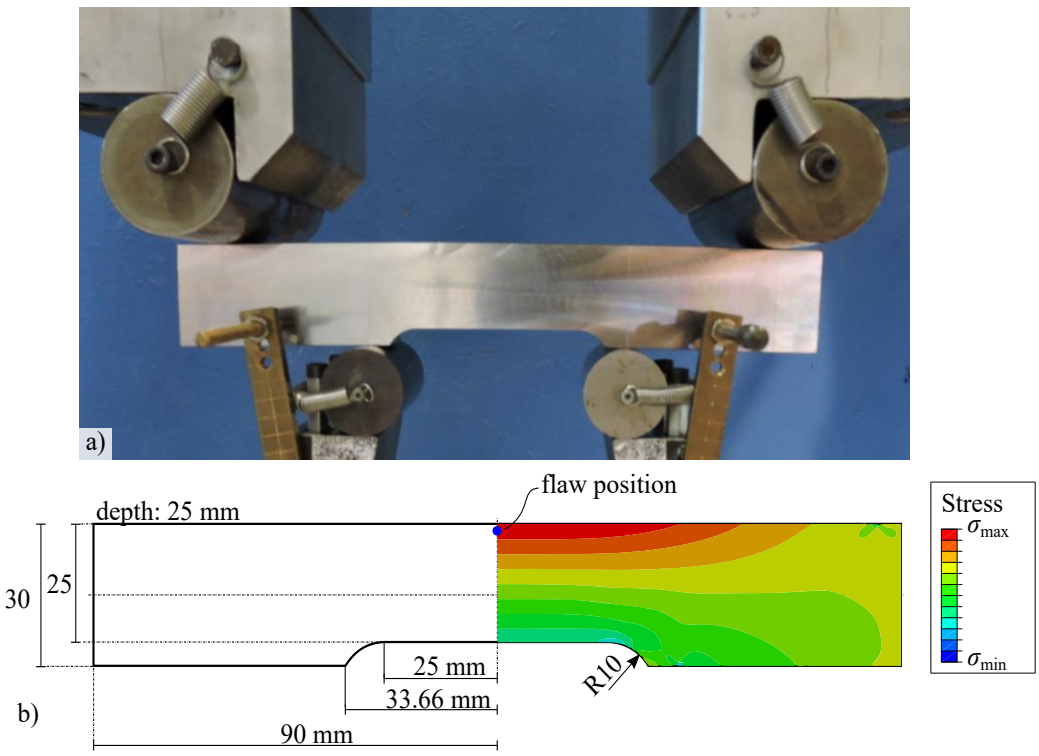

Figure 3.8.: (a) 4-point bending test in testing setup at T_{RT}. (b) Geometrical features with stress field relative to the applied load obtained with Abaqus.

Once the specimen breaks, the total amount of low amplitude load blocks are compared to the total amount of beach marks on the fracture surface. The low amplitude blocks that did not leave a beach mark are those occurring during crack nucleation — when the crack front was not yet propagating. They can be quantified by tracing back from the last load cycles in the sequence, as the figure suggests. Hence, the total amount of high amplitude load cycles consumed for the nucleation process can be counted. In the example of Figure 3.10 there are 18 low amplitude load blocks consumed before the first beach mark. As each load block contains 2000 load cycles, the nucleation process took 36000–38000 cycles. The beach marks are identified by direct visual inspection first, but also stereo microscopy and SEM are needed for the smaller marks. In some situations also the light angle and surface humidity had to be adjusted in order to make the beach marks clearly visible. When the test was performed at high temperature and the crack initiates near the surface, the color of the beach marks shows even better how the load blocks can be traced back. See Figure 3.11 for light camera images of high temperature specimens and Figure 3.12 for SEM images of the same inclusions.

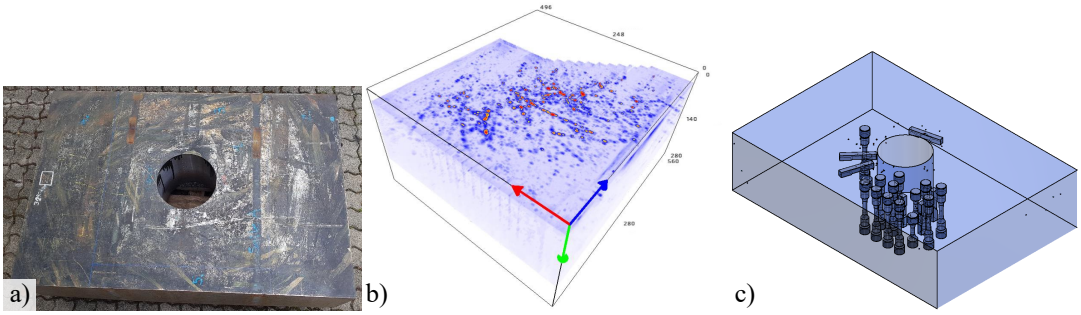

Figure 3.9.: (a) Segment of the rotor disk before specimen preparation. (b) Isometric view of the UT scan results on a disk segment. The red dots are indications of forging flaws. This scan is used to plan the specimens. (c) Specimen cutting plan in a 3D view of the segment indicating two different types of specimens (squared 4-point bending specimens and cylindrical tensile specimens) and different orientations within the forging. The small dots mark UT indications of defects.

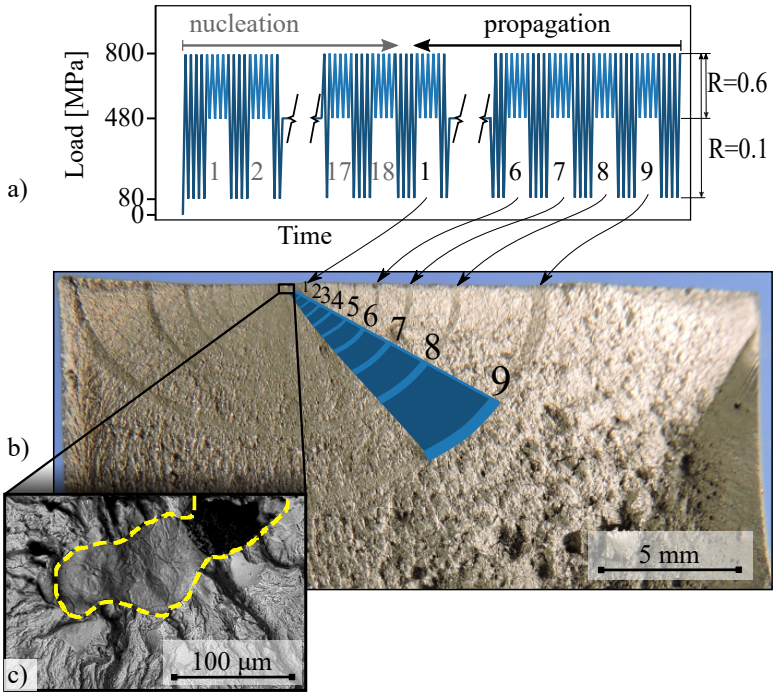

Figure 3.10.: (a) Schematic view illustrating the loading sequence of the experiments and its correlation to the visible beach marks. The last 9 low-amplitude load blocks caused the 9 beach marks of figure (b). In this example the nucleation occurred during the first 18 load blocks. (b) Image taken with a light camera showing the fracture surface of a 4-point bending specimen with a flaw near the upper surface and the corresponding fatigue crack growth in semi-elliptical shape. (c) SEM image of the flaw area. The yellow line marks the flaw.

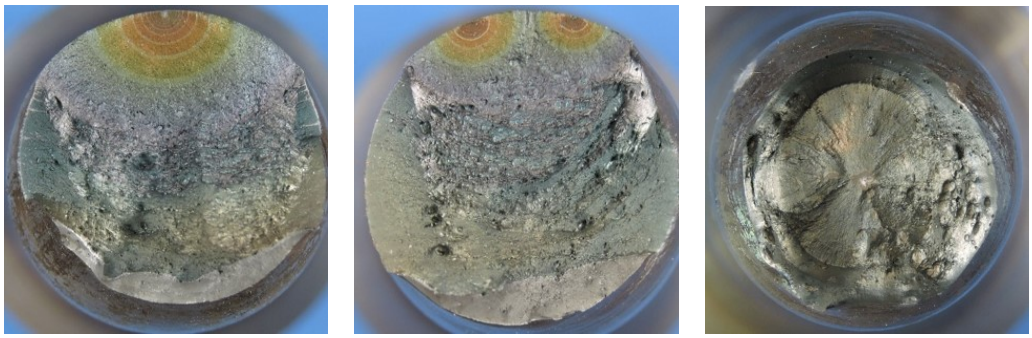

(a) Single surface flaw **(b)** Two surface flaws **(c)** Single volume flaw

Figure 3.11.: Light camera images of fracture surfaces of high temperature cylindrical tension tests. The beach marks from surface flaws (a)(b) are better visible than the ones from embedded flaws (c).

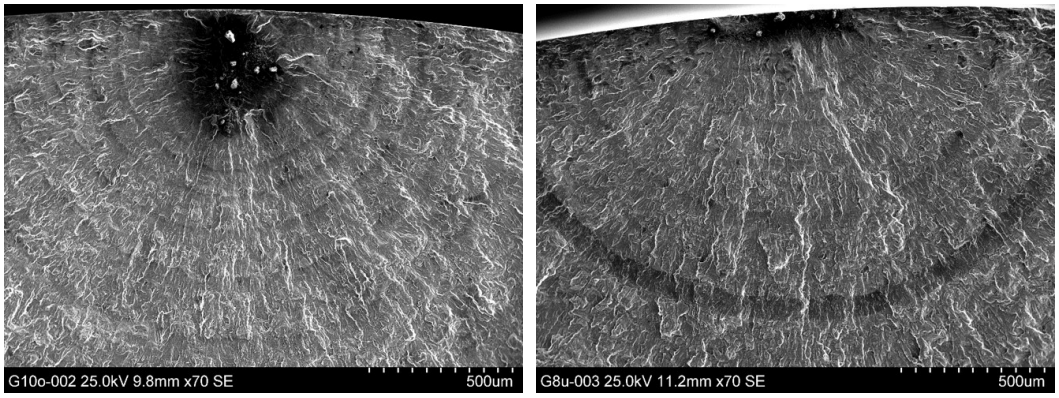

(a) SEM detail of Figure 3.11a. **(b)** SEM detail of Figure 3.11b.

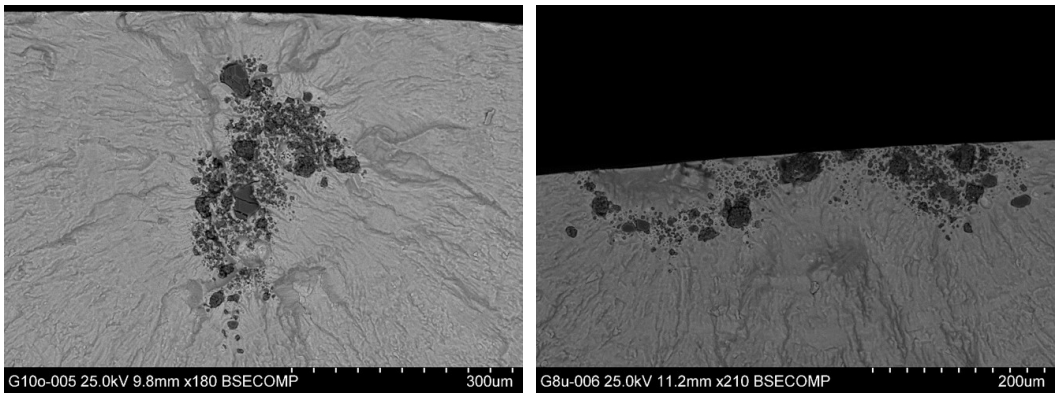

(c) Near-surface inclusions from (a) **(d)** Surface inclusions from (b)

Figure 3.12.: SEM images of fracture surfaces with visible beach marks and inclusions.

3.5. Results

3.5.1. Fracture Surface

The concentric beach marks of Figure 3.12 reveal the presence of a forging flaw, a weak-spot near their center-point. Resulting from the complex forging process, several different types and shapes of flaws can be observed. The SEM images in Figure 3.13 show the different types of forging flaws that have been observed in this study.

Separations

Figures 3.13a and 3.13d show a separation of the matrix structure. This type of flaw is sometimes better visible on images of secondary electrons (SE) (3.13d) than backscattered electrons (BSE) (3.13a). SE are very beneficial for the inspection of the topography of the sample's surface. The surface of separations is smooth. The matrix material is discontinuous. This may be caused by mechanical shear stresses during the manufacturing process (hammering of the ingot, high forging stresses in already cooled down areas of the forging etc.) and subsequent lack of fusion of the separation. This type of flaws is rather sharp and is likely to nucleate rapidly into a crack. They have only been encountered in one of the three tested disks and only near the outer surface of the pancake shaped forging. This makes them non-critical and irrelevant from a design standpoint, since the 'pancake' forging is machined into the final shape of the rotor disk and gets rid of the original surface material.

Inclusions

The majority of the observed flaws where inclusions. The number and sizes of the individual particles comprised in one flaw can vary, e.g. Figure 3.13e shows only one, relatively large, inclusion and suggesting few other large inclusions potentially being lost during the final fracture process. After a closer look at this single large inclusion, it seems to be a sinter material rather than a solid crystal. This sinter material may be the original shape of inclusions before they are further fragmented and diluted into the matrix in a large number of individual inclusions as shown in Figure 3.13c.

Both figures show mixed-oxide inclusions (potentially CaO, MgO, Al_2O_3 particles) trapped within the metal matrix. The cluster of densely packed particles of Figure 3.13c was crushed into its present form from a larger inclusion during the forging process. Figure 3.14a is a magnification of the mixed-oxide particles illustrating the crystalline structure. The observed size of the single particles in those clusters varies from a few micrometers up to ca. 50 micrometers. From the energy dispersive X-ray spectroscopy (EDX) of Figure 3.14b, mass and volume fractions of the elements can

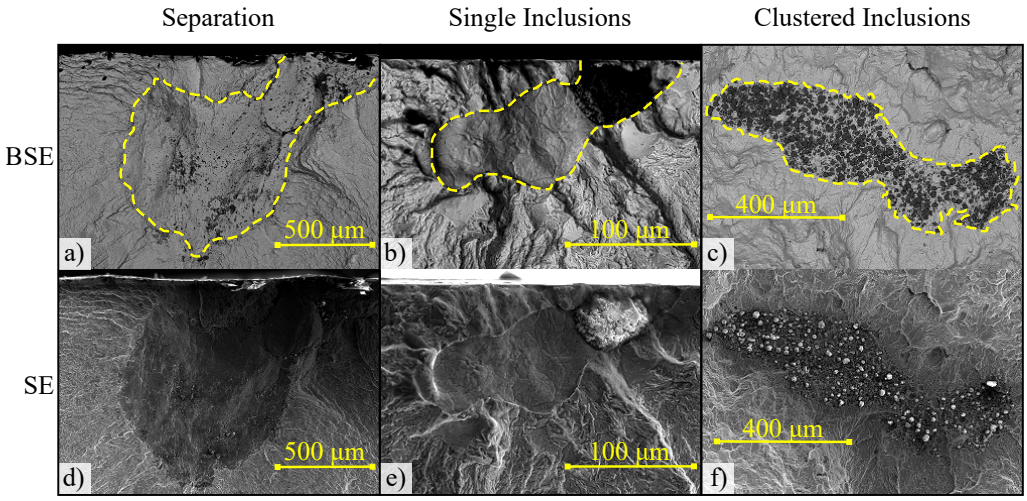

Figure 3.13.: SEM images of forging flaws illustrating the difference between separations, single sinter inclusions and clusters of inclusions. (a)(b)(c) BSE images of the same locations shown in (d)(e)(f) with SE images. Separations are recognized by the smooth surface (contrasting the rough cracked surface) and the absence of inclusions, which are normally clearly visible, see (c)(e)(f).

be approximately obtained. This type of flaws tend to be found near the center of the forging. They can have very compact shapes, as well as disperse; very elongated or only local spots. Figure 3.15 gives an idea of the variety of the densely packed inclusions.

The images of the densely packed inclusions have been further analyzed using image segmentation. The shape and size of the single particles could be approximated. Figure 3.16 illustrates how the area of interest of the SEM image is separated and binarized using adaptive threshold values of the grey-scale. Subsequently watershedding divides clusters into separate particles. The watershedding algorithm is discussed by Soille [93]. The areas of the single particles are measured and size distributions are obtained for each flaw. Figure 3.17 shows the results for three exemplar flaws. The area size distributions for all considered flaws can be described by power laws with exponents between -1.8 and -0.8. Work on the universality of fragmentation processes over a large range of scales and processes show power law fragment size distributions, see e.g. Kun and Herrmann [43] or Domokos et al. [20]. For a three dimensional system an exponent of -1.66 is reported. A direct comparison to our observed exponent is complicated as we are lacking information about the third dimension and are quantifying an area size distribution of a physically three dimensional process. However, our findings fit nicely into the suggested universality discussion and support our assumption of fragmentation processes of larger inclusions during the forging process.

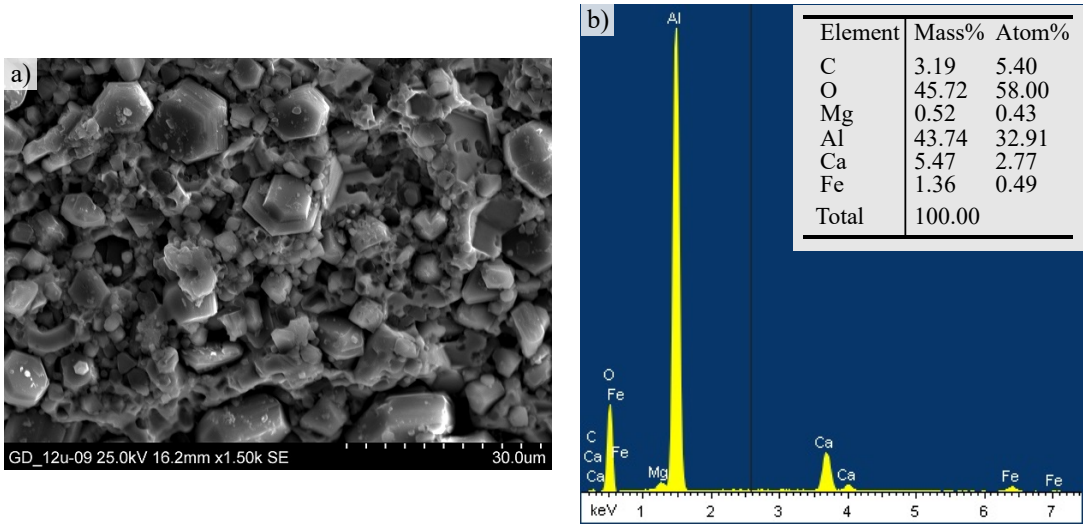

Figure 3.14.: (a) SEM image exhibiting the crystalline structure of a mixed-oxide inclusion at a magnification of 3000x. (b) Typical EDX images of inclusions. From the energy spectrum mass and volume percentages of atoms can be deduced.

Interestingly it was found that a similar power law distribution also applies to the size distribution of UT indications. This study is reported in Appendix A.

3.5.2. Observed Nucleation Cycles

Table 3.3 shows the main results of the experiments for some exemplar flaws. The first column contains the sample identification numbers, which are for internal reference only. Then the flaw typology is noted, the flaw size measured by area on the fracture surface, the testing temperature and the uni-axial load σ_{max} applied on the flaw. In general, the aimed maximum stress was slightly below the yield strength at the three temperatures (ca. 800 MPa (T_{RT}), ca. 700 MPa (T_1) and ca. 640 MPa (T_2)). In the last two columns the cycles to fracture and the nucleation cycles (expressed as a range) are reported, together with the fraction of the nucleation phase in percent. Many other measured features could be added to the table, such as the local stress at inclusion height, the distance of the flaw to the surface, the amount of cycles per load block, the shape of the flaws, the presence of additional flaws on the fracture surface etc. All this information is stored and compared in order to recognize trends and characteristics of the nucleation process. Some are discussed in the modeling sections in Chapter 4, others are reported in the following figures.

Figure 3.18 shows the results for 60 flaws in 45 different specimens. The observed number of nucleation cycles is plotted against the measured area of the flaw and also

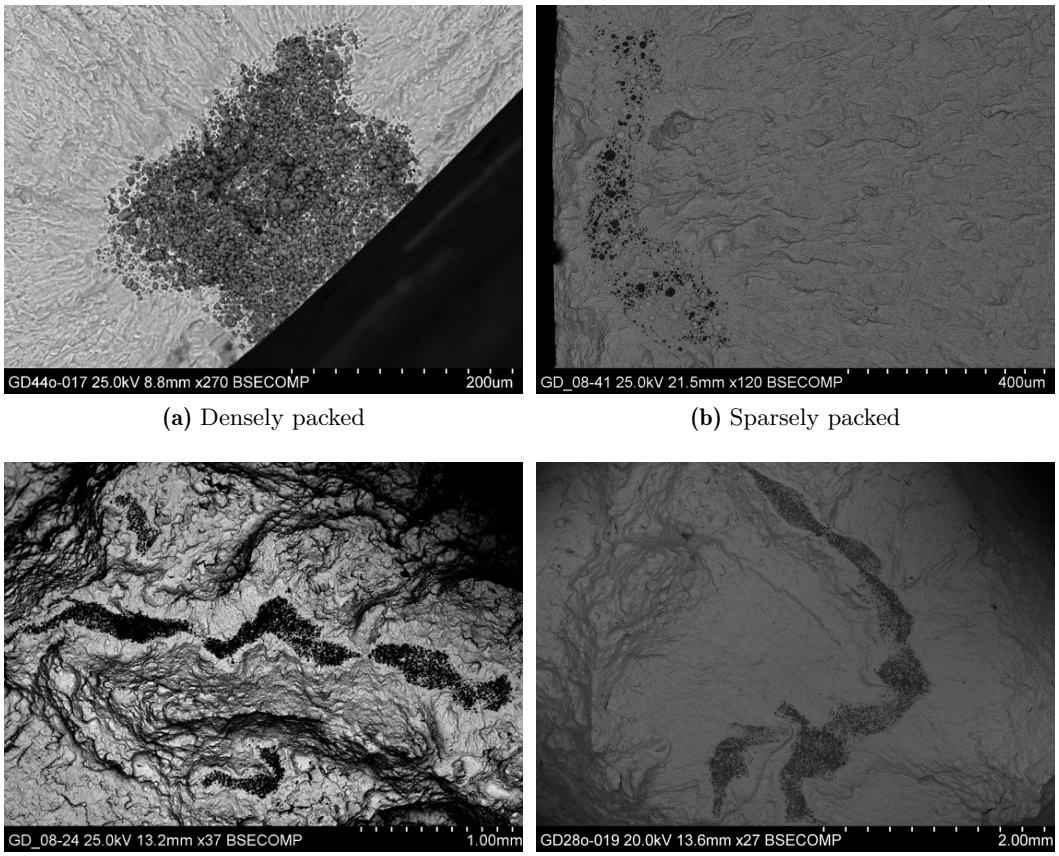

(a) Densely packed

(b) Sparsely packed

(c) Neighboring clusters

(d) Very long shape

Figure 3.15.: SEM images of a variety of clustered inclusions.

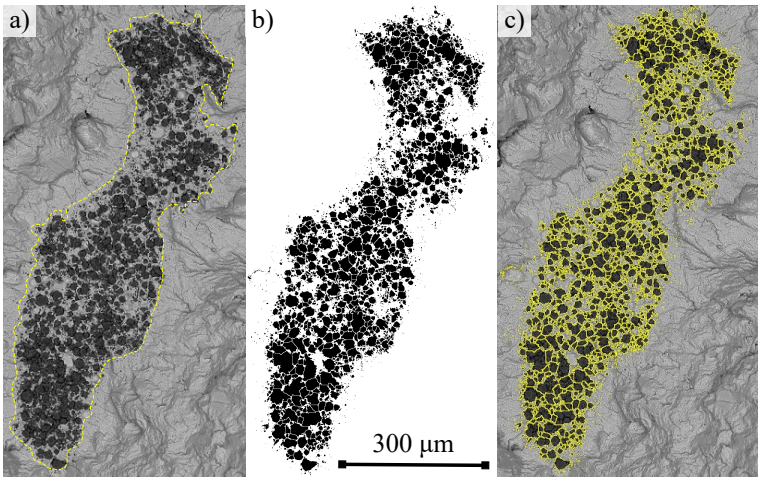

Figure 3.16.: Image segmentation (using ImageJ) on densely packed inclusion particles visible on the fracture surface, from Figure 3.13c. (a) BSE image of a cluster of inclusions. (b) Binarization by applying a threshold. (c) Watershedding divides cluster into separate particles.

ID #	Flaw Type	Area [mm^2]	Temp. [°C]	Load [MPa]	Fracture [cycles]	Nucleation [cycles] (frac.)
3	incl. (surf.)	0.337	T_{RT}	768	25374	12000–14000 (51%)
11	incl. (surf.)	0.186	T_{RT}	800	25702	12000–14000 (51%)
39	incl. (vol.)	2.400	T_{RT}	799	17434	4000–6000 (29%)
43	sep. (near surf.)	2.045	T_{RT}	740	48991	28000–30000 (59%)
46	sep. (surf.)	0.054	T_{RT}	801	33221	8000–10000 (27%)
47	sep. (surf.)	0.315	T_{RT}	801	19151	6000–8000 (37%)
48	sep. (surf.)	0.568	T_{RT}	801	19151	0–2000 (05%)
50	sep. (surf.)	0.936	T_{RT}	800	22199	10000–12000 (50%)
54	sep. (near surf.)	0.704	T_{RT}	801	19229	4000–6000 (26%)
68	incl. (surf.)	0.154	T_{RT}	802	30916	14000–16000 (49%)
69	incl. (surf.)	0.107	T_{RT}	801	35454	16000–18000 (48%)
79	incl. (surf.)	0.229	T_1	705	19297	4000–6000 (26%)
82	incl. (vol.)	0.526	T_2	640	74029	64000–66000 (88%)
86	incl. (vol.)	1.076	T_2	640	43674	30000–32000 (71%)
90	incl. (near surf.)	0.041	T_1	705	133640	118000–120000 (89%)

Table 3.3.: Exemplar flaws from the experiments. The flaw type is either 'separation' (sep.) or 'inclusion' (incl.) located in the volume (vol.) or (near-)surface (surf.). The indicated load is the maximum load at the flaw ($R = 0.1$). The column 'Fracture' reports the load cycles until fracture of the specimen occurred. The nucleation is given in ranges of 2000 cycles (between brackets is the fraction of the average nucleation time over the total amount of load cycles, see Figure 3.21b).

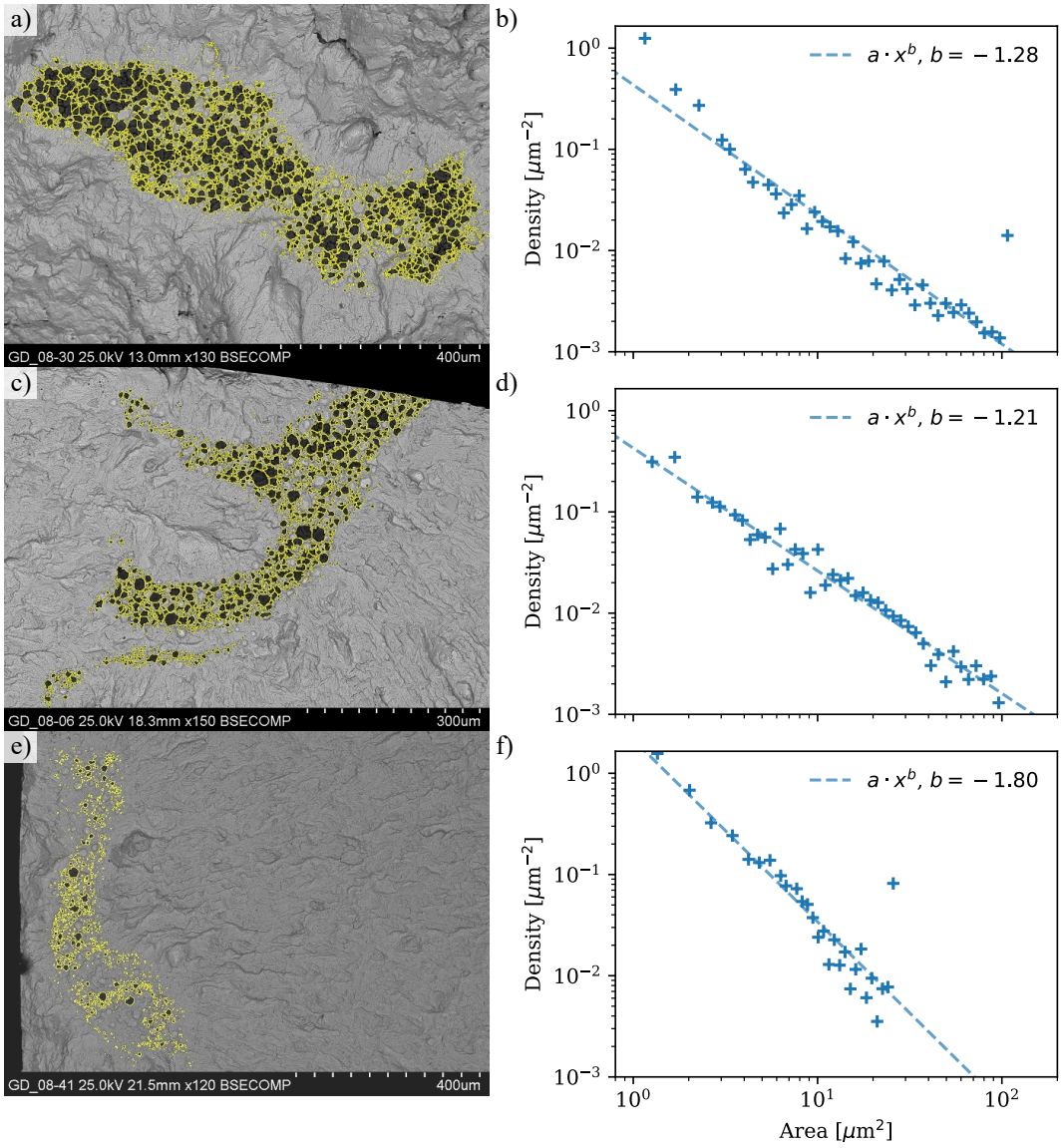

Figure 3.17.: Particle size distributions for exemplar flaws fitted to a power law with exponent b.

against the TFS of the flaw — defined as the diameter of an equivalent circle with the same area of the flaw. The TFS is a relevant parameter, since it is directly compared with the KSR size from the UT inspection, see Eq. (2.1).

The displayed data points are a selection of flaws that we will call 'primary flaws', since they unambiguously triggered the main fracture of the specimen as the beach marks reveal. Most specimens had one or more such defects with respective beach marks, other specimens had no clear beach marks to be counted, i.e. no nucleation time to be reported. The legend of the plot reflects most characteristics of the flaws. Note the following:

- Loading condition in MPa at the flaw location is marked with a number near the marker if it significantly deviates from the aimed loading (ca. 800 MPa (T_{RT}), ca. 700 MPa (T_1), ca. 640 MPa (T_2)).
- The flaw typology is in most cases an 'inclusion'. For 'separations' a small 'Sep' text is added near the marker.
- Some flaws were clearly not oriented orthogonal to the loading direction but rather parallel to it (e.g. Figure 3.19). Those flaws need to be carefully considered in the modeling phase and are noted with an 'X' on the marker.

The plot reveals some trends in the nucleation process. In general one could say that large flaws lead to short nucleation times. One could roughly draw a diagonal line through the scatter plot. This trend should be corrected by the loading condition, as high stresses and temperatures decrease the life significantly. Another trend is that surface flaws have shorter lives. A difference between 4-point bending tests and cyclindrical tension tests could not be observed. Separation types of flaws were only found in one forging, near the surface. They had in general shorter lives.

Three specimens had very short nucleation lives of 1000 cycles: two yielded due to high temperatures in combination with too high stresses of 800 MPa, one broke early due to a sharp edge in a large separation type of flaw at the surface.

Important to note is that the majority of the analyzed flaws were smaller than 1 mm in diameter. This also confirms the suspect that most flaws are actually not the ones from the UT indications; they may be either part of a larger group indication or, as explained before, they became primary flaws only due to their position at the surface of the specimen.

In Figure 3.20 we see the same flaws from Figure 3.18 with the nucleation time plotted against the Smith, Watson and Topper parameter P_{SWT}, where the loading condition on the flaws, with σ_{min} and σ_{max}, is corrected using Eq. (3.2). In the same plot the LCF results for standard specimens from Figure 3.5b are shown. As expected,

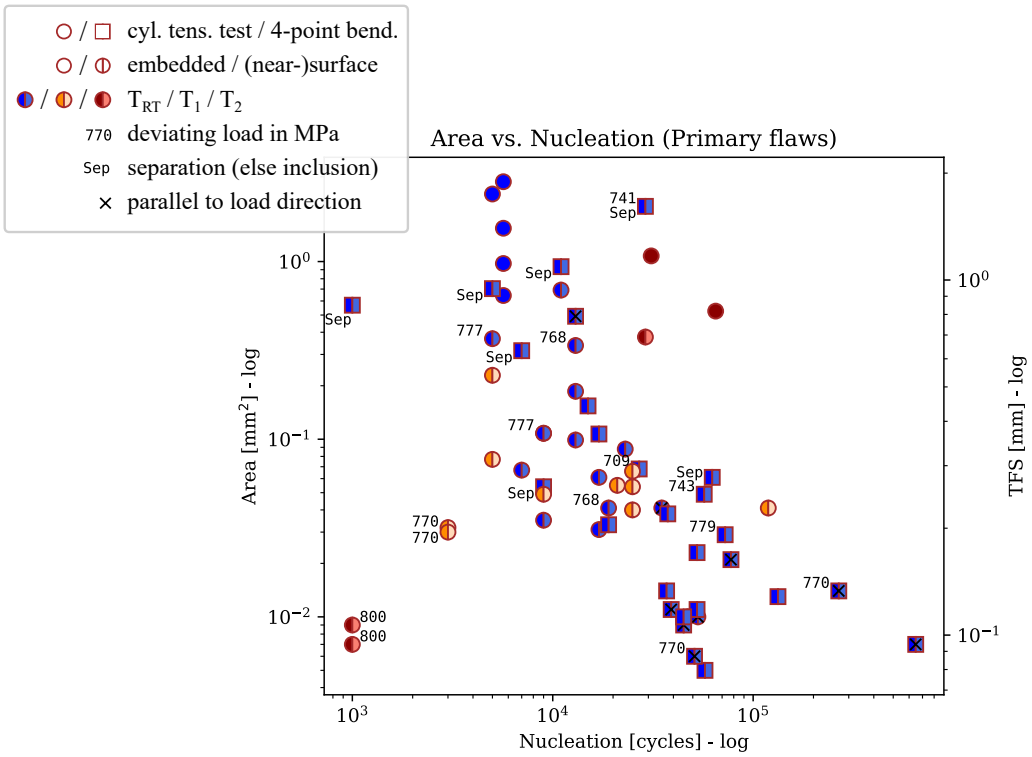

Figure 3.18.: Nucleation cycles from experiments for all primary flaws vs. flaw area (or also TFS) as measured from the fracture surface.

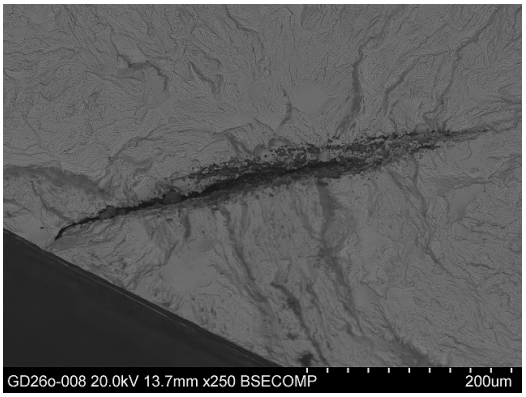

Figure 3.19.: SEM image of a defect oriented orthogonal to the fracture surface and parallel to the uni-axial load. Such flaws have a milder notch effect and do not represent the worst loading condition. Thus, they are non-conservative for the model calibration.

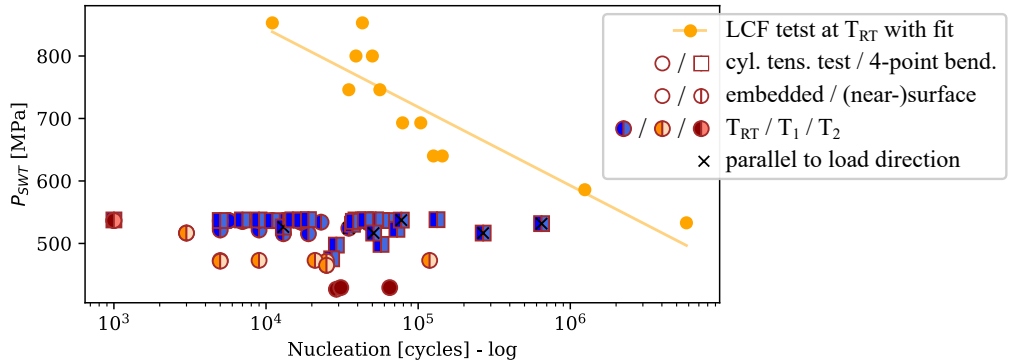

Figure 3.20.: Nucleation cycles from experiments for all primary flaws vs. applied load (damage parameter P_{SWT}) compared with the results of LCF specimens at T_{RT}.

the experiments on specimens including forging flaws have shorter lives. The flaws oriented parallel to the loading condition (marked with a 'X') have apparently such favorable orientation that they endure most cycles.

Figure 3.21a shows again the nucleation times of all the primary flaws with the addition of the remaining load cycles to failure of the specimen. Also the range of uncertainty, denoted as 'nucleation range' — when the first visible beach mark started back to when the preceding load block started, see Figure 3.10 — is visualized. This is in most cases 2000 or 4000 cycles; the size of a load block.

There are 4 flaws (from the same specimen) that had clearly nucleated and each of them initiated a long crack that collectively led to specimen failure. Unfortunately from the fractographic analysis there was no clear beach mark to be distinguished on the damaged surface. For this reason the nucleation time could only be generously estimated between 0 and 11340 cycles, which was the count at failure.

6 experiments had more than 100 thousand load cycles and did not fit the plot. For those flaws the fraction of nucleation cycles was considerably larger w.r.t. the remaining cycles that led to failure. A cross-check of these results with Figure 3.18 tells that these were all flaws with $TFS < 0.25\,\text{mm}$ or with an orientation orthogonal to the fracture surface. For this reason the nucleation took extremely long.

In Figure 3.21b the fraction of the nucleation time w.r.t. the entire amount of cycles until failure are plotted. From this plot it becomes clear that the portion of nucleation time is significant when compared to the crack propagation part. In most cases it amounts to more than 50% of the total time, with only few exceptions below 20%. One separation type of flaw had a very short nucleation life, suggesting that it was in fact already a sharp crack from the beginning.

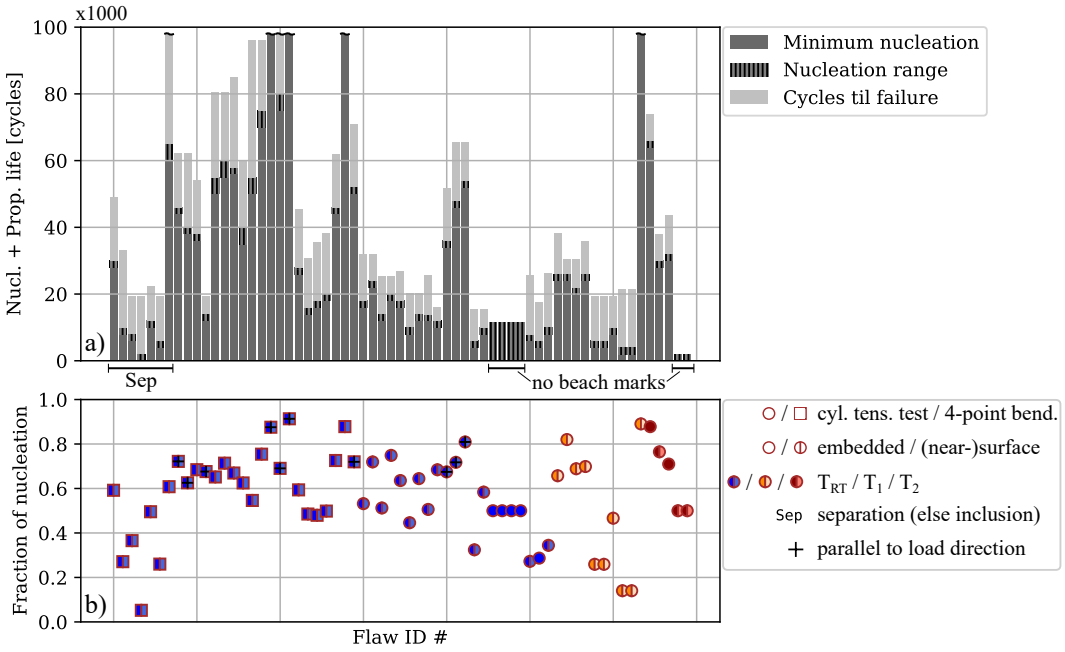

Figure 3.21.: (a) Each bar represents one of the 63 primary flaw with a nucleation part and a propagation part until the specimen breaks. The nucleation is in almost all cases determined up to a range of 2000 or 4000 cycles, denoted as 'Nucleation range'. The y-axis represents the absolute load cycles scaled by 'x1000'. (b) The same flaws are represented with markers. The y-axis represents the fraction of the average nucleation time over the entire amount of cycles till fracture.

Even though the failing specimen is not directly comparable with the failure criteria applied to an engineering component, it should be clear by now that the nucleation phase of the failure mechanism from a forging flaw is not negligible and that adding it to the component design could be very beneficial.

3.6. Discussion

Extracting valid specimens from the forged components is not a trivial task. Despite the challenges and difficulties, many specimens were successfully extracted and tested. More than 30 were tested at room temperature and 20 at higher temperatures. Of the tests performed at room temperature, only one did not exhibit clear beach marks on the surface. Approximately half of the tests at higher temperature were run-outs. They did not fail after a preset limit of more than 300000 cycles (one specimen was even tested at 1 million cycles taking more than one week!). Testing of those specimens was stopped due to time and cost considerations. The temperature was

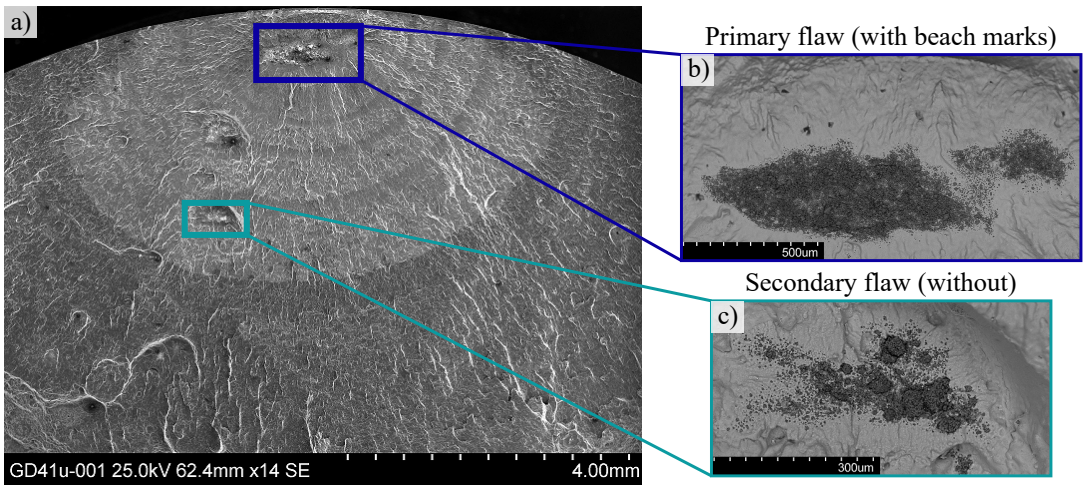

Figure 3.22.: (a) SEM image of fracture surface illustrating the difference between the (b) primary flaws, triggering the main fracture, and the (c) secondary flaws.

dropped to room temperature and testing was continued with higher stress amplitudes until failure. After failure there were beach marks observed and the nucleation time of the respective flaws could be established, conditional to the unusual load history of the specimen.

Since the amount of specimens is limited, in order to make the most out of them, also 'secondary flaws' on the fracture surfaces were analyzed. Of those secondary flaws there is no observed evidence of a nucleation time. Figure 3.22 shows how, for the secondary flaws, there are no beach marks to be counted. Nevertheless, from the nucleation time of the principal flaw, it can be deduced that the secondary flaws have at least the same nucleation time observed for the principal flaws (otherwise they would have caused the main fracture). These flaws can be somehow considered as run-outs.

On the other end there are some secondary flaws that visibly show crack initiation, but the main fracture with beach marks came from another flaw that overtook the 'competition'. For these flaws we have, as stated above, a minimum boundary for the nucleation time but also an upper boundary which is the total amount of cycles that led the specimen to failure. These considerations allow to use all the information we have at our disposal. Nevertheless, in order to remain conservative, such assumptions are only applied to flaws where the fractographic analysis was clear.

In Figure 3.23 these secondary flaws are sorted by size and minimum nucleation time in a similar way as in Figure 3.18. The arrows indicate an open end to the right. This plot, on the contrary of Figure 3.18, does not show particular trends in

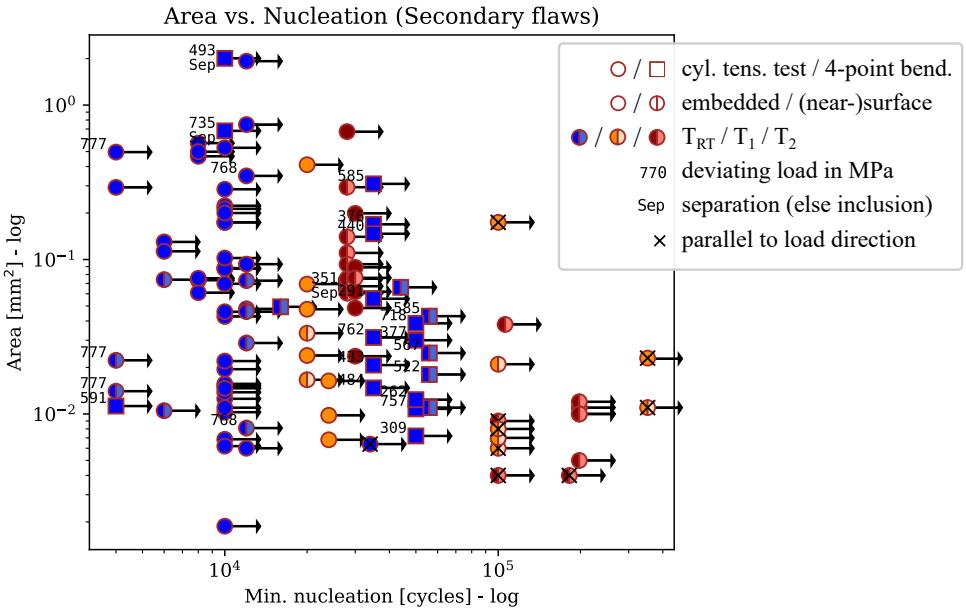

Figure 3.23.: Minimum amount of nucleation cycles of secondary flaws vs. flaw area as measured from the fracture surface. The arrows indicate that the experiments may be considered as run-outs with unknown upper bound. The minimum nucleation time is inferred from the primary flaws in the same specimen.

the nucleation behavior. This is due to the fact that only very limited information of the process is available for these flaws. This knowledge is not an exact knowledge, but even this censored data contributes to the calibration of the nucleation model under specific, conservative considerations, as discussed in section 4.2.5.

From the SEM images of the fracture surfaces many detailed information concerning the flaw's position, geometry and chemical composition was obtained. Besides the estimated amount of nucleation cycles, the aforementioned data are valuable for modeling purposes. The main geometric features and the loading conditions together with the nucleation times are used to set-up, validate and calibrate a model as described in the next chapter. From the trend of Figure 3.18 it becomes evident that the flaw size must play an important role within the modeling approach. One main geometric feature, though, which remains difficult to capture is the size of the flaw orthogonal to the fracture surface. This 'depth' information is difficult to measure *post mortem* and by NDT it cannot be assessed with sufficient accuracy. Incremental grinding has been discarded due to cost considerations and the risk of dropping the NMI particles while grinding. CT scans have been performed on some flaws, without success. The

depth dimension will play a key part in the calibration of the model.

Since we can only measure the area of the flaw projected on the fracture surface, we use this as starting point for modeling. Keep in mind, though, that this specific cross-sectional area is not necessarily the largest area projection of the flaw. It may be that somewhere, below the fracture surface, there is a larger cross-section to be found. One would expect that the specimen breaks at the largest extension of the flaw, where the matrix material is the weakest. Other, local effects may be more detrimental, such as the crystalline structure of a NMI particle or other microstructural features. In any case, underestimating the area of the flaw leads to conservative results in the calibrated model. The area is slightly underestimated while calibrating, leading to an underestimation of the model's predictions w.r.t. the expected nucleation life.

Also important to keep in mind is that not all the specimens were obtained in the most critical — thus the most desired — orientation w.r.t. the flaw, see e.g. Figure 3.19. In such cases, the results must be accepted with caution. Discarding such outliers would still lead to conservative results, since they are oriented optimistically w.r.t. the principal load direction.

4. Probabilistic Forging Flaw Nucleation Model

In Chapter 1 the state-of-the-art designing methodology for rotor components has been described. Inherent forging flaws undergoing cyclic loading may initiate a crack which propagates until component failure. At present, this failure mechanism is accounted for in design by modeling the crack propagation only. The crack nucleation, or crack initiation from the forging flaw, is basically neglected. The conservative underlying assumption is that the flaw can be represented by a sharp crack already from the beginning. The lifetime of the crack can then be calculated using fracture mechanics with a starting crack size equal to the TFS, inferred from UT.

The experiments described in the previous chapter proved that neglecting the nucleation time is normally overly conservative. In this chapter, first a general two phase description for the failure mechanism is postulated. Then, focusing on the nucleation phase, three probabilistic models are presented that account for the nucleation time of the single forging flaws. These models are calibrated and validated with the experimental data and made robust by sensitivity analyses. Finally one model is integrated, together with a probabilistic fracture mechanical model, into the design tool *ProbFM*, able to predict the entire life cycle of a forging flaw. In Chapter 5 the tool is applied to a simplified rotor component first and then to a more complex real-life rotor disk component.

4.1. Life cycle of a Forging Flaw: Two Phase Description

In the literature there are several approaches describing the life cycle of a component. As mentioned in Section 2.4, the total fatigue life, N_F, is conventionally divided in two terms:

$$N_F = N_i + N_p \tag{4.1}$$

The initiation life N_i and the propagation life N_p of a crack. For the forging flaw, we follow the same approach. The two processes of crack nucleation followed by crack growth until failure of the material under cyclic or static loading are schematically illustrated in Figure 4.1. This process can be captured by the following expression:

$$N_{flaw} = N_{Nuc} + N_{FM} \tag{4.2}$$

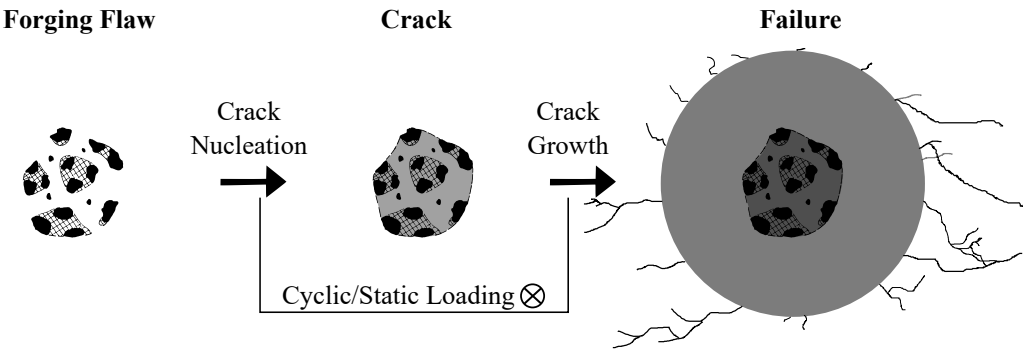

Figure 4.1.: Example illustration of the life cycle of a forging flaw: Under cyclic (and/or static) loading the area of NMI first nucleates into a crack before subsequent crack growth will lead to component failure.

where N_{flaw} is the total lifetime of the flaw in cycles, split into a nucleation part N_{Nuc} and a fracture mechanics part N_{FM}. Both are dependent on the flaw geometry and the local loading conditions and temperatures in the component.

If we follow the stages in the fatigue life presented by McDowell et al. [51] (see Eq. (2.6)), the nucleation phase can be represented by the entire amount of cycles that the material imperfection needs to incubate into a micro-notch root scale crack, further propagate in a microstructurally small crack and finally, through a physically small crack, into a long crack. In our present modeling approach, the crack propagation phase equals N_{LC} and is probabilistically computed with LEFM as described by Amann [4].

$$N_{LC} = N_{FM} = N_p \tag{4.3}$$

With the above, McDowell tries to confine the failure mechanism in clearly defined phases, which in reality are hard to distinguish. From an experimental point of view it is not (yet) possible to quantify the different stages described above. The distinction between crack incubation and microstructurally small crack could be simulated in multi-scale models. But it would be difficult to calibrate such models with experimental observations, since the latter are not measured in our case. For this reason we stick to a two-phase approach where the nucleation phase is defined as the amount of cycles needed to initiate a crack with a length in the order of magnitude of the forging flaw itself. The crack propagation phase is when the long crack grows further outside of the initial flaw area. Figure 4.2a is a SEM image of an etched surface of the studied 26NiCrMoV14-5 steel. It has a very fine ASTM 6 grain size, which corresponds to ca. 45 µm. Since we did not have a similar etched surface with also a flaw on it at our disposal, we try to compare the forging flaw with a sketch of the grain structure

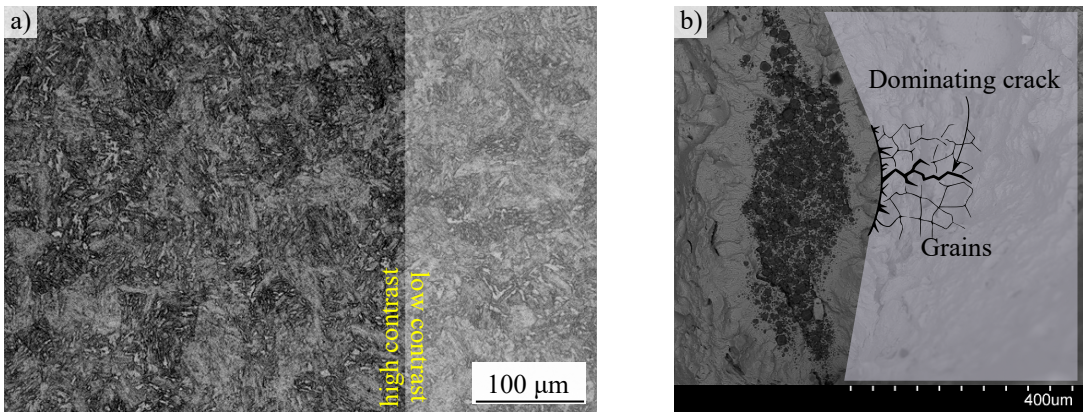

Figure 4.2.: (a) SEM image of etched surface. The grain structure has grains of ASTM 6 size. (b) NMI with sketch of sized grain structure and microcrack initiation.

in Figure 4.2b. The left part of this figure shows a forging flaw with its many fragmented particles. On the right part we inserted the sketch from Figure 2.4, resized to realistically illustrate the grain size scale compared to the inclusion size. This visualization shows that the entire flaw area is roughly one order of magnitude larger than the single grain, but the single flaw fragment is of the same size of the grains (if not smaller). The macroscopic crack initiation described by the CMB formulation (eq. 2.2) fitted to LCF tests normally describes larger cracks of 1–2 mm. Applying this formulation to cracks as illustrated by the sketch of Figure 4.2b is a bit of a stretch of the physical model. Considering that we aim at 'effectively' describe the process of crack nucleation, and we do not have experimental data on shorter crack formation at hand, we proceed in describing the macroscopic crack initiation from flaws with the CMB formulation, normally applied to larger cracks. The resulting model is finally calibrated to the experiments on forging flaws and eventual modeling imprecisions or offsets are corrected this way. One great advantage of applying the CMB formulation based on LCF tests is that this kind of data is largely available for most materials applied in engineering. This characteristic will help to apply the presented nucleation models also to other metals in the future.

The sketches of Figures 4.1 and 4.2 help to conceptually separate the two phases which can be distinguished from the experiments: the first, where no beach marks are formed; the second, where beach marks are visible and the crack propagates outside the region of the flaw.

The design tool *ProbFM*, presented by Kadau et al. [4; 38], conservatively assumes the nucleation phase to equal zero: $N_{Nuc} = 0$. The aim of this study is to develop a crack nucleation model that probabilistically quantifies the nucleation duration and

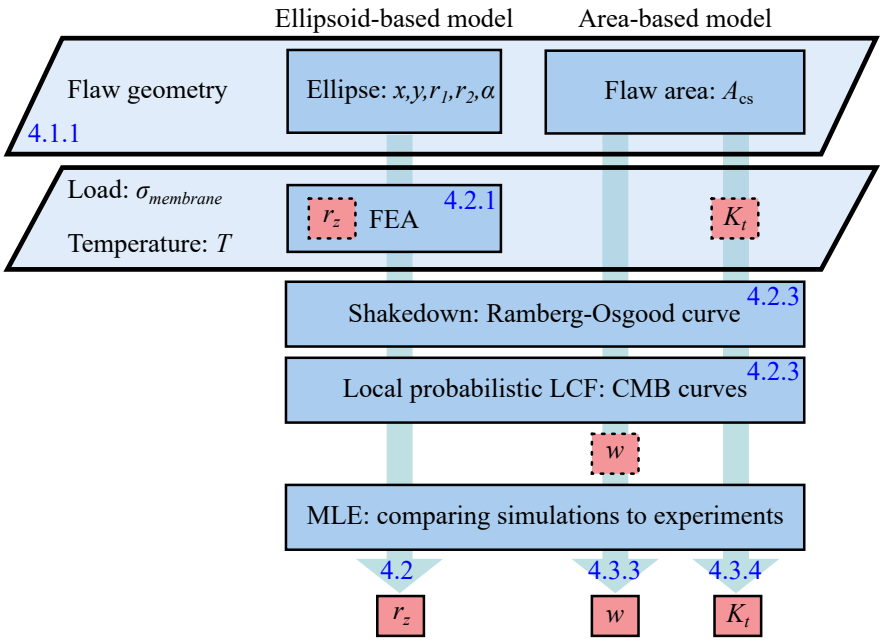

Figure 4.3.: The flowchart depicts the three main modeling approaches pursued during the research: the 'ellipsoid-based' model and the 'area-based' models with w and K_t parameters. The details of each are reported in the respective sections marked in blue.

relieves part of this conservatism. It still remains a fundamental model requirement to be conservative, if we keep in mind the application of forgings in heavy duty gas turbines and the enormous consequences of eventual failure of a disk w.r.t. human injury, environmental damage and asset loss.

The various modeling attempts have been presented in a series of three publications [69–71]. The aim of the models is to effectively and probabilistically represent the nucleation process of forging flaws. The model must account for the main parameters influencing the nucleation process which are the flaw typology, size and geometry, as well as the matrix material behavior under different loads and temperatures. Since the detailed geometrical features of flaws and also the loading conditions can become quite complex, the model should capture those features in an effective rather than a detailed way.

The three arrows in the flow diagram of Figure 4.3 refer to the three modeling approaches presented in this chapter. The details of the several steps are contained in the respective sections, written in blue. The red highlighted boxes contain the variables that are used for calibration in the respective modeling approach.

4.1.1. Effective Flaw Geometry

The flaws can have very complex geometries, as discussed in Section 3.5.1 and illustrated in Figure 3.13. In order to reproduce the details of the single crystals of the flaws and the corresponding stress concentrations and fracture mechanisms, one should model the flaw in the meso- or even in the microscale as proposed by several authors, e.g. Jian et al. [36]. This goes beyond the scope of the current research, nevertheless, the experimental results were used in a collaboration project between Siemens Energy and the Los Alamos National Laboratories to run peridynamic simulations as discussed in Section 4.2.7 and presented by Karim et al. [74; 75].

When considering large forged components, the only available information on flaws is the presence of a UT indication after NDT or not. Based on this indication, the size of the flaw and its main orientation can be estimated within millimeter precision. The proposed modeling approach should ideally use only this information as input. This requires strong simplifications of the flaw geometry. Every additional degree of complexity and corresponding additional model parameter cannot be inferred from UT indications and can therefore not be a design variable in the proposed model.

Nevertheless, owing to the destructive testing campaign presented in Chapter 3, we gained good insight on the specific geometries of flaws, their several typologies and respective probabilities and locations of appearance. These recognized trends and generalities should be embedded into global model parameters and the model fitted, such that its behavior reflects the experimental results. Still, keeping the amount of design variables to a minimum.

An effective geometry for describing irregularly shaped flaws, which is widely applied in literature, is the ellipse, see for example Prasannavenkatesan et al. [67] or Chapter 2 of Murakami [56]. There are several ways to fit an ellipse to the flaw geometry found on the fracture surface. According to Stojmenovic [94], the methods can be split into shape(or boundary)-based and area-based. The shape-based methods only consider the boundaries of the shape to be fitted and tend to overfit all the variations of the boundary points, leading to unsatisfactory results for geometries with irregular shapes as illustrated in Fig. 4.4a.

For the area-based methods the entire inner area of the geometry is considered (this requires a closed shape). They are less sensitive to abrupt variations of the boundary since they account for the 'mass' of all the pixels within the geometry. The area of the fitted ellipse matches the area of the random geometry. For some forging flaws this fitting is problematic; when the flaws are not continuous and there is a lot of matrix material in between, the ellipses tend to be too small, see Figure 4.4b.

Of course, there are also flaws which can be perfectly fitted with both approaches, because the shape is already elliptical, see Figure 4.4c.

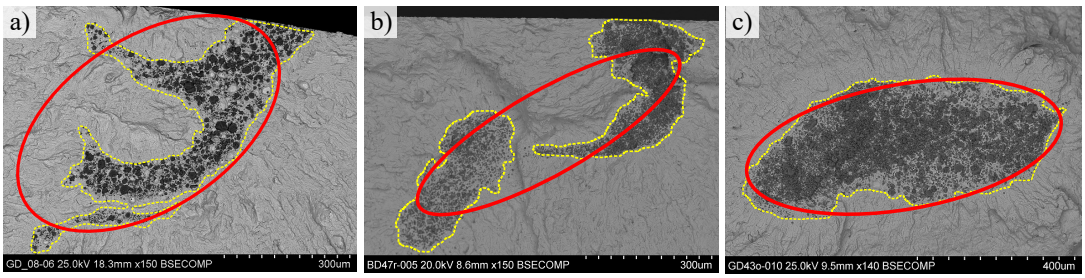

Figure 4.4.: Flaws are modeled with effective ellipse shapes. (a) Problematic shape-based fit. (b) Problematic area-based fit. (c) Ideal ellipse fit.

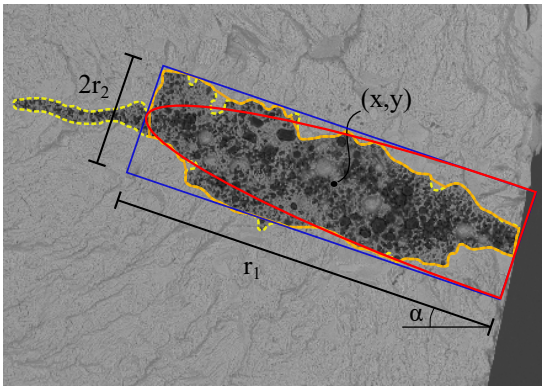

Figure 4.5.: Surface flaw modeled as an halve ellipse. The flaw area is manually traced (yellow, dashed line). The complex flaw geometry is then simplified (orange line). By means of a bounding box (blue rectangle), the ellipse is derived with ca. the same area as the original flaw (red halve ellipse).

It is not easy (if possible at all) to develop an automated flaw recognition algorithm and consequent ellipse fitting that suits all possible flaw typologies and geometries; a one-size-fits-all solution. For this reason — and because the amount of flaws in question is contained — some flaws are manually encapsulated in an area of interest which is then approximated by an ellipse with use of a bounding rectangle. Figure 4.5 illustrates this procedure. The complex geometry (dashed yellow line) is manually simplified excluding small features (solid orange line). Then, a minimum bounding rectangle is defined around the boundary. The 5 parameters defining the semi-ellipse are contained in the rectangle definition: location coordinates (x, y), major and minor radii (r_1, r_2) and orientation angle (α). The flaws are approximated by ellipses in case of volume flaws and by semi-ellipses in case of (near-)surface flaws (Figure 4.6).

The depth direction of the flaw is the direction orthogonal to the fracture surface, which coincides with the loading direction of the specimen. Unfortunately, this geometrical feature is difficult to measure. It is impossible to unambiguously infer this

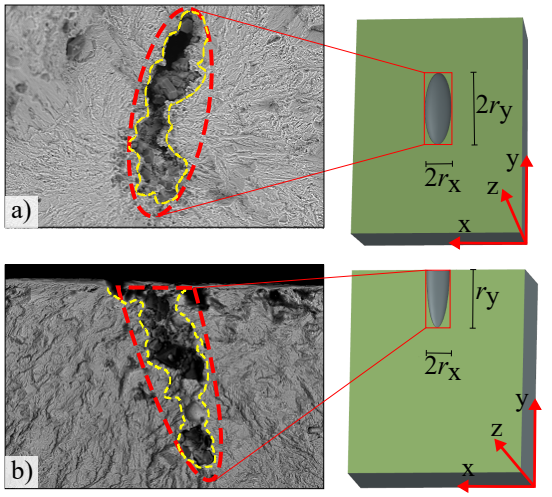

Figure 4.6.: For modeling purposes embedded flaws are represented by (a) ellipses and (near-)surface flaws by (b) semi-ellipses.

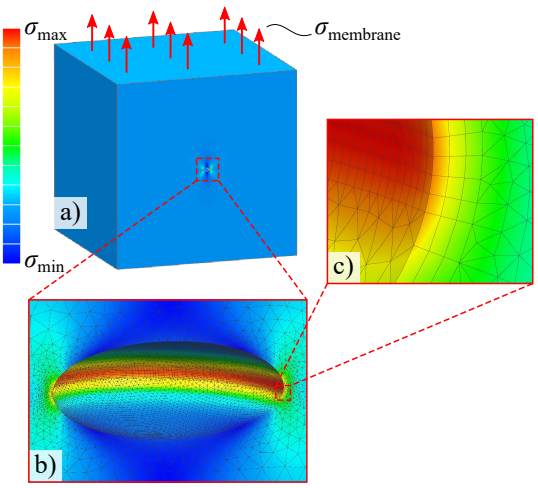

Figure 4.7.: (a) Uni-axial load, or membrane stress, applied to an embedded ellipsoid. (b) Stress distribution on the surface of the ellipsoid. (c) Mesh refinement at the locations with high stress gradients.

size parameter from the SEM image of the fracture surface. This unknown, important geometric feature of the flaw will be used as calibration parameter in the 'ellipsoid-based' nucleation model. In the 'area-based' nucleation model we will only use the cross-sectional flaw area measured on the fracture surface of the sample; no other geometrical features are needed.

4.2. Ellipsoid Based Nucleation Model

The first model to be discussed is the ellipsoid-based nucleation model, in which the flaw and its surrounding matrix material is modeled as a large cube of matrix material with an ellipsoidal void representing the flaw.

4.2.1. FEA

For the flaws characterized as 'separations', there is no second phase material involved; the flaw consists of a discontinuity of the matrix and may therefore be modeled as a pore or a void.

The flaws categorized as 'inclusions', on the other hand, do have a second phase material involved. Since we lack all sort of information about the specific material characteristics of those NMIs (Young's modulus, bonding properties, ligament between

the particles etc.), we cannot model the flaws as inclusions consisting of a second phase material; instead, we model also the 'inclusion' type of flaws as pores in a single phase matrix. This approach is also advocated by Murakami [56] and Schäfer et al. [81].

The size of the cube surrounding the ellipsoidal void is chosen large, such that the stresses on the boundaries are nearly homogeneous and are not influenced by the notch caused by the void. A size 10 times the size of the major radius of the ellipsoid suffices. The volume is modeled and meshed in a FEM model with special attention to sharp curvatures near the void. The cube is meshed with rather uncoordinated 10-node tetrahedral structural solid elements with quadratic displacement behavior in the far-field zone. Near the void, at the notch (where the stresses are highest) the volume is meshed with 20-node hexahedral elements and the remaining near-field zone is meshed with 15-node prisms. Pyramid elements are needed as transition pieces between hexahedrons and tetrahedrons. Near the void, brick elements are used in order to have better grip on the meshing algorithm even when the flaw size is altered and assuring a regular grid with valid element shapes and sufficient integration points where stress gradients are high. Those details are visually illustrated in Figure 4.7.

The same figure also shows the solution of the FEA for a given uni-axial far-field load and uniform temperature. One load cycle is defined by a minimum and a maximum load at constant and uniform temperature. The model will be calibrated with the same uni-axial loads and temperatures as in the experiments; for the engineering application of the model we must consider the real components and their complex multi-axial loading conditions and temperature gradients; this is discussed in Section 5.2.1.

4.2.2. Material Model

The base material has been characterized during the testing campaign and compared to the thorougher Siemens Energy proprietary material database. The resulting material model was presented in Section 3.4.1 and resumed in Table 3.2.

4.2.3. Stresses, Shake-down and LCF

The applied loads in combination with uniform temperatures cause a stress field around the ellipsoidal void. This typically has low compressive stresses at the two poles on the axis along the uni-axial load direction. Those are the areas that are less prone to fail due to fatigue. Then there is the high tension area which goes all around the equator line, orthogonal to the load direction. This is the area with the highest probability of crack initiation due to cyclic loading. The proposed model assumes the crack nucleation process to be LCF driven. The load assumption for LCF crack initiation normally rests on the maximum distortion energy criterion, or von Mises yield

criterion [52]. In ductile materials, the hydrostatic pressure is not considered relevant for generating dislocations. Only deviatoric stresses are held responsible for dislocations. The stress tensor, $\{\sigma_{11}, \sigma_{22}, \sigma_{33}, \sigma_{12}, \sigma_{23}, \sigma_{31}\}$, is represented by the equivalent von Mises stress:

$$\sigma_{vm} = \sqrt{\frac{(\sigma_{11} - \sigma_{22})^2 + (\sigma_{22} - \sigma_{33})^2 + (\sigma_{33} - \sigma_{11})^2 + 6(\sigma_{12}^2 + \sigma_{23}^2 + \sigma_{31}^2)}{2}} \tag{4.4}$$

Figure 4.7 shows the von Mises stresses around a semi-ellipsoidal void caused by the uni-axial load on the cube. The shown results are obtained with linear elastic simulations; this causes the stress-field around the ellipsoid to be directly proportional to the applied uni-axial load at the top of the cube. One load cycle, with a minimum and maximum membrane stress, $\sigma_{membrane}$, translates into a minimum and maximum stress-field around the ellipsoid. The use of linear elastic simulations is only justified if the local stresses remain smaller than the yield stress σ_y, or if a shakedown method is applied, which artificially translates elastic strains into elasto-plastic strains. Most shakedown methods are based on energy preservation assumptions. In this study we apply a variation of the Glinka method which also accounts for the cyclic stress-strain behavior of the material, see [28; 42; 53]. The main reason for applying shakedown methods is that they spare the use of computationally expensive elasto-plastic simulations.

The local probabilistic LCF method, described in Section 2.6, is used as post-processing on the elasto-plastic strains of surface $\partial\Omega$, from the FEA including shakedown. The probability for crack initiation, anywhere on the surface, is given by the Weibull function (2.10) with shape m and scale η, see Figure 4.8b for an example. η is obtained by a high order numerical integration of all the hazard densities over the curved surfaces, see Eq. (24) of [83]. Eq. (2.15) can be approximated with a summation over all integration points k, and expressed as

$$\eta = \left(\sum_{i=1}^{k} \left(\frac{1}{{N_{i_{det}}}^m} A_i \right) \right)^{-\frac{1}{m}} \tag{4.5}$$

All the hazard densities times their area weights are summed. The hazard densities are obtained by solving the CMB equation (2.3) for the elasto-plastic strain amplitudes at each integration point on surface $\partial\Omega$. The result for a halve-ellipsoid is shown in Figure 4.8a, where the hazard densities at all integration points are displayed.

Every combination of minimum and maximum load, uniform temperature and geometrical feature of the flaw results in specific η, defining a Weibull distribution for

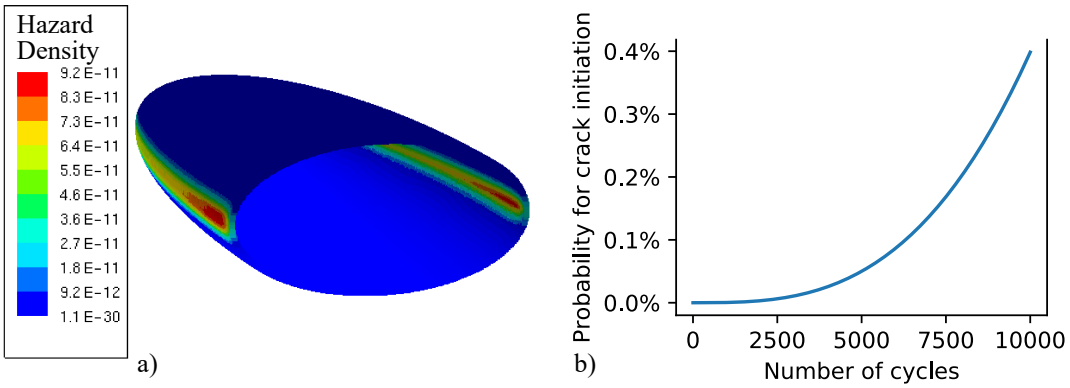

Figure 4.8.: (a) Hazard density on the surface $\partial\Omega$ of the ellipsoid representing the flaw. (b) Example for probability of crack initiation from the flaw as a function of load cycles N represented by a Weibull distribution ($m = 3$ and $\eta = 50000$, used for illustration purposes).

the nucleation time of that flaw. Since m remains unchanged, only η defines the Weibull distribution of Eq. (2.10). For this reason the sensitivity study in the following sections focuses on η only, which is an alternative measure for the amount of nucleation cycles. In probabilistic sense, η coincides with the 63^{rd} percentile of the Weibull distribution.

4.2.4. Sensitivity Study

In this section a sensitivity study of the ellipsoid-based nucleation model is presented. The reference-case is a spherical pore with a radius of 1 mm, an applied uni-axial load range of 80–800 MPa ($R = 0.1$) at 20 °C. The material model reflects the investigated high-strength rotor steel. Maximum applied temperature is 500 °C and the yield strength of the material is ca. 800–900 MPa.

Element Size

Since the highest risk regions are always at the locations with the highest stress concentrations, these 'equatorial' areas have to be described by a refined mesh, see Figure 4.7c. A FE mesh convergence study has been performed in order to capture the gradient and stress concentration more accurately. This guarantees a reliable description of the notch effect and the statistical size effect. Figure 4.9 shows the convergence of η for an increasing amount of elements in the 'equatorial' area. The x-axis refers to the amount of rows of hexahedral elements along the equator line. This is shown here exemplary for one flaw geometry and has been repeated also for variations of geometries. Increasing the amount of elements comes at the expenses of

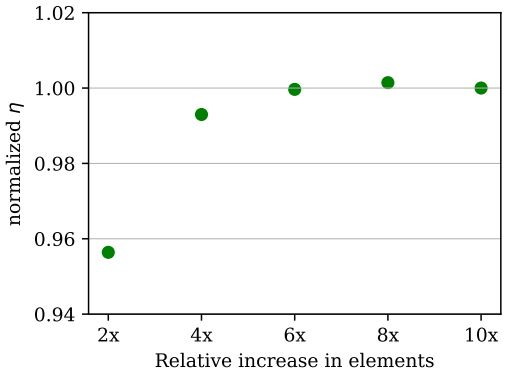

Figure 4.9.: By increasing the amount of hexahedral element rows along the 'equator line', the resulting η stabilizes and converges.

computational time. In order to keep the final amount of elements as low as possible amount of hexahedral element rows is set to 8. Depending on the geometry, some FEM models reach the million of elements in total.

Temperature

The model is in theory able to include inhomogeneous temperature fields. In practice, for our application, the effect of a temperature gradient on component scale is negligible when projected to the small scale of the flaws. For this reason only uniform temperatures are applied in the present study. The red line in Figure 4.10 shows the effect of varying this temperature on the nucleation life, expressed in η. Starting from the base case at room temperature, the LCF process lasts shorter for increasing temperatures and the Weibull scale parameter η decreases proportional to the temperature model parameterized with the CMB formulation, until reaching the service temperature limits for the given material.

The vertical axis has been normalized in order to keep the quantitative results confidential. η_0 marks the Weibull scale parameter of the reference base-case.

Load Variation

A large impact on the nucleation time is given by the applied load. The load cycles are described by a minimum and a maximum load, which may interchangeably also be defined using the load amplitude $\sigma_a = \sigma_{max} - \sigma_{min}$ and the load ratio $R = \frac{\sigma_{min}}{\sigma_{max}}$. The blue and the orange lines in Figure 4.10 show how η changes with varying σ_{max} and R, respectively. Increasing σ_{max} or decreasing R leads to an increase of ε_a, which in turn leads to shorter LCF lives following Eq. (2.3). Increasing σ_a would result in

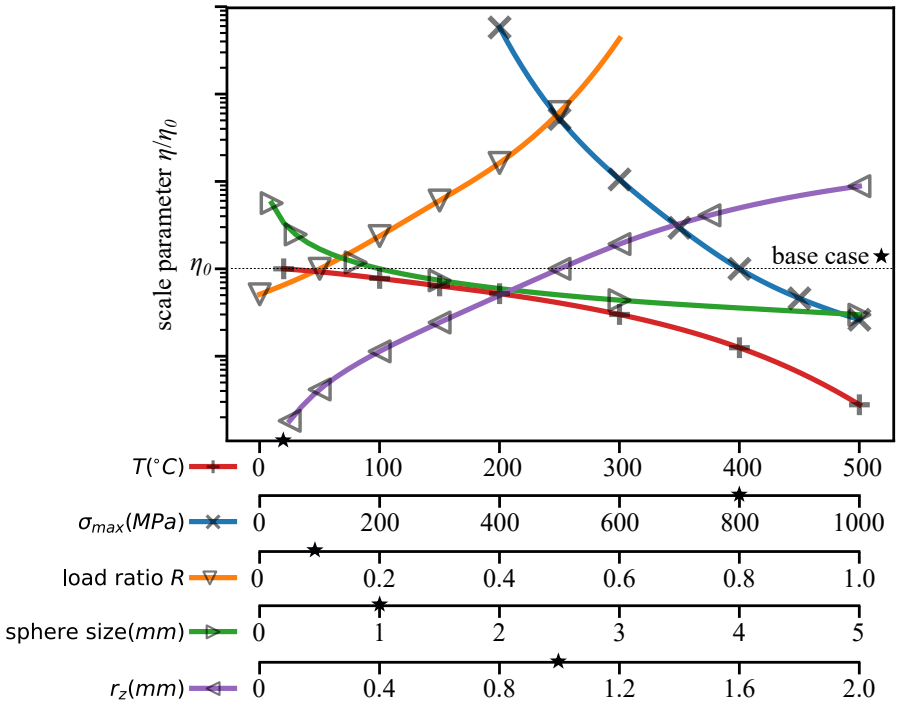

Figure 4.10.: Response of the Weibull scale parameter η on varying input parameters.

the same trend. In higher stress zones this effect is even more detrimental due to plasticity. At low stress zones the LCF life may even get into the so-called endurance limit, preventing the flaw from nucleating at all.

Size-Effect

One interesting feature of the model is that it reacts to the size of the flaw. The PoF is proportional to the size of the stressed area. If we consider two flaws with the same shape but different absolute size A_1 and A_2, their linear-elastic stress-field will look identical under the same loading conditions. The only difference is the size, which causes the nucleation time (expressed in η) to relate according to

$$\frac{\eta_1(A1)}{\eta_2(A2)} = \left(\frac{A_2}{A_1}\right)^{\frac{1}{m}} \tag{4.6}$$

This relation is confirmed by simulations with varying flaw diameter. The green line in Figure 4.10 shows this effect. The functional relation between the radius and η is indeed a power-law as in Eq. (4.6). At small sizes, parameter η considerably increases and with it also the expected nucleation time of the flaw. This behavior reflects

the experimental observations, already shown in Figure 3.18, where small inclusions have longer nucleation lives than larger ones, making the latter more dangerous for components.

z-Radius

The shape of the ellipsoidal pore can be manipulated by its 3 axes of which the z-axis is parallel to the applied stress and the x- and y-axes are orthogonal to it and can be measured experimentally, see Figures 4.5 and 4.6.

The 2D representation of flaws, as they appear on the fracture surfaces of specimens, are modeled by means of the r_x and r_y radii of the ellipsoids. The lack of the depth information is taken as an opportunity to use the z-radius, r_z, as a calibration parameter for the model. The expectation is that for different types of flaws, different values for r_z would apply.

Note that r_z is a mean to express the sharpness of the radius of the flaw. In the limit of $r_z \to 0$, a sharp crack is modeled; the nucleation time approaches zero due to the high plastification at the originating crack front; the crack immediately starts propagating in a fracture mechanical sense. By taking the other extreme, $r_z \to \infty$, there will be no stress concentration at all. The stress around the flaw is streamlined and the nucleation time approaches the regular LCF life of the flawless matrix material. This effect is illustrated with the purple line in Figure 4.10.

Distance to Surface and a/c-Ratio

A perfectly embedded flaw can be modeled as an ellipsoid with a large distance to the free surface, such that the stress field on the free surface remains unaltered. Most flaws from the experiments — and also critical positions within rotor disks — are at the surface or near the surface. A sensitivity study will illustrate the influence of the distance to the surface on the nucleation life.

In Figure 4.11 we see the modeled flaws for three different a/c-ratios. c is the ellipse radius orthogonal to the free surface and a is parallel to it. This is the notation normally used in fracture mechanics; it coincides with the previously defined r_x or r_y radii for the ellipsoid. The upper ellipses depict flaws with distance $k \cdot c$ to the surface. This distance is decreased until the ellipse almost touches the border. At this point a singularity arises in the FEM model: the ligament between the ellipsoid and the free surface becomes extremely small, causing immediate plastic collapse of the matrix material. The local probabilistic LCF calculation returns a lifetime approaching zero. In reality the plastic collapse of that ligament does not imply the end of the nucleation time, since the crack cannot grow any further in that direction. Instead,

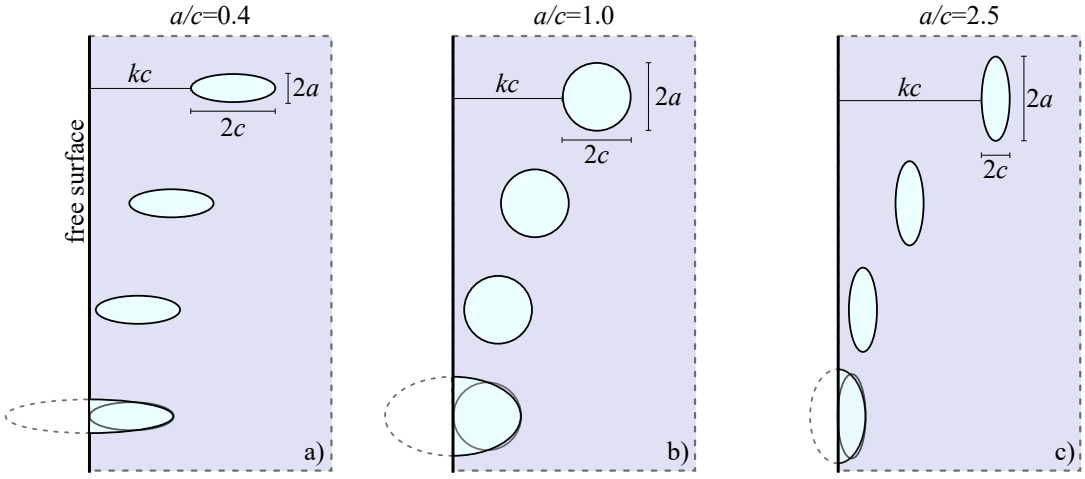

Figure 4.11.: Ellipse at varying distance ($k * c$) from the free surface with (a) $a/c = 0.4$, (b) $a/c = 1.0$ and (c) $a/c = 2.5$.

this asymptotic situation can be captured by modeling an half-ellipsoid encapsulating the entire ellipse and the ligament. Radius c will more than double and a slightly increase, as illustrated in the lower part of the figure.

The effect on η is plotted in Figure 4.12. At distances approaching zero, η rapidly decreases, see, e.g., the blue marker surrounded by a red circle. Instead of those collapsed values of η, I propose to take η applicable to the half ellipse (left in the plot) as minimum. At distances larger than $3 \cdot c$ the influence of the free surface clearly diminishes. If we take the half ellipse as one extreme case on one hand and the fully embedded ellipse as extreme on the other hand, we can spare some (near-)surface simulations by applying a correction factor to η obtained with simulations for fully embedded flaws. Dividing η for embedded flaws by η for the half ellipses (for the three different a/c-ratios) gives three correction factors, see Table 4.1. The most impacting factor applies to flaws with $a/c > 1$. Based on those findings we can model (near-)surface flaws as embedded flaws and simply apply this conservative factor for distances smaller than e.g. $3 \cdot c$, instead of trying to solve the complex singularity situation or to distinguish between full ellipsoids and halve ellipsoids.

a/c-ratio	correction factor
0.4	0.74
1.0	0.60
2.5	0.44

Table 4.1.: Conversion factors for (near-)surface flaws at different a/c-ratios.

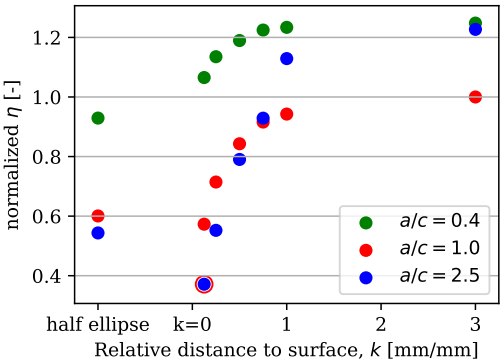

Figure 4.12.: Plot of the normalized Weibull scale parameter, η, at varying distance to the free surface for different a/c-ratios.

Interesting to note is that flaws with $a/c = 0.4$ and 2.5 have similar life expectations for embedded flaws, but very different expectations near the surface. This can be explained due to support effect that deep surface flaws with $a/c < 1$ have from the matrix material in direct proximity of the surface. This leads to rather mild strain amplitudes in those regions and only high amplitudes at the small tip of the half-ellipsoid. For shallow surface flaws with $a/c > 1$, the topography in direct proximity of the surface is much more 'open'. This prevents a supporting effect, resulting in sustained strain amplitudes along the entire halve-equator line of the half-ellipsoid. This, in turn, gives smaller values for η.

4.2.5. Calibration of z-Radius

The sensitivity study showed the general behavior of the ellipsoid-based model, which is consistent with the experimental observations of the flaw nucleation phenomenon. All the trends are qualitatively as expected; only quantitatively to be calibrated, as discussed in this section.

Temperature, Load and Geometry of Specimens

For calibrating the model to the experiments, we need to setup the boundary conditions to reflect the experiments the best way as possible. The experiments were conducted at room temperature (ca. 25 °C) and at two higher temperatures, T_1 and T_2. During testing the temperatures were kept constant and homogeneous. This is reflected in the simulations by considering constant temperatures of reference for material characteristics, such as Young's modulus in the elastic FEA, stress-strain curves for the shake-down and strain-life relations for the probability of crack initiation.

The flaws are cyclically loaded with $R = \frac{\sigma_{min}}{\sigma_{max}} = 0.1$. Depending on where the specimen exactly failed, the local, uni-axial stress at the fracture surface may slightly vary. The stress fields are homogeneous for the cylindrical tension tests (see Figure 3.7c) and have a gradient for the 4-point bending tests (see Figure 3.8b). These boundary conditions are modeled in the FEA by applying a surface pressure on the top of the cube in two load steps, one with σ_{max} (for T_{RT} this is normally close to 800 MPa) and one with $\sigma_{min} = 0.1 \cdot \sigma_{max}$. The difference between the two resulting strain fields gives the local strain range, which is used for the LCF computation. The bottom of the cube is constrained in load direction.

The size and location of the ellipsoid within the matrix cube are given by radii r_x and r_y (see Figure 4.6) and the distances of the flaw to the specimen's surface. These measures are unique to each sample and replicated in specific FEMs. Only the z-radius, r_z, of the ellipsoid is not defined. We define the curvature, or r_z-ratio, as $\frac{r_z}{A_{cs}}$ where A_{cs} is the cross-sectional area of the ellipsoid in the xy-plane as obtained from r_x and r_y. For each sample, 10 FEM models are produced where the r_z-ratio is incrementally increased from sharp curvatures ($\frac{r_z}{A_{cs}} = 0.1$) to unsharp curvatures ($\frac{r_z}{A_{cs}} = 4.0$). The output of the nucleation model for each r_z variation is compared to the real observed nucleation time from the experiment. With this procedure the model is calibrated.

Maximum log-likelihood Estimation

The experimental results are used for calibrating the nucleation model, such that this model is able to conservatively predict the nucleation time of flaws. First the flaws are separated by type. The most likely r_z is found using the maximum log-likelihood estimation

$$\hat{l}(\theta \mid x_1, \ldots, x_n) = \sum_{i=1}^{n} \ln(f_i(x_i; \theta)) \tag{4.7}$$

By maximizing $\hat{l}$, the most likely θ is found, conditional to observing $x_1, \ldots, x_n$. Within our modeling environment θ represents the r_z-ratio. x_i is the observed amount of nucleation cycles for a specific flaw i which has a measured r_x and r_y and applied σ_{max} and T. $f(x_i; \theta)$ depicts the occurrence probability for realization x_i given a parametric distribution with θ — in our approach this is a Weibull distribution. $f_i(x_i; \theta)$ represents the entire nucleation model including load, temperature, size and geometry of a flaw in specimen i.

With a decreasing θ the curvature sharpness at the equator line of the flaw increases. This causes a steep increase in hazard density, as the purple line in Figure 4.10 already

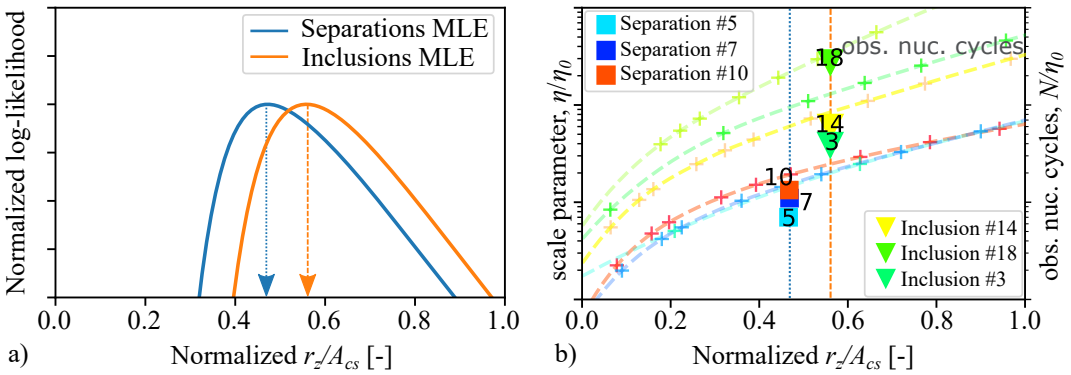

Figure 4.13.: (a) Log-likelihood density curves for varying r_z-ratio for two types of flaws. Calibration is based on experimental data. (b) Calculated Weibull scale parameter for varying r_z-ratio of 6 different flaws. Each indication corresponds to different r_x and r_y values as obtained from fracture surface analysis. The experimentally observed nucleation cycles can be related to the calculated scale parameter η at the intercept with the maximum likelihood estimator for r_z-ratio from figure (a).

showed.

Figure 4.13a shows some results where the log-likelihood for separations and inclusions are compared. For separations the most likely r_z-ratio is smaller than for inclusions. This is expected, as separations appear to have sharper edges and less matrix material cohesion; in the experiments they tend to exhibit a lower number of cycles to nucleation. In the next section the log-likelihood functions have been computed for separation type of flaws and inclusions separately, obtaining tailored calibrations of the r_z-ratio.

Calibration

In Figure 4.13b the simulation results for three examples of separation flaws are plotted. Each flaw, represented by a separate color, has been simulated for several $\frac{r_z}{A_{cs}}$ values and is plotted with the '+'-marks. Then, a trend line has been drawn through those points using a quadratic spline function. The difference between the lines is given by the difference in geometry, temperature and loading conditions between the flaws. For all lines it holds that with increasing r_z the scale parameter η (and with it the cycles to nucleation) increases — same trend as for the purple line in Figure 4.10. For all available samples the likelihood function of Eq. (4.7) is computed and plotted in Figure 4.13a, using the observed amount of nucleation cycles for each flaw. The maximum likelihood estimator for the separations is found and also plotted in the figures (blue, vertical, dotted line). The squares mark the observed number of nucle-

ation cycles for the three examples. These values can be correlated to the calculated scale parameter given by the intersection of the MLE-line with the calculated scale parameter curves for each flaw.

Remember that the separation type of flaws have only been observed at the outer surface of the pancake shaped disk, which will be further machined. This means that the shown results are interesting for the development of the nucleation model, but irrelevant for its application in design. In the following, these flaws will be excluded from the model calibration data set.

For three examples of inclusion type flaws the simulation results for the scale parameters are also shown in Figure 4.13b. The corresponding likelihood densities are plotted in Figure 4.13a. The estimated r_z-ratio tends to be larger than for the separations.

4.2.6. Validation of MLE

After calibration it is important to make a consistency check, which examines the assumption of modeling the nucleation process with a LCF-approach, probabilistically expressed with a Weibull distribution. If the physical process is Weibull distributed, then also the observations should be Weibull distributed after calibration of the model. This test is not trivial for the present problem. Every flaw is modeled by a different Weibull distribution, due to the different conditions (geometry, temperature and load). One possibility is to reduce all the distributions to a 'unity' Weibull distribution with scale parameter equal to 1. This would 'visually' collapse all the flaw models to one identical Weibull distribution with $shape = m$ and $scale = 1$. In order to do so, the observed nucleation durations N_i, for each flaw, are divided by the respective scale parameters η_i. Figure 4.14a shows a plot of the unity Weibull distribution. This distribution is compared with the Empirical Cumulative Distribution Function (ECDF) of the scaled simulations of the experimental observations, $\frac{N_i}{\eta_i}$. As already anticipated by the plot, there is no match with the Weibull distribution.

When dividing all the observations into subsets — grouped by testing temperature, flaw type or even flaw orientation within the crack surface — the results fitted the Weibull distribution only slightly better. The best approximation was obtained by taking the subset of only flaws of the 'mixed oxide' typology, tested at ambient temperature, with orientation parallel to the fracture surface (which is the worst case orientation). This subset consists of 24 flaws which are the ones displayed in the plot of Figure 4.14a. All the simulations were run applying a shape parameter $m \approx 7$ as defined in Section 3.4.1. Several other shape parameters were studied. Figure 4.14b shows results for simulations with, $m \approx 3$. Changing the shape parameter implies that the entire post processing using the local probabilistic LCF approach must be

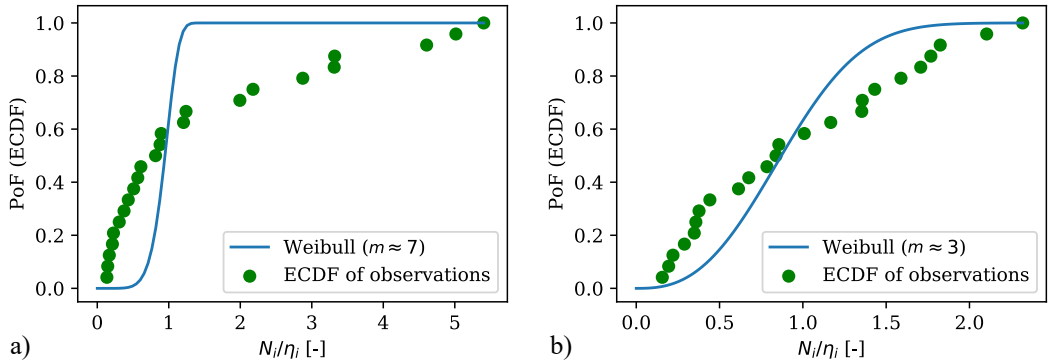

Figure 4.14.: Normalized nucleation times from a subset of experimental observations, N_i/η_i, compared with unity Weibull distributions. (a) Weibull distribution ($m \approx 7$). (b) Weibull distribution ($m \approx 3$).

repeated. The results seem to come closer to the Weibull distribution, but not close enough. Figure 4.15 shows a more detailed overview of the (non-scaled) observed nucleation times plotted against the expected simulated nucleation times. Besides the median values at 50%, there are also several other percentile lines following the Weibull model with $m \approx 3$. The model is calibrated using only the subset of 24 flaws tested at room temperature. But also the flaws tested at T_1 and T_2 are displayed in red and orange. Especially the three T_2 points fall in the conservative part of the plot, upper-left corner. But there are also relatively many T_{RT} points right of the 95% line; this is an indication for a non-conservative prediction.

This poor achievement brought us to increase the complexity of the MLE one step further and to assume θ not to be fixed, but distributed according to a two-parameter density distribution $g_\theta(\alpha, \beta)$. The MLE is not looking for an optimal value of θ anymore, but for optimal values of α and β defining the distribution of θ. Since values of θ are only valid in the positive half-space, we looked at lognormal-, gamma-, Weibull- and uniform- distributions. The best approximations came from uniform and Weibull distributed realizations of θ. The plots in Figure 4.16 show the 'unity' Weibull distribution with $m \approx 3$ compared with families of ECDF scatters where the normalized nucleation time, N_i/η_i, was obtained from random samples of θ according to the uniform distribution (left) and a Weibull distribution (right). 100 MC simulations were performed of which the 5%, the 50% and 95% percentiles are displayed. The results from the Weibull distributed θ look slightly better, but also here it holds that the mean values fit quite well, but the overall shape of the ECDF is far off.

If we were to apply this nucleation model with the current calibration, the most worrying matter would be conservatism. In principle we can state that if the ECDF

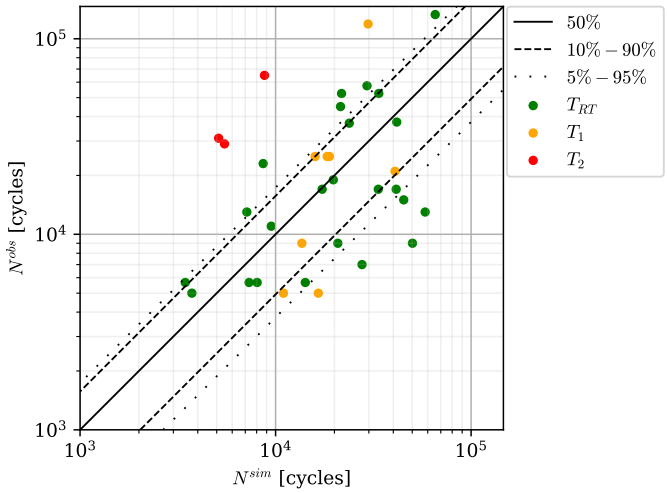

Figure 4.15.: Observed nucleation times vs. the simulated expected nucleation for the ellipsoid model with $m \approx 3$ with distinction in temperature and percentile bands.

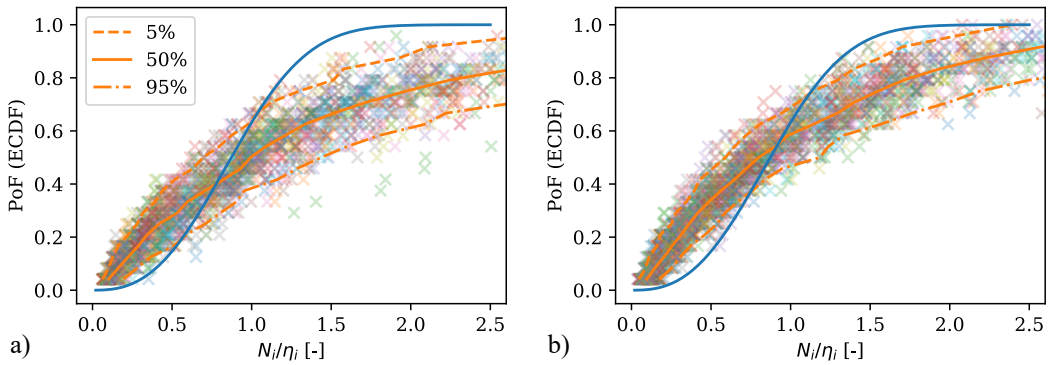

Figure 4.16.: Normalized nucleation times from a subset of experimental observations compared with unity Weibull distributions ($m \approx 3$). The ECDFs of N_i/η_i are obtained from 100 MC simulations. (a) Values for θ sampled from a uniform distribution. (b) Values for θ sampled from a Weibull distribution.

of normalized, nucleation times lies (partially) left of the unity Weibull distribution (blue line in Figures 4.14 and 4.16)), the approach is not conservative. In other words it means that it is very likely that the model predicts shorter nucleation times than observed from experiments. On average the predicted nucleation times will be fine, but in the tails it is not representative. From the presented plots we can conclude that the current calibrated model is not conservative and not applicable.

4.2.7. Discussion

From the presented results it seems that modeling the flaws with effective ellipsoids led to unsatisfactory results. The calibration of the curvature parameter $\frac{r_z}{A_{cs}}$ increased complexity and gave no good results when comparing the predicted nucleation times of the model with the observed nucleation times of the experiments. The Weibull hypotheses could not be proven right. Modeling flaws with a 3D geometry seemed to make sense, as we imagined the nucleation process to take especially place at the border of the flaws where the sharp crack initiates. The beauty of that approach is that by means of a local probabilistic LCF computation the equatorial region of the ellipsoid became the exclusive area where a crack would initiate. When applying an elastic stress as membrane stress on the ellipsoid, the local notch would increase this elastic stress into the plastic region, with lower life expectation. The plot in Figure 4.17 shows the simulation results for a representative flaw at room temperature for varying applied load σ_{max}. The nucleation life (expressed in a normalized scale parameter η) is computed using $m \approx 3$, see Figure 4.14b. From Figure 4.17 we see that for low loads ($\sigma_{max} < 400$ MPa), the life expectation steeply increases up to extremely high orders of magnitude (10^9 cycles), following the elastic part of CMB equation. Here the equatorial area is still completely in the elastic regime. Around ca. 400 MPa the steepness decreases and plasticity starts playing a predominant role. The equatorial area is in highly plastic regime even if the applied load σ_{max} is not. The dashed line shows a reference η_0 of 1000 cycles at 800 MPa, similar to most T_{RT} experiments. This is the parameter domain to which the model was calibrated. The plot shows that the experiments were acting in a fully plastic regime at the equator. The sketch in Figure 4.18a illustrates how the contribution of the equatorial region is overwhelmingly larger than the remaining surface of the ellipsoid.

This equatorial area is directly related to the circumference of the ellipse (defined by r_x and r_y) and takes the size effect of the flaw into account. The circumference of an

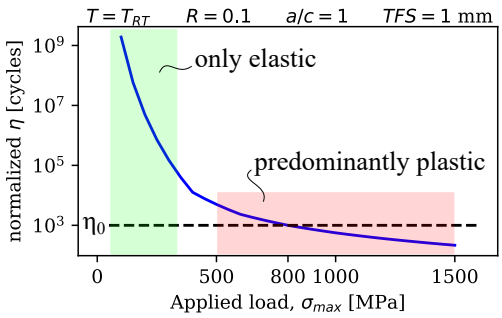

Figure 4.17.: The plot shows the predicted nucleation life expressed in η (normalized) for varying applied load σ_{max}. The dashed line shows a reference $\eta = 1000$ cycles for an applied load of $\sigma_{max} = 800$ MPa, which is comparable to most T_{RT} experiments.

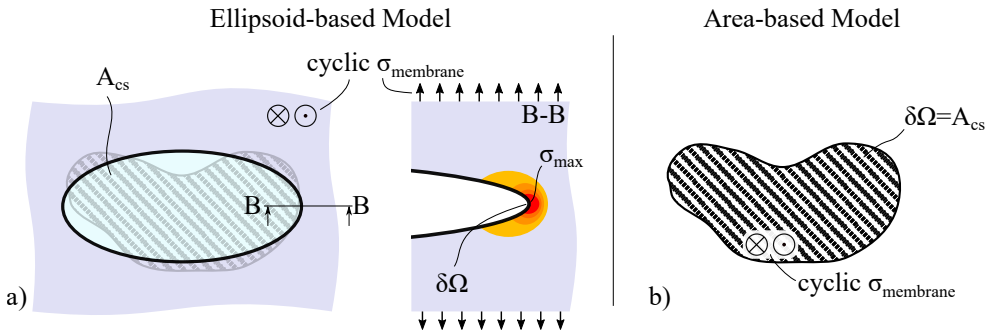

Figure 4.18.: (a) The ellipsoid-based modeling approach has a hot-spot region on the equator line with significant plastification (even at low membrane stresses). This region is effectively the surface area, $\partial\Omega$. (b) The area-based model has no hot-spot region, since the entire equivalent area $\partial\Omega$ is loaded equally with the membrane stress.

ellipse can be approximated using Ramanujan's so called 'second approximation' [72]:

$$p_{ellipse} = \pi(r_x + r_y)\left(1 + \frac{3h}{10 + \sqrt{4 - 3h}}\right)$$
$$h = \left(\frac{r_x - r_y}{r_x + r_y}\right)^2 \tag{4.8}$$

By this equation it becomes clear that the effectively loaded area $\partial\Omega$ of the ellipsoid is a functional of $(r_x + r_y)$.

In the next section an alternative modeling approach is presented, which is more focused on the area of the flaw visible on the fracture surface. This area was previously coined as cross sectional area, A_{cs}, and is functional of $(r_x \cdot r_y)$. In this approach the area $\partial\Omega$ $(= A_{cs})$ is loaded with the membrane stress (Figure 4.18b); the same

stress that was previously used as boundary condition on top of the cube, see Figure 4.7. This alternative approach is far less complex and the calibration results look astonishingly good. The physical meaning behind modeling the flaw according to its cross-sectional area only — rather than by a 3D ellipsoidal geometry — is that the nucleation process is stochastically taking place within the entire flaw and not only at the outer border, where the long crack eventually propagates. The bulk of the flaw consists of more or less densely packed particles mixed with ligament from the matrix material. The nucleation process seems to be decided in the microstructural process of coalescence of those particles and the progressive collapse of the ligament.

For a fundamental understanding of the underlying physical mechanisms leading to crack formation one could use microscale models. They are often computationally expensive and require many detailed information about the flaws which limit their application to the experimental academic domain. They are not conceived as models for application in engineering tools for components, but their findings can still help to deduce macroscale behavior of materials. Together with the Los Alamos National Laboratories and funded by the US Department of Energy, Siemens Energy ran a simulation program where the experimental results from the present study were compared against peridynamic simulations using high performance computing techniques. Publications by Karim et al. [74; 75] show the progressive process of coalescence of particles. Figure 4.19 illustrates a 2D peridynamic simulation where a flaw is modeled as a cloud of single particles (red) trapped in a 2D cross-section of matrix material (blue). The model is cyclically loaded in vertical direction, causing damage to the internal structure of the flaw (white-red). The nucleation process in this simulation is initially taking place internally to the flaw. This is a rather stochastic process. The exact location of the worst damaged areas depends on the random configuration of the single particles. This means that, beside the statistical aspect of the damage process, there is also a statistical geometry aspect. The same kind of simulations are also run in a 3D model. Similar results were obtained, but the 3D coalescing process is more difficult to visualize. Interesting thing to learn from those simulations is that the nucleation process is more related to the internal structure of the flaw, and thus to an area dependent parameter, than to the ellipse shape of the flaw, which is the typical shape used in FM computations for sharp (already nucleated) cracks.

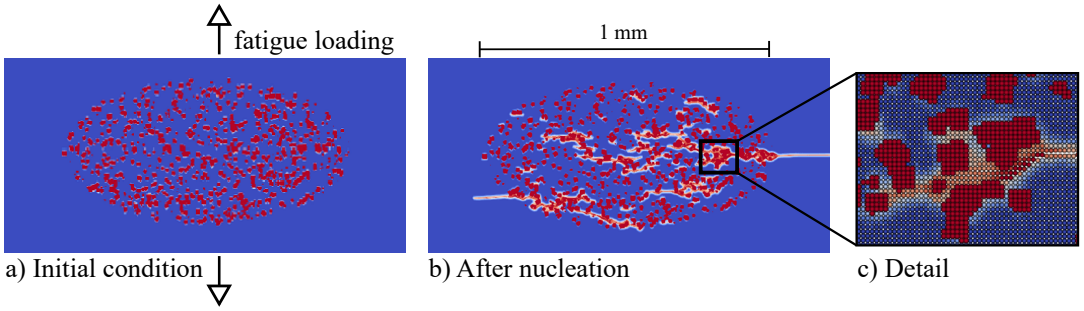

Figure 4.19.: (a) 2D peridynamic simulation of an embedded flaw under cyclic loading. Blue is the matrix material and red the NMI. (b) The single particles coalesce and develop a crack. The matrix material damages in a scale ranging from 0–1 (blue-white-red). (c) Detail of coalescing particles and ligament collapse. From [74].

4.3. Area Based Nucleation Model

4.3.1. Probabilistic Nucleation of Effective Surface

Instead of modeling the flaw as a 3D geometry with unknown third dimension r_z, it can be modeled as a smooth 2D area by only considering the measurable cross sectional area of the flaw, A_{cs}. A flat element with an area A_{cs} is loaded with σ_{max} and σ_{min} at given temperature. Two calibration options have been explored, both adjusting the results on the stress-life plane. The first one uses a correction factor w, that is applied on the simulated nucleation cycles (expressed by η^{sim}) in order to fit the experimental results (expressed by η^{exp}). The second one uses a stress concentration factor K_t, applied to the membrane stress, $\sigma_{membrane}$. K_t is calibrated such that the simulations fit best the experiments. Figure 4.20 shows the stress-life plane — similar to Figure 3.20 — that visualizes the two correction factors in a plot which is further detailed in the next sections: w causes a horizontal shift and K_t a vertical one.

4.3.2. Motivation for Area-Based Model

A quick preliminary check can be performed on the suspect that the nucleation time is Weibull distributed and mainly related to A_{cs}. By using the subset of flaws with similar temperature and loading condition, we can 'turn off' those influencing parameters and focus on the area only. With Eq. (4.6) we can convert $\eta_i(A_{cs,i})$, valid for flaw i, to $\eta_{i,1\text{mm}^2}(A_{1\text{mm}^2})$, valid for a $1\,\text{mm}^2$ equivalent flaw. This way the area is accounted for and the observations are collapsed in a load, temperature and area independent space. A well defined η_i should be correlated to the observed nucleation time for that particular flaw, N_i. For the sake of a preliminary check, we can substitute η_i by N_i

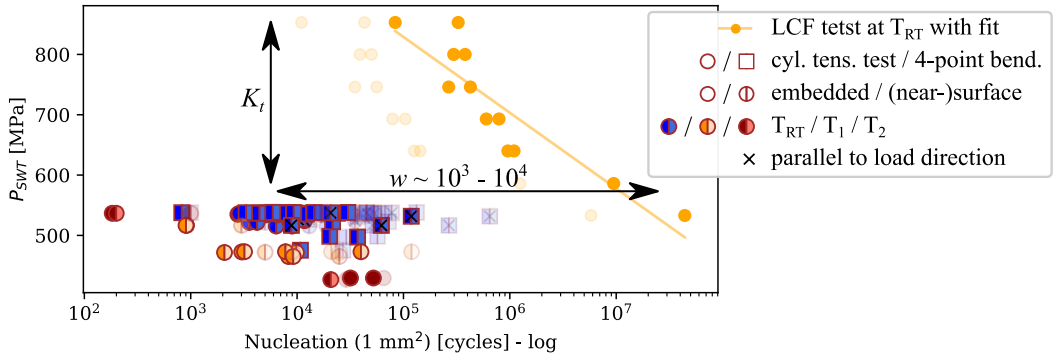

Figure 4.20.: Comparison of clean LCF specimens towards the nucleation lives of flaws after applying a 1 mm^2 equivalent size correction. The transparent data points are the uncorrected ones taken from Figure 3.20. Calibration of w causes an horizontal shift; while calibration of K_t causes a vertical shift.

and simplify Eq. (4.6):

$$N_{i,1\text{mm}^2} = N_i \left(\frac{A_{cs,i}}{1[\text{mm}^2]} \right)^{\frac{1}{m}} \tag{4.9}$$

Doing so for the selected flaws results in the ECDF of $N_{i,1\text{mm}^2}$ shown in Figure 4.21. In the same figure also the ECDF of the original, unscaled N_i's are plotted, visualizing the effect of scaling to 1 mm^2 equivalent flaws. In an iterative process the Weibull curve is fitted to the results and the area correction is re-performed with the optimized shape parameter, m. After a sufficient amount of iterations a converged value for m is found. The plot in Figure 4.21 shows that the corrected nucleation times fit a Weibull distribution astonishingly good. The obtained shape parameter, $m = 2.92$, is very close to the one assumed for the ellipsoid-based model of Section 4.2.6, see Figure 4.14b.

Despite not having many flaws available at testing temperatures T_1 and T_2, we repeated the above scaling exercise for 8 flaws at T_1 and 3 at T_2, where loads of respectively ca. 700 MPa and ca. 640 MPa were aplied. The plots of Figures 4.22a and b are obtained. Even though the ECDFs are sparsely populated, the two plots seem to comply with the Weibull assumption. Note that the Weibull shape at T_1 is smaller than 2. Weibull distributions with $m = 2$, are Rayleigh distributions. If the shape parameter is smaller than 2, the distribution rises to a peak quickly, with the maximum increase in failure rate occurring at the first cycle. Such shapes are used to model early wear-out. Also note that for T_2 the amount of cycles tend to be much larger than at the other temperatures.

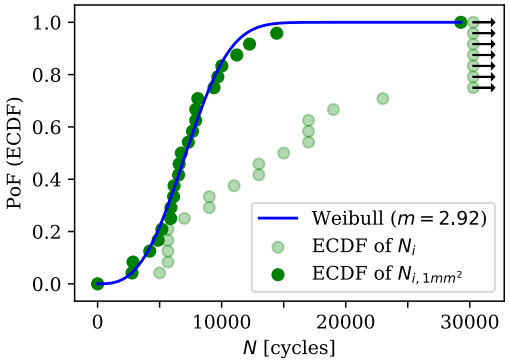

Figure 4.21.: ECDF of nucleation times as observed for selected flaws (for some flaws the nucleation times were very high and did not fit the plot). Corrected nucleation time for $1\,\mathrm{mm}^2$ equivalent flaws and corresponding Weibull fit. Only mixed oxide type of flaws, tested at T_{RT}, oriented parallel to fracture surface are considered.

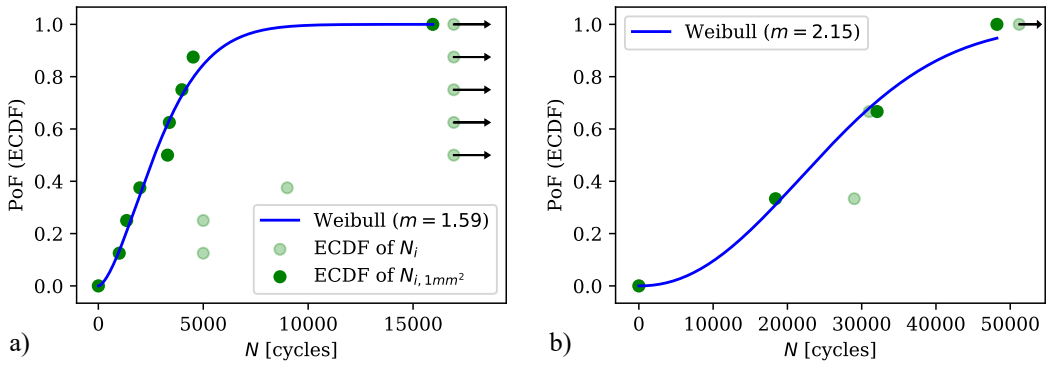

Figure 4.22.: ECDF of nucleation times as observed for selected flaws. Corrected nucleation time for $1\,\mathrm{mm}^2$ equivalent flaws and corresponding Weibull fit. (a) Flaws tested at T_1. (b) Flaws tested at T_2.

4.3.3. Calibration of Life Correction Factor

For a $1\,\mathrm{mm}^2$ equivalent flaw we fitted a Weibull function for the experiments at room temperature (see Figure 4.21) with shape parameter $m = 2.92$ and a scale parameter which we call $\eta_{RT}^{exp}(1\mathrm{mm}^2)$. The underlying data points were tested with a maximum load of 800 MPa and $R = 0.1$ at 20 °C. By applying these same conditions on a $1\,\mathrm{mm}^2$ flat surface, the local probabilistic LCF model gives a scale parameter, $\eta_{RT}^{sim}(1\mathrm{mm}^2)$. To obtain results similar to the experiments, we define a calibration factor, w:

$$w = \frac{\eta^{sim}(1\mathrm{mm}^2)}{\eta^{exp}(1\mathrm{mm}^2)} \tag{4.10}$$

This factor can be physically understood if we compare the LCF life expectation of a clean specimen of $1\,\mathrm{mm}^2$ to the life of a $1\,\mathrm{mm}^2$-equivalent flaw. The LCF curve was already plotted against the flaw nucleation life in Figure 3.20. Figure 4.20 shows basically the same information, but with all cycles converted to a $1\,\mathrm{mm}^2$ equivalent, using Eq. (4.9). The gauge area of the clean LCF specimens was ca. $373\,\mathrm{mm}^2$. With $m = 2.92$ the LCF life of $1\,\mathrm{mm}^2$ equivalent specimens shifts to much longer lives due to the size effect. This shift is illustrated by the transparent yellow dots moving towards the plain yellow dots. The yellow line is a linear least squares trend line. Also the data points of the experiments with flaws move slightly after correcting them to $1\,\mathrm{mm}^2$ equivalent flaws. If we roughly compare the LCF life of the trend-line with the nucleation life of the experiments (at similar values of P_{SWT}), we find a factor of about 3 to 4 decades (as illustrated with the horizontal arrow). Similar factors are found for w at T_{RT}, T_1 and T_2. The difference in LCF life basically corrects for the weakened material due to the presence of the NMI, where the matrix material is interrupted by flaw particles. The high scatter might be due to the fact that not only the uncertainty of the LCF life, but also the scatter in geometrical features of the flaws, are contained in the Weibull scatter. Variation in particle density, size distribution, bonding to the matrix, distance to the surface and overall constellation between the flaws seems to be captured well in the Weibull system. With the consequence that m decreases from $m \approx 7$ for the purely LCF based calibration to $m < 3$ for the experiments with defects.

Now, all the flaws can be simulated with respective areas A_i, applied load σ_{max} and temperature T. The obtained scale parameter, η_i^{sim} is corrected with factor w:

$$\eta_i = \frac{\eta_i^{sim}(A_i)}{w} \tag{4.11}$$

Just as previously done with the ellipsoid-based model validation, we can divide the experimentally observed nucleation life N_i, by the calibrated scale parameter

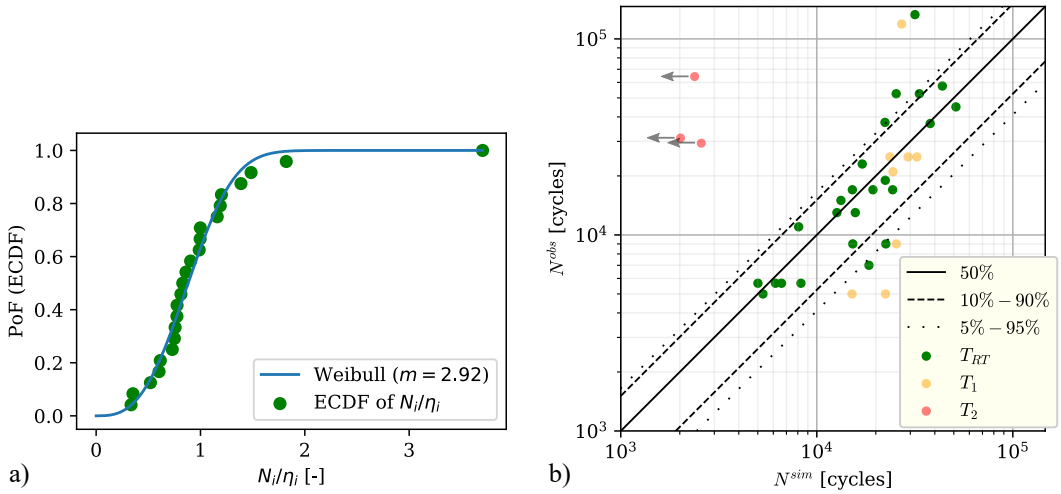

Figure 4.23.: Area-based nucleation model with w calibrated to only mixed oxide type of flaws, tested at T_{RT}, oriented parallel to the fracture surface. (a) Normalized nucleation times for experimental observations at T_{RT}, N_i/η_i, compared with unity Weibull distribution. (b) Observed nucleation times vs. the simulated expected nucleation with distinction in temperature and percentile bands ($m = 2.92$).

obtained from the simulation η_i, and validate the behavior of the model. Figure 4.23a shows the ECDF of N_i/η_i plotted against the Weibull distribution with $\eta = 1$ and $m = 2.92$. The plot looks pretty much identical to the experimental results shown in Figure 4.21, only with a normalized scale parameter. This proves that the model calibration works properly and that the selected flaws indeed can be modeled with an area-based probabilistic LCF model defined by a Weibull distributed scatter.

Figure 4.23b shows the observed nucleation times vs. the median of the simulated nucleation times. w has been calibrated to T_{RT} flaws and applied also to the other temperatures T_1 and T_2 for comparison only. The T_{RT} points seem, indeed, to be predicted well. The T_1 flaws have relatively many (3/8) points below the 5^{th} percentile, which is non-conservative. The three T_2 flaws, on the contrary, fall outside the plot in an overly conservative domain. In an ideal case, the data points for the three temperatures would all lie along the median line. This would confirm that the temperature dependent LCF model captures the temperature variations well. Unfortunately, the plot shows that — especially for T_2 — this is not the case.

Repeating the calibration for temperature T_1 with $m = 1.59$ returns a new calibration factor w. The ECDFs of N_i/η_i for the subset of flaws tested at T_1 is plotted in Figure 4.24a. It shows that the calibration works properly also for the flaws at T_1. Figure 4.24b shows, again, the comparison between the observed and the simulated

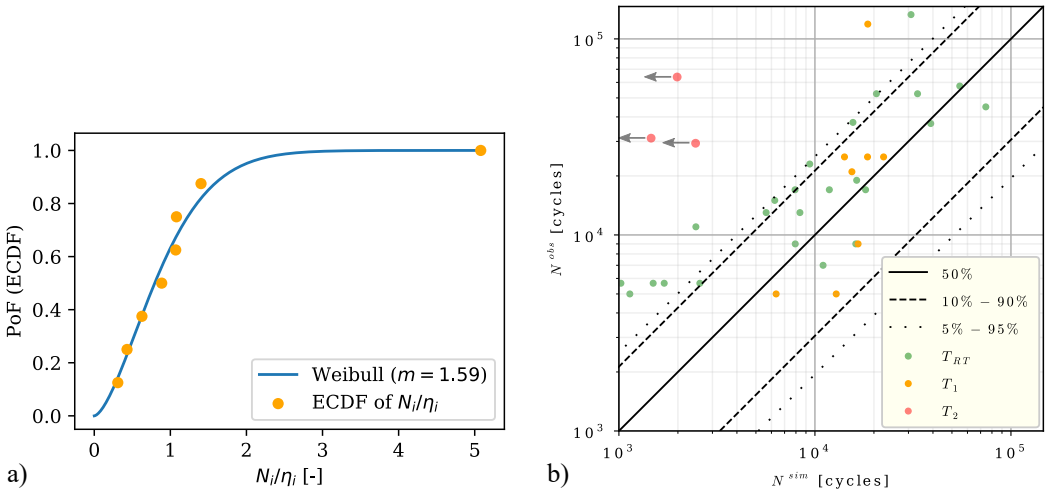

Figure 4.24.: Area-based nucleation model with w calibrated to T_1. (a) Normalized nucleation times for experimental observations at T_1, N_i/η_i, compared with unity Weibull distribution. (b) Observed nucleation times vs. the simulated expected nucleation with distinction in temperature and percentile bands ($m = 1.59$).

nucleation times for this model. Since the shape parameter is smaller, the percentile bands are wider. Also here, the points at T_2 fall outside the plot area and are estimated overly conservative. One main concern to this model is that $m < 2$, which is untypical for the pure LCF behavior of the regarded steel.

A calibration based only the three T_2 flaws does not make sense. Since for T_{RT} we had the largest calibration base and $m > 2$, we will consider that model for further analyses. The behavior of this model for varying loading conditions is shown in Figure 4.25, where the correlation of the expected nucleation life (expressed in a normalized scale parameter η) and the applied load σ_{max} is plotted. For comparison also the result of the ellipsoid-based model from Figure 4.17 is plotted. The area-based model is directly proportional to the CMB curve: when doubling the load, e.g. from 500 to 1000 MPa, the life decreases by 4 decades, similar to the LCF curve for this material at room temperature, Figure 3.5b. This is much steeper than for the ellipsoid-based model, because there are no local plastification effects playing a key role. Consequence is that for higher loads, the life decreases fast. Also here the dashed line can be used as reference for comparing the two models that were both calibrated for loads around 800 MPa.

The main problem with the area-based model with correction factor w is that it behaves overly conservative for the T_2 observations. At such high temperatures I suspect that the ligament between the NMI particles behaves more ductile and

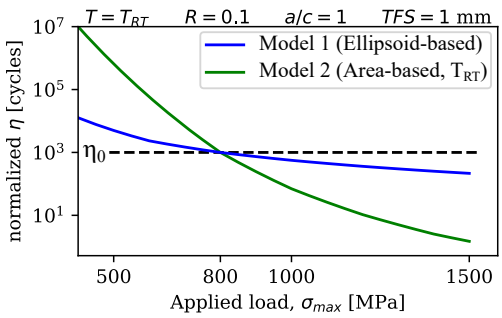

Figure 4.25.: The plot shows the predicted nucleation life expressed in η (normalized) for varying applied load σ_{max}. The dashed line shows a reference $\eta = 1000$ cycles for an applied load of $\sigma_{max} = 800$ MPa, which is comparable with most T_{RT} experiments.

microcrack formation takes longer. This might explain the longer observed nucleation times for the three T_2 flaws. Instead of picking only one calibrated w, we could consider a varying, temperature dependent $w(T)$. This however would increase complexity, it would be prone to over fitting and introduce the problem of how to interpolate between the three calibrated temperatures T_{RT}, T_1 and T_2. In the next section we introduce another area-based model where the temperature dependence gives more satisfying results.

4.3.4. Calibration of Stress Concentration Factor

The previously presented area-based model with correction factor w is not accounting for plasticity effects like the ellipsoid model did. The ellipsoid-based model had an inherent stress concentration at the equatorial region. We can add this plasticity effect artificially on the area-based model by multiplying the applied membrane stress with a stress concentration factor K_t:

$$\sigma_{max} = \sigma_{membrane} \cdot K_t \tag{4.12}$$

In this case the conversion factor w is not applied. This approach may be represented as a vertical shift in stress direction, see Figure 4.20, rather than an horizontal shift in life direction, as was the case with w. An optimal K_t is found using a MLE method, see Eq. (4.7). The variable θ in this case equals K_t. At each variation of K_t, the area-based model is simulated for each flaw i, resulting in n Weibull functions $f_i(x_i;\theta)$. Using the so-called 'golden section search' algorithm [41], a maximum $\hat{l}$ is found with $K_t = 3.2$, calibrated with the 24 flaws at T_{RT}. This value for K_t seems a very reasonable stress concentration factor for a stress field with the presence of an

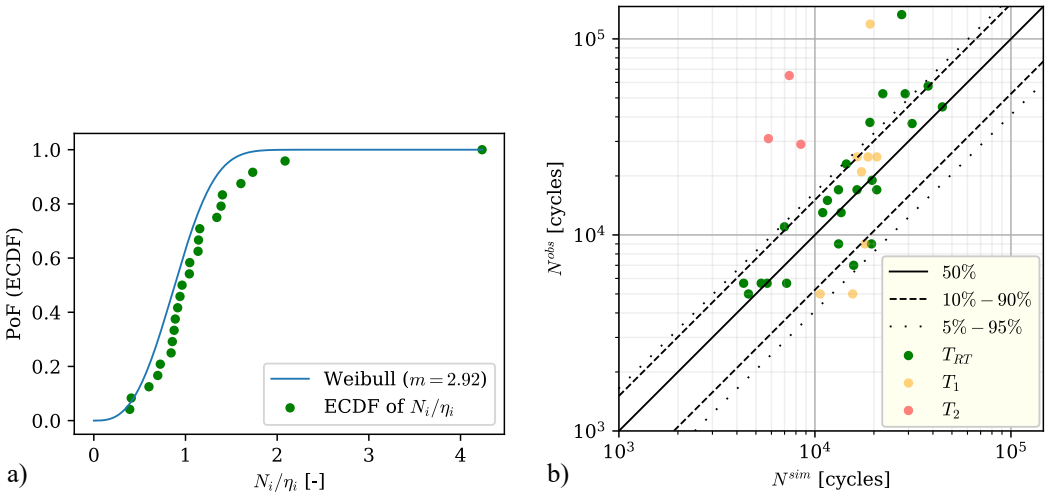

Figure 4.26.: Area-based nucleation model with K_t calibrated to only mixed oxide type of flaws, tested at T_{RT}, oriented parallel to the fracture surface. (a) Normalized nucleation times for experimental observations at T_{RT}, N_i/η_i, compared with unity Weibull distribution. (b) Observed nucleation times vs. the simulated expected nucleation with distinction in temperature and percentile bands ($m = 2.92$).

inclusion. Figure 4.26a shows the ECDF of N_i/η_i plotted against the unity Weibull distribution with $m = 2.92$. Figure 4.26b shows the comparison of the absolute observed nucleation times vs. the medians of the simulated nucleation times. The flaws at T_{RT} fit well, some points at T_1 seem non-conservative and the three flaws at T_2 are not overly conservative anymore. With this modeling approach we obtained the best results.

4.4. Comparison of the Different Modeling Approaches

In the previous sections I presented three modeling approaches:

- Ellipsoid-based modeling approach (Model 1),
- Area-based modeling approach with correction factor w (Model 2),
- Area-based modeling approach with stress concentration factor K_t (Model 3)

All three models are calibrated using the subset of 24 flaws tested at T_{RT}. Figure 4.27 shows the detailed overview of the (non-scaled) observed nucleation times plotted against the expected simulated nucleation times for the three models as already shown in the previous sections.

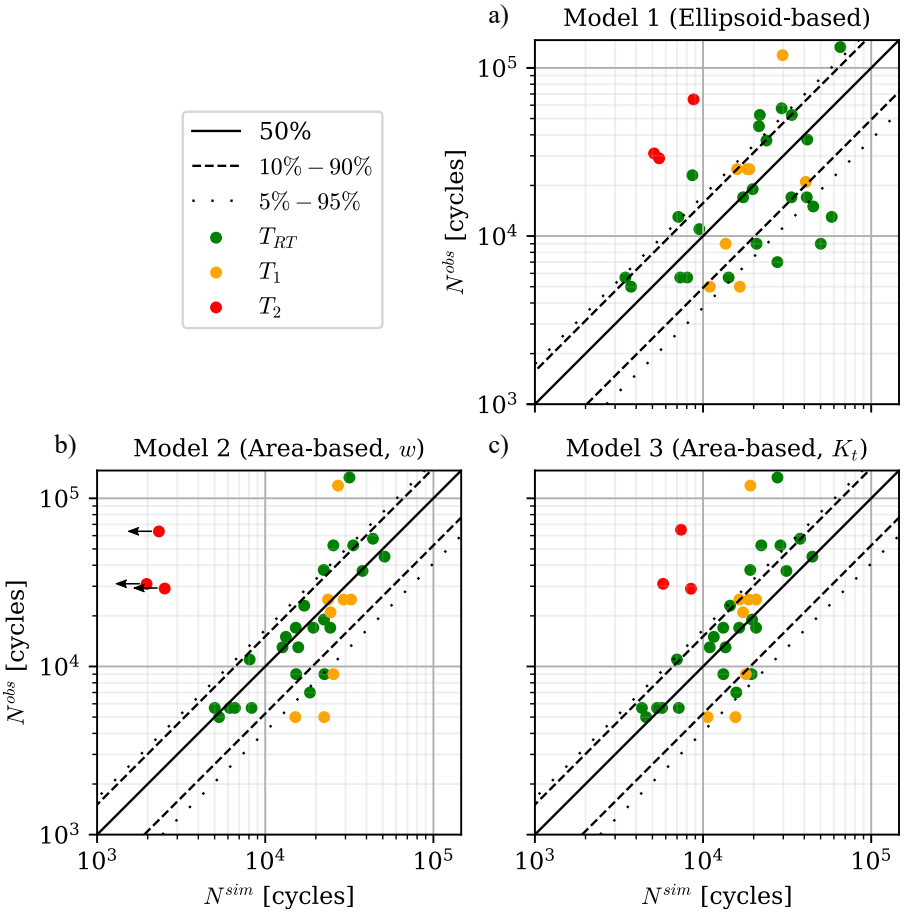

Figure 4.27.: Comparison of the results for three modeling approaches. Observed nucleation times vs. the simulated expected nucleation for the single models with distinction in temperature and percentile bands.

Model 1 has no extremely conservative points, but has an overall bad match with the Weibull distribution. Model 2 makes a good fit to the Weibull distribution, but it also has some overly conservative predictions, especially for the three flaws at T_2. Model 3 follows the Weibull curve well and has conservative predictions without being overly conservative at T_2.

4.5. Discussion

The area-based model with calibration factor w proved that the Weibull approximation for crack initiation, based on the area of the flaw — rather than modeling the flaw as an ellipsoid — fits the experiments well. One drawback of this approach is

σ_{max} [MPa]	$R = \frac{\sigma_{min}}{\sigma_{max}}$ [-]	Temperature [°C]	Area (πac) [mm^2]	η scale-parameter
200	-0.2	RT	0.5	12345
...	...	...	...	...
1500	1	500	5	67890

Table 4.2.: Outlook of a lookup table resuming the resulting η's for all the combinations of input parameters covering the design space.

that it does not account for local plasticity effects at the crack formation front, since it has an identical load definition over the entire area equal to the membrane stress of the matrix material. The ellipsoid-based model had a very prominent plasticity effect at the notch (the equator area), which seemed to reproduce well the ductile behavior at high temperatures of crack formation from the NMI particles. In this model the remaining surface of the ellipsoid barely contributes. Unfortunately, there was no good match of the modeled experiments with the Weibull distribution, which suggested that the hazard density, concentrated only at the equator, did not account for the size effect properly. The area-based model has been improved by artificially adding the plasticity effect with a stress concentration factor K_t. Here the entire area of the flaw contributes to the hazard rate. The plastic region is not limited to the border, but it is present on the entire flaw area, taking the best from the two previous modeling approaches.

4.6. Model Implementation in Engineering Tool

In order to continue the reflection and show-case the implementation of the nucleation model in design, I assume the presented area-based model (Model 3) to be final. This model is calibrated to the experiments and predicts the nucleation time of forging flaws with different sizes, varying temperature and loading conditions. With a DOE, the entire parameter space is covered based on a large amount of numerical simulations. This DOE makes the implementation of the nucleation model extremely fast, because there is no need to run numerical simulations within the engineering application itself. The DOE is feeding a large lookup table which serves as regression model for the nucleation life. An outlook of such table is illustrated in Table 4.2. It contains thousands of combinations of input parameters.

The nucleation model only makes sense if embedded in a framework for quantifying the entire life cycle of a flaw. According to Section 4.1 the life cycle of a flaw consists of the nucleation phase and the crack propagation phase. The crack propagation phase has been the focus of many studies and is usually approached by LEFM. I

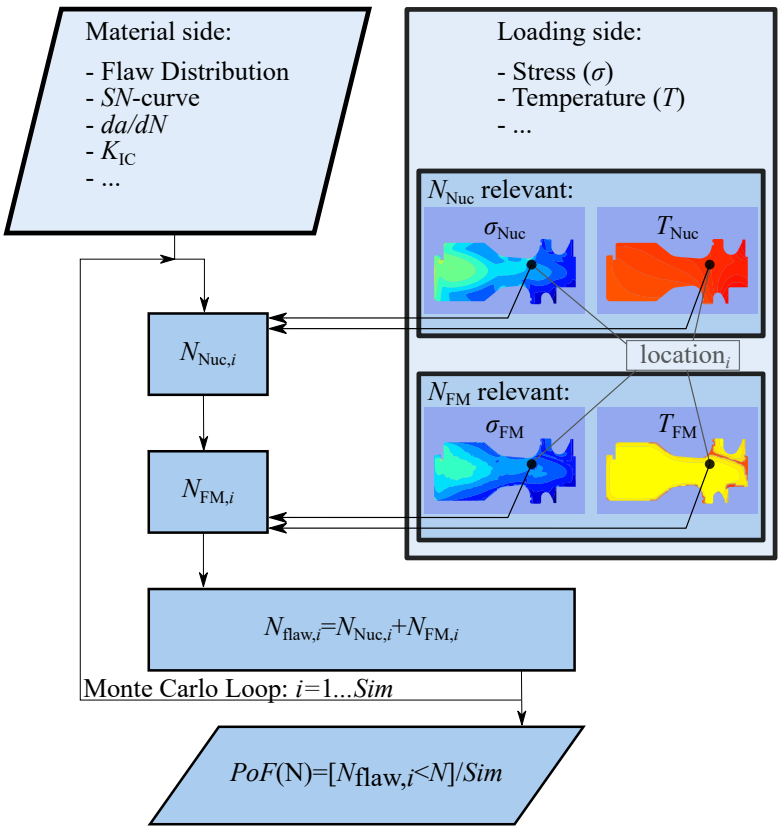

Figure 4.28.: Direct simulation MC approach for probabilistic implementation of the suggested combination of nucleation life and fracture mechanical life.

already referred to the work of Kadau et al. on the probabilistic fracture mechanics framework, *ProbFM*. Here I present the modular addition of the nucleation phase to this framework, which was also presented in [69].

By means of a direct simulation MC loop, a large number of simulations are performed, each with a single flaw realization. The flaws in the component are sampled based on a UT inspection database. The simulation procedure takes into account the PoD of the applied UT inspection procedure (i.e. flaws can be missed), the size and location of the flaws, as well as the conversion from the measured to the true flaw size. Details about the derivation of these flaw distributions are nicely resumed by Vrana et al. [102].

Both the nucleation and the crack propagation life depend on material properties such as SN-curves, $\frac{da}{dN}$-curves, $\frac{\sigma}{\varepsilon}$-relationships, flaw sizes and geometries, expressed by statistical distributions that follow certain assumed distributions. These properties have also relevant statistical correlations, see Annis [8]. However, nucleation and crack

propagation life depend also strongly on the component loading conditions, including transient temperature and stress distributions typically obtained by transient thermal and mechanical FEA. In general, the two processes of crack nucleation and crack propagation do not have the same definitions of critical temperatures and stresses along the load transient. The nucleation process e.g. is accelerated by higher temperatures and larger stress amplitudes. The crack growth might be limited to critical transient time points exposing a low fracture toughness for low temperatures. Also, crack growth might be more dependent on the crack plane and stress orientation. For each process the significant temperature- and stress amplitude fields are obtained, which serve as input for the respective module. These contour plots are visualized in the flowchart of Figure 4.28, where also the direct simulation MC loop is shown. The statistical variables are randomly sampled according to their distributions and correlations. Each simulation consists of a realization of one flaw with its own nucleation life $N_{Nuc,i}$ and subsequent fracture mechanical life $N_{FM,i}$. They are strongly depend on the location$_i$ where the flaw is sampled. Summing the two gives the total lifetime $N_{flaw,i}$. At the bottom of the flowchart the probability of failure after N cycles is calculated by

$$PoF(N) = \frac{S_f(N)}{S} \tag{4.13}$$

where S is the total number of simulated MC samples, and $S_f(N)$ is the number of samples that failed after N cycles. The hazard rate H is defined by:

$$H(N) = \frac{PoF(N+1) - PoF(N)}{1 - PoF(N)} \tag{4.14}$$

H is used as a measure for the risk of failure within the next cycle under the condition that no failure has occurred before. In order to resolve low probabilities of failure for rotating equipment, millions to billions of MC samples have to be performed. Chapter 5 illustrates this procedure based on a component application.

5. Component Applications

In this chapter we present two component applications of the newly developed nucleation model, integrated within the *ProbFM* framework. In a first case we consider a simplified component, and look at some general effects of the nucleation model on the total life time prediction. In the second case a real-life rotor component with more complex geometries and loading conditions is considered.

5.1. Simplified Rotor Component

With a simple geometry it is easier to demonstrate the basic functioning of the nucleation model. The loads and temperature distributions are kept simple and predictable. A rotor disk is often modeled with a 2D axis-symmetrical model, as illustrated in Figure 5.1a. The 2D model is basically one section of the disk drawn with x and y coordinates. The simplified component is based on such an axis-symmetrical model of a cylinder with a hole in it. No additional geometrical features.

5.1.1. Stresses and Temperatures

Mechanical stresses are caused solely by the rotational velocity and are a combination of hoop and radial stresses. These stresses increase as the rotational velocity increases during start-up of the engine.

Also the temperature field changes in time. At start-up the exterior of the disk heats up quickly and heat slowly diffuses to the interior of the cylinder, causing thermal stress overshoots in the bulk of the disk.

From a nucleation point of view, we are interested in finding the minimum and maximum local stresses defining a LCF load cycle and the applicable temperature. Since the highest temperature does not necessarily coincide with the maximum stress in time, it is conservative to apply the maximum temperature to the entire load cycle. The critical stress condition follows from a detailed analysis of the evolution of the stress tensor within the transient. The maximum amplitude in combination with the mean stress are computed for each location. Figures 5.1b and c show the maximum stress amplitudes and the maximum temperature fields within the transient analysis. The thermal stress overshoot in the bulk of the disk is clearly recognizable.

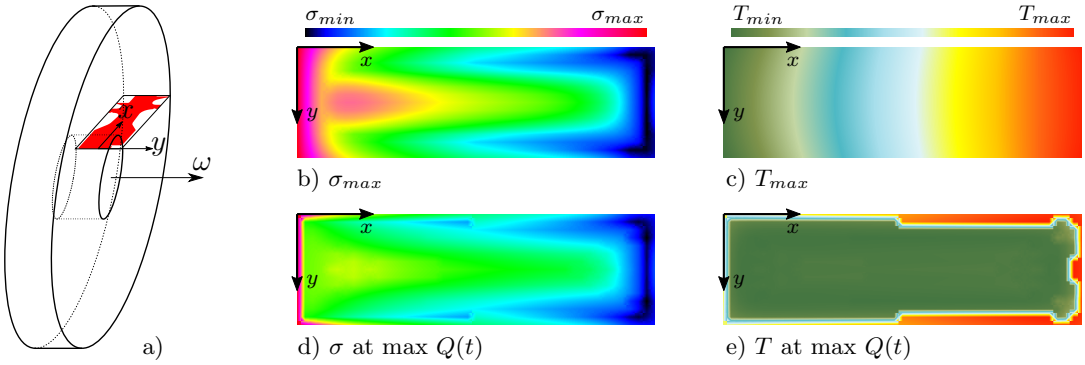

Figure 5.1.: (a) Both the dummy component and the real-life rotor disk are modeled according to a 2D axis-symmetrical representation of a disk. (b)(c) Nucleation relevant load and temperature distribution within the dummy component. (d)(e) FM relevant load and temperature distribution.

From a fracture mechanics point of view, the situation is more complex. Generally speaking, the crack growth rate $\frac{da}{dN}$ increases with higher temperatures; the critical stress and temperature states within the transient, however, are found at the most critical condition for the failure criterion which is stress and toughness driven, see Chapter 3 of Amann [4] for a more thorough explanation:

$$Q(t) = \frac{||\underline{\sigma}(t) \cdot \hat{\sigma}_I^{max}||}{K_{Ic}(T(t))} \tag{5.1}$$

The numerator is large at high stresses, and the denominator is small at low temperatures. This leads sometimes to surprising pictures for the most critical local time steps. Figures 5.1d and e show the critical stress and temperature situations for each location at the load step where $Q(t)$ is maximum.

5.1.2. Discrete Approach

The nucleation model has been inserted within *ProbFM* in a step-wise approach by first considering the worst conditions for crack nucleation within the entire disk and progressively expanding the assessment to local conditions. By applying the worst stress and temperature conditions w.r.t. nucleation and w.r.t. propagation respectively, one obtains a very conservative reliability assessment of the disk. This assessment consisted in performing the MC simulations as described in the flowchart of Figure 4.28; instead of applying local stresses and temperatures, the global, worst conditions in the entire component have been applied for each simulation i. Then, we split the disk in two zones and took for each zone the worst conditions. Proceeding this way up to more than 1000 zones. Figure 5.2 illustrates this procedure of pro-

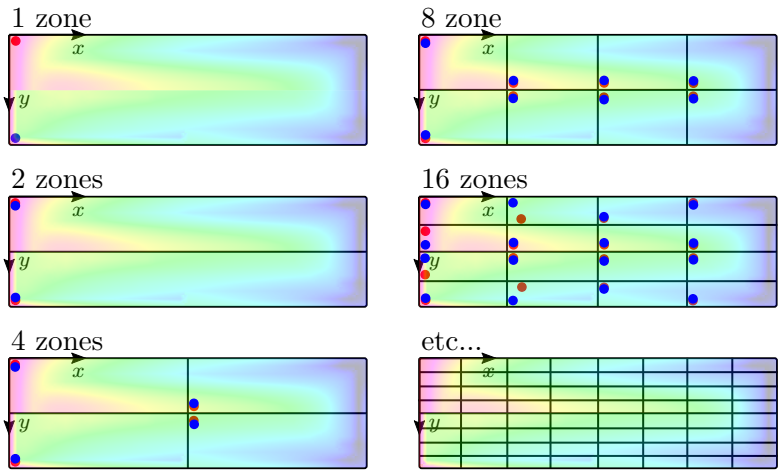

Figure 5.2.: Dummy component with increasing amount of zones, each with worst nucleation (red dot) and worst propagation (blue dot) spot — that do not always coincide. As reference, also the stress fields from Figures 5.1b and d are plotted in the background of the component in transparent colors: the upper half shows σ_{max} (significant for nucleation) and the lower half shows σ at max $Q(t)$ (significant for propagation).

gressive creation of zones with the maximum loading conditions for nucleation and propagation marked by respectively red and blue dots.

Figure 5.3 shows how the reliability assessment evolves with increasing amount of zones. The PoF (from Eq. 4.13) for increasing amount of load cycles increases. This zoning approach, or discrete approach, was conducted in two ways, first only considering the propagation phase (left plot) and then including the nucleation phase (right plot). By including the nucleation phase, the amount of cycles till failure increases, so the curves shift to the right. Both plots show how, with increasing amount of zones, the probabilities of failure after, e.g., 50.000 cycles, converge to a normalized value P_0. Increasing the zones even further ultimately leads to the continuous, or local, approach.

5.1.3. Continuous Approach

In the continuous approach the flaws are sampled randomly at any location of the disk with respective stress and temperature conditions. Figure 5.3 also shows results for the continuous approach.

The results from the MC simulation can be visualized as an increasing PoF with increasing number of cycles (like in Figure 5.3); it can also be visualized as a risk map, showing the amount of flaws that led to failure for each voxel of the component at a given amount of cycles. Figure 5.4 shows such risk maps after 50.000 cycles for sim-

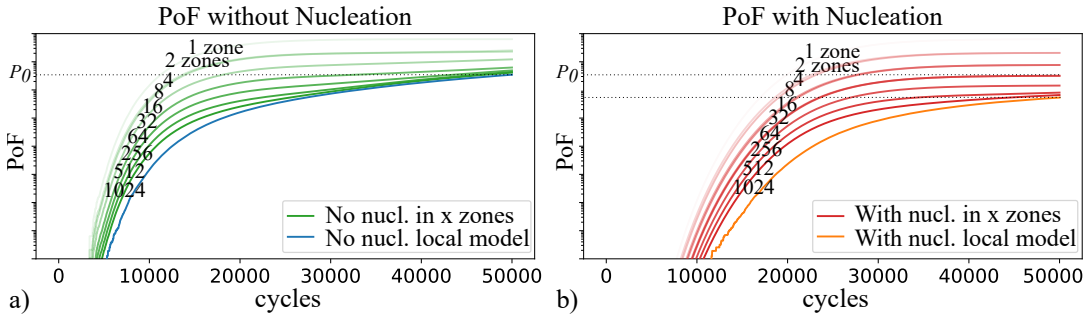

Figure 5.3.: PoF vs. number of load cycles for the discrete, zoning approach on a simplified component. For increasing amount of zones, the results convergence to the continuous, local method. Note that the PoF is in logarithmic scale. (a) Only crack propagation is considered, without nucleation. (b) Both crack nucleation and propagation are accounted for.

ulations performed with only LEFM, with only nucleation and with the combination of both. In the figures we see how the high stresses at the inner side of the disk (left part of the plot) and the overshoot in thermal stresses in the bulk region cause higher risk areas. The upper figure displays the analysis when accounting only for crack propagation, disregarding the nucleation time; this is how *ProbFM* currently works. The middle figure is presented only for showcasing an extreme case where there is only nucleation life and no propagation at all — every nucleated flaw immediately fails. This is obviously not a design case but only visualizes the areas where the nucleation model is of most impact. The lower figure shows the final results of a fully embedded crack nucleation and propagation MC simulation. Where both the nucleation and the propagation are at very high risk, also their combination is. Some regions, like the bulk region, have both a relatively high risk, but their combination is clearly lower. There are also areas where only the propagation has a significant contribution; adding the nucleation results in low risk areas. The general effect of including the nucleation model is that hot-spot areas decrease, and the total assessment becomes less severe.

5.1.4. Discussion

This study was performed to validate the continuous approach, which is the full implementation of *ProbFM*. Important to notice is the fact that the discrete approach is more conservative than the continuous one at all times. This means that for quick calculations — or in absence of precise transient FEA simulations — it is possible to approach the reliability with conservative estimates.

Please note that for preparing the above comparison between the zoning approach and the continuous approach, we reduced complexity significantly by sampling only one sized flaws. The conversion factor k was set to 1, the KSR value fixed to 4 mm,

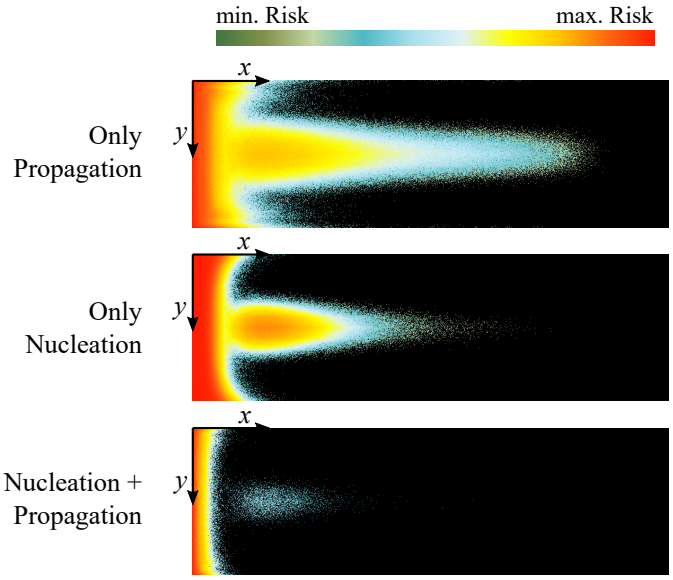

Figure 5.4.: Risk maps of the simplified component showing both FM and Nucleation separately and added to one another.

and the POD distribution reduced to a single factor 1. With this work-around we obtained only samples of flaws with $TFS = 4\,\text{mm}$; this reduced the parameter space considerably for the sake of comparison. All other stochastic parameters, such as $\frac{da}{dN}$ or the nucleation life, remained variable.

5.2. Siemens Energy Gas Turbine Rotor Disk

A real engineering component for rotor disks has a more complex geometry. Especially the thermal analysis needs to be performed diligently due to geometric features. In this section we study the behavior of the upgraded *ProbFM* based on a transient FEA of a real-life component.

5.2.1. Loads and Temperatures of Component

When applying the model to real life components, it is important to realize that complexity increases. There are features such as cooling air bore-holes, blade attachments and torque moment connections. Their FEA is more complex and at times less predictable. Multi-axial loading along the entire transient must be studied carefully in each area. Besides this, one mission profile has a ramp up period, a maximum mechanical load at max speed and a ramp down with eventually minor load cycles in-between. During this mission also the temperature transient plays an important

role. The machine heats up slowly and temperature gradients within a component cause significant thermal loads beside the rotational mechanical load. The applied stress and temperature states represent one specific load mission which is repeated N times. Duty-cycles consisting of a mix of different individual missions can, at least for the FM part, be simulated explicitly. For the LCF part, they could be accounted for by damage accumulation models. Such models include the rainflow-counting algorithm and the Palmgren-Miner rule, in which different load missions are mixed by occurrence and order. Since some of these phenomena are not explicitly accounted for, some simplification must be made under conservative assumptions. One of them is to model the multi-axial reality with a worst-case uni-axial model, since the area-based nucleation model cannot cope with multi-axiality.

5.2.2. Global Effective Nucleation Model and Infant Mortality

Figure 5.5 shows the results of several *ProbFM* computations on a real-life component. We first focus on the blue lines, which show a state-of-the-art computation of *ProbFM* for a turbine rotor disk without accounting for the nucleation phase. The upper two plots show the probability of failure of a rotor disk component (Eq. (4.13)) and the lower plot shows the hazard rate (Eq. (4.14)). I chose this component with the given load profile, because it reveals a typical issue with the hazard rate, namely the infant mortality peak. Infant mortality causes high rates of failure at the very beginning of life. This phenomenon represents all those flaws which are sampled with disadvantageous material properties and fail after only few load cycles. The high hazard rate immediately decreases until a steady-state where only random failures occur. After a long steady-state, wearout begins and the hazard rate increases again, giving life to the so-called bathtub curve. This is not visible in the plot of Figure 5.5, due to the limited amount of cycles of the simulation. The maximum hazard rate is an important parameter for component design. Often the acceptable risks are legally defined on a per year basis. Since the failure mechanism is based on a per cycle analysis, the operational profile of a machine becomes key for the acceptance criteria. The annual risk can be estimated given an annual amount of start-stop cycles of the machine, N_{year} by:

$$H_{year}(N) = \int_{N}^{N+N_{year}} H(N)dN \tag{5.2}$$

where we basically integrate the hazard rate over the amount of cycles ran in one year.

Typically, base-load gas turbines run most of the time and are only shut down for maintenance. Gas turbine operators ask increasingly for higher flexibility, due to the

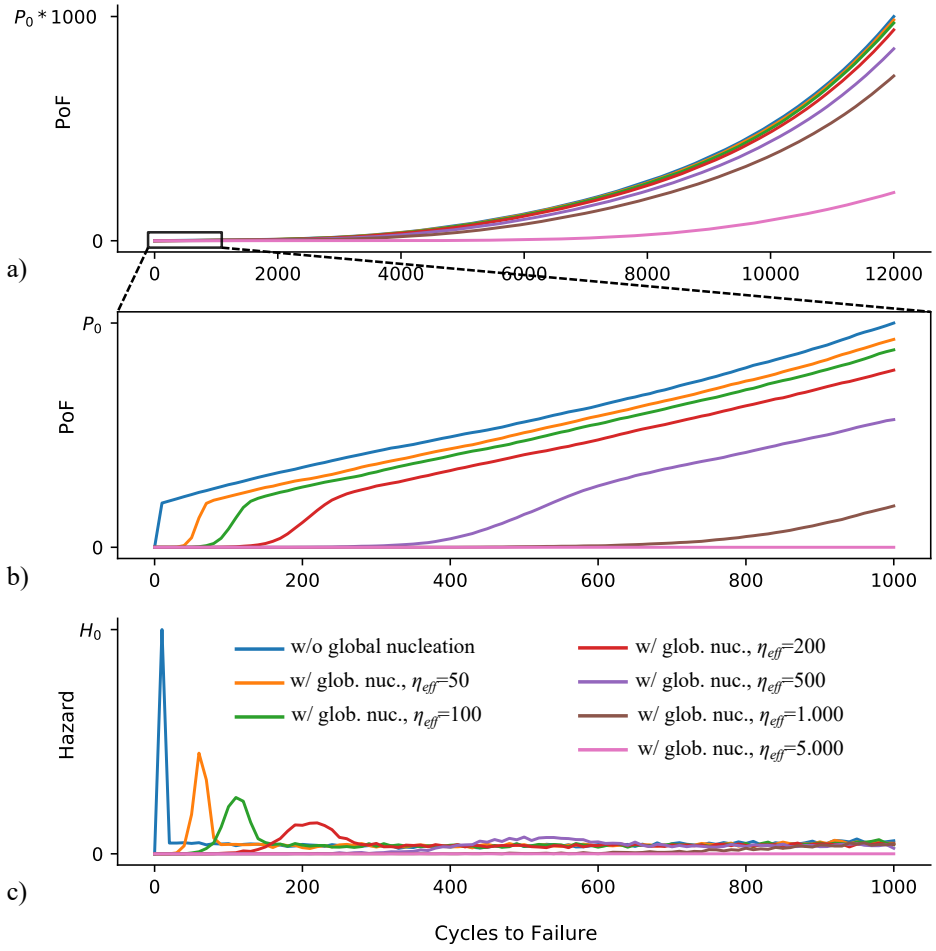

Figure 5.5.: (a)(b)Probability of failure and (c) hazard rate plots for simulations without nucleation and simulations accounting for a global nucleation with equivalent Weibull distribution applied to a rotor disk component. Weibull scale parameter ranging from 50-5000. (b)(c) Focus on initial life span.

increasing volatility of the energy market. The increased amount of energy coming from renewable power sources (wind and solar), causes gas turbines to become more supplementary power sources for covering peaks in demand or troughs in supply, with one or more starts a day. The same type of machine gives lower annual risks in the base-load profile and higher annual risks in the flexible setup. This consideration and also the demands for extending the lifetimes of gas turbines in service, make it extremely attractive to include the nucleation model when assessing crack formation from forging flaws.

As a first approach, the influence of crack nucleation is studied qualitatively, without considering its dependence on flaw size, temperature, stress and location. Instead, representative, effective Weibull shape and scale parameters (m_{eff} and η_{eff}) are selected and applied to the entire component in a global fashion. In other words, the flowchart of Figure 4.28 is followed, only the nucleation is replaced by a one-size-fits-all Weibull function. Of course, this is not a realistic, nor responsible way to account for the nucleation time; this is only a thought exercise in order to visualize the shift in lifetime expectation of a component, as shown in Figure 5.5. Besides the base-case (blue line in Figure 5.5), all other lines account for the additional nucleation time using the global Weibull distribution, ($Weib(m_{\mathit{eff}}, \eta_{\mathit{eff}})$). Different effective scale parameters ($\eta_{\mathit{eff}} = 50 - 5000$) with constant shape parameter ($m_{\mathit{eff}} = 6.5$) are compared. The hazard plots in the figure show how the bathtub curve shifts with increasing η_{eff}. With this example the flattening of the initial peak as consequence of the nucleation can be easily understood. Using the nucleation model in design would give the basis to reliably accept some components, that would otherwise show a high infant mortality peak. Infant mortality of rotor disks has, indeed, never been reported in field experience. This, however, cannot be used as statistical proof, since there is not enough data out there to resolve the extremely small risks at hand. Another advantage of introducing the nucleation model into engineering tools is that it allows new design machines and those in service to extend their lifetimes.

In the next section I will apply the local nucleation model (as proposed in Chapter 4) and see how this locally influences the risk map of a real-life component.

5.2.3. Local Nucleation Model

Figure 5.6 shows a probabilistically calculated risk contour plot for a rotor disk of a gas turbine. For this demonstration, realistic operational data and FEA are used as input to the simulations. Each flaw that led to failure after 120,000 load cycles is represented in these plots. Since failure from a flaw in a well-designed component is an extremely rare event, the amount of load cycles was set unrealistically high to visualize the local spread of probabilities. The local decrease in risk with the nucleation model is clearly

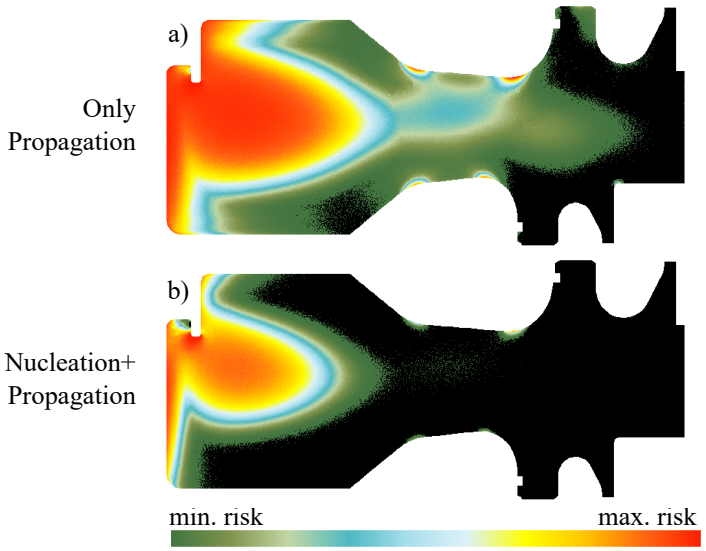

Figure 5.6.: Calculated risk contour plots of a gas turbine rotor disk. (a) accounting only for crack propagation and (b) accounting for both nucleation and crack propagation.

visible. For these simulations the flowchart of Figure 4.28 is used including the local nucleation model which is dependent on flaw size, local temperature and local stress profile. This approach is voxel based. At each voxel there is a certain amount of flaws sampled with given stochastic size distribution and material characteristics. Not all of them fail after 120.000 cycles, those who failed contribute to the risk in the given voxel. This is how the risk map is build. Since there are many flaws in many voxels that do not fail, this calculation is based on billions of brute force MC simulations in order to converge to meaningful and smooth curves.

From these local risks the global probability of failure on component level is obtained by integration over the component. Figure 5.7 shows how these probabilities develop with an increasing number of load cycles. The PoF at 120.000 cycles reflects the situation of Figure 5.6. Also interesting are the results at lower numbers of cycles in the upper panel of the figure. For comparison, also two simulations with the global effective nucleation model (from Section 5.2.2) are plotted. The model with $\eta_{eff} = 10.000$, e.g., compares well with the local nucleation scheme at 20.000 cycles, but they diverge for higher amounts of cycles. These results show the importance of modeling the nucleation life locally. Considering the nucleation life globally would overestimate the local effect in areas where, due to low stresses or temperatures, flaws eventually never nucleate. This very long nucleation life is especially visible in the lower hazard plot, where the hazard rate with local nucleation model never reaches the rate without nucleation even at extremely high numbers of cycles.

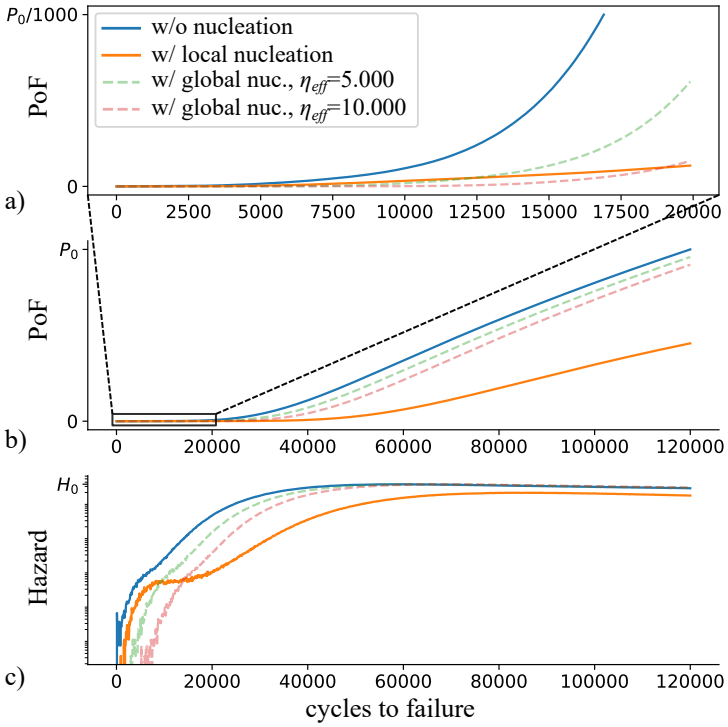

Figure 5.7.: Probabilities of failure and hazard rates for simulations with and without local nucleation. For comparison also two simulations with a global equivalent nucleation are shown. The upper panel ranges from 0-20,000 load cycles, whereas the two lower panels are in a larger scale up to 120,000. Note, the Hazard Rate is in a logarithmic scale.

This component application demonstrates the utility of the probabilistic forging flaw nucleation model. For implementation in design, it is important though to consider conservatism aspects. And, if deemed necessary, lower the expected nucleation life, e.g., with safety factors. Conservatism in the nucleation model has been incorporated by:

- not considering the experiments on flaws with very long nucleation lives, due to e.g. an orthogonal orientation w.r.t. the fracture surface,
- considering the worst case nucleation life in the observed range of typically 2000 or 4000 nucleation cycles,
- using the area observed on the fracture surface, which might not be the largest expansion of the flaw, leads to an over-estimation of the nucleation life when calibrating the model and to an under-estimation of the nucleation life when

applying the model in design,

- making sure that the calibrated model gives probabilistically shorter nucleation life expectations than the observed nucleation lives from the experiments (for all temperatures),
- representing the complex multi-axial transient loading condition of the component with the worst case uni-axial load range,
- practically only surface flaws are used for calibration. Since the area-based model does not distinguish between surface flaws and embedded flaws, this leads to a conservative bias in design, where most flaws are embedded in the components volume.

6. Conclusions

The aim of this work is to demonstrate experimentally that the lifetime of a flaw can be extended by accounting for the crack nucleation phase, besides the already considered propagation phase. This has been done extensively in a testing campaign on specimens from a rotor steel which included forging flaws. From the experiments it was observed that the nucleation time correlates to the applied stress amplitudes, the testing temperature but also to the initial flaw size.

Based on those influencing parameters, three physics based numerical models have been developed. In the first, the geometry of the flaw is represented with a 3D ellipsoid. In the second, only the cross-sectional areas of the flaws are modeled with respective material temperature and the loading conditions during testing. A calibration factor is applied, correcting the expected life to the observed life with a factor. The third is similar to the second with the difference that the calibration factor is not applied on the expected life, instead, a stress concentration factor is calibrated to test results. The crack nucleation is described as a LCF process where cracks are initiated under cyclic loading and microcracks develop from the flaw region into the matrix material. This modeling approach is a local probabilistic one, under the assumption of a Weibull distributed crack initiation, able to capture the size effect of the flaws. All three numerical models are calibrated to the experimental observations using a MLE method under conservative assumptions. The first, ellipsoid-based, had the advantage that it accounts for plasticity at the developing crack front. For varying temperatures it gives decent results; but is not reflecting the Weibull curve properly. The second, area-based model, approaches the Weibull assumption better for each individual temperature. This model does not account for plasticity on the crack front; ideal would be to use the area-based approach with the ability to locally account for plasticity, which is done in the third model.

Once the model was stable and deemed to reliably predict crack nucleation, it has been implemented within a probabilistic framework for fracture mechanics computations of flaws in forged rotor disks. This is a framework that samples up to billions of flaws within a component through brute force MC simulations. The flaws are stochastically distributed based on UT findings, considering probabilities of detection and conversion factors from UT-signals to true flaw sizes. Also the material properties are stochastic and vary along the samples. The MC simulations are collected in a

risk map of the component, highlighting the regions with higher probabilities of crack failure from forging flaws. Also PoF and hazard rate curves are generated, where the PoF increases with higher amounts of load cycles. These curves form the basis for acceptance criteria and reliability assessments of components. Due to the addition of the nucleation phase within this computational framework, the design lifetime of components could be reliably extended.

7. Outlook

This methodology rests on continuous update of material properties based on testing. This impacts the flaw size distribution found with UT, the conversion factor, k, but also matrix material properties relevant for fracture mechanics and LCF. One very promising development would be to substitute the 2-parameter Weibull distribution into a 3-parameter Weibull distribution with a threshold value or a bounded kind of distribution describing the local probability for crack initiation. Such a distribution would better adhere to the physical evidence that there is a minimum amount of cycles under which no crack initiation was ever observed and also that for most materials there seem to be an endurance limit. There could be an upper limit defining the objective material limit in the best case scenario. The tail of the Weibull distribution is infinitely long, but the amount of load cycles on a material are (above the endurance limit) not infinite, this should be reflected in the upper bound. Despite this theoretical argumentation, there are still some practical hurdles to deviating from the 2-parameter Weibull distribution. One is the problem of setting a value for those bounds which are, by definition, extremely improbable to be observed empirically. Should the threshold vary at different strain levels? Can numerical probability functions be adopted like ECDFs? How will this play a role in a local probabilistic approach, where the size effect of a loaded surface plays a crucial role? These hurdles must be thought out thoroughly and need to be based on experimental evidence beside theoretical suspects. Further extending the testing campaign on specimens from forgings including flaws would also be beneficial for the model, providing a larger statistical basis for its calibration. Unfortunately, such testing campaigns are expensive and unlikely to be repeated in the near future.

Besides further refining the material database, it can be also useful to build surrogate models able to predict probabilities of crack failure based on changing loading conditions. Oftentimes the reliability assessments are done considering worst case loading conditions or fixed operational profiles, e.g. cold start base-load conditions. Consequence of the current energy transformation is an increase in flexibility and operational profile of gas turbines. Machine learning algorithms can be trained to assess the contributions from each load profile and also sequences of multiple different load conditions, approaching a digital twin simulation. The present *ProbFM* framework could form the nucleus around which ML algorithms can be deployed as wrappers.

The presented approach considers almost all input parameters as stochastic quantities with a measured scatter. Only the temperature and the stress fields, obtained from thermal-mechanical FEAs in conjunction with whole engine models of the gas turbine, are treated as deterministic values without scatter. Setting-up those analyses stochastically is not trivial! Scatter in temperature e.g. is driven by variation in heat conductivity, heat transfer coefficient and specific heat capacity of the material, but also by uncertainties in the whole engine model. Scatter in stresses is mainly driven by variation of the Young's modulus. Stochastic FEA's are not commonly used yet, since there are no good solutions for implementing the aforementioned uncertainties properly. At present, stringent boundary conditions are considered for the FEA, such that the outcomes are conservative. As technological improvements are made and fast solvers developed, also those scatters can be captured within the *ProbFM* framework and conservatism reduced.

Promising results are expected from the follow-up project *Understanding Crack Nucleation*, owned by the Department of Energy, partnered by Siemens Energy and executed at the Los Alamos National Laboratories. In this project high performance computing (HPC) is applied to peridynamic models of forging flaws in steel rotor disks. This is a microscale model where the crack nucleation from forging flaws is approached in a more fundamental way and not only effectively, as presented in this thesis. Such peridynamic simulations seem to give more insight in the internal development of microcracks within the cluster of particles of one flaw, see Figure 4.19. First results of this research have already been published by Karim et al. [74; 75]. General information about the project can be found on the website "www.hpc4mtls.llnl.gov/projects.html". From first simulations it appears that the nucleation life of inclusions does not depend much of the extension of the field of inclusions in the load direction. When the flaw is modeled with a large extension in z-direction, we see that several competing microcracks are initiated above each other of which only one evolves into a long crack leading to failure. Whereas, if this z-dimension is small, there is only one microcrack initiated. This leads to a statistical size effect where more competing microcracks are statistically more likely to generate one long crack. The small depth extension is not causing significant increases in local stresses.

The effort put into this project for the time being is confined to one specific rotor steel. It would be extremely beneficial to transfer the know-how acquired in this project to other similar forged materials without the need to repeat specific testing campaigns on specimens with flaws for each new material. In principle this is possible if the considered flaws are of the same typology as in this current project and if there are sufficient LCF tests available allowing the local probabilistic LCF method to work properly. One special point of interest is the scatter parameter of the Weibull curve, m.

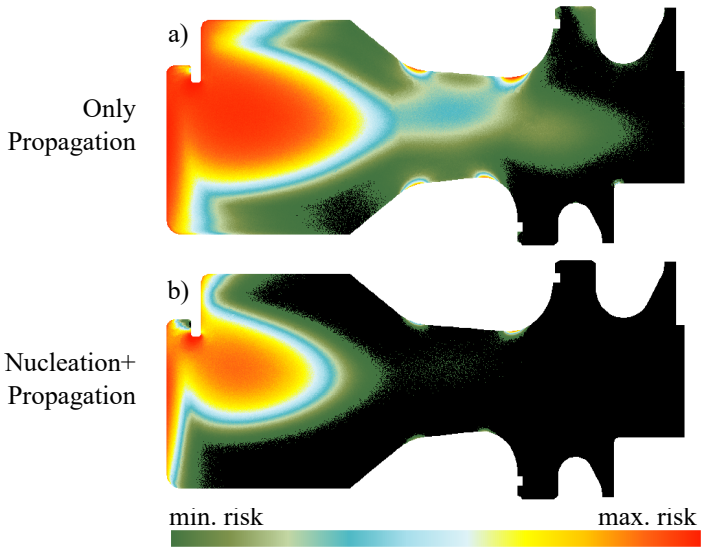

Figure 7.1.: Illustration of the effect of adding the nucleation life to the propagation on a real life component. The risk contour plot relaxes locally due to a prolongation of life of the sampled flaws. (a) accounting only for crack propagation and (b) accounting for both nucleation and crack propagation. Note, the contours are shown on a linear scale over a range of four decades, each contour has the same range.

This is a parameter which is often debated. For the current steel we have experimental data available for calibrating the nucleation model, which make the correctness of m of less importance. For new materials there are no calibration points available and the importance of m becomes decisive. Efforts should be put in understanding m, its uncertainty and applicability.

One step further would be to apply the methodology presented here to other types of materials and other typologies of flaws. Good candidates are e.g. dirty white spots found in nickel-alloys such as IN718 [21], hard alpha inclusions in titanium disks or even porosity in castings and additive manufacturing. Recently, Siemens Energy initiated a government funded project (ROBOFLEX), in collaboration with Fraunhofer IWM, where specimens from blade castings with porosity are tested and a crack initiation model will be developed. Findings from the current project will certainly be transferred to the ROBOFLEX project. One strong characteristic of the presented approach is that it accounts for the size-effect of the flaws; but one should not forget the validity range for the LCF model. As soon as flaw enters the scale size of the material structure, the crack formation process fundamentally changes; other approaches should be considered then.

The crack nucleation model presented here has been successfully implemented within

an engineering tool used at Siemens Energy. It may become a key enabler for some parts, especially under the current changing conditions where more flexible use of engines is required. Figure 7.1, already shown in Chapter 5, illustrates some key results of adding the nucleation life to the fracture mechanical life for a real-life component, demonstrating the relaxation of some areas with the local reduction of risk. Nevertheless, the approach should be included in formal design philosophies and further challenged and validated by component designers. After a period of utilization within pilot projects it will gain general recognition and widespread application.

Bibliography

[1] The development of anomaly distributions for aircraft engine titanium disk alloys. In *38th Structures, Structural Dynamics, and Materials Conference*, Structures, Structural Dynamics, and Materials and Co-located Conferences. American Institute of Aeronautics and Astronautics, 1997. doi:10.2514/6.1997-1068.

[2] Abinger, R., Hammer, F., and Leopold, J. Großschaden an einem 330-mw-dampfturbosatz, 1988. Allianz: Der Maschinenschaden.

[3] Ai, Y., Zhu, S. P., Liao, D., Correia, J., Souto, C., de Jesus, A., and Keshtegar, B. Probabilistic modeling of fatigue life distribution and size effect of components with random defects. *International Journal of Fatigue*, 126:165–173, 2019. ISSN 01421123. doi:10.1016/j.ijfatigue.2019.05.005.

[4] Amann, C. *Probabilistic Fracture Mechanics of Forged Rotor Disks*. PhD thesis, KIT, Karlsruhe (Germany), 2017.

[5] Amann, C. and Kadau, K. Numerically efficient modified runge–kutta solver for fatigue crack growth analysis. *Engineering Fracture Mechanics*, 161:55–62, 2016. ISSN 00137944. doi:10.1016/j.engfracmech.2016.03.021.

[6] Amann, C., Gravett, P. W., and Kadau, K. Method and system for probabilistic fatigue crack life estimation, 2016. URL `patents.google.com/patent/US9280620`. US Patent 9,280,620 B2.

[7] Amann, C., Kadau, K., and Gumbsch, P. On the transferability of probabilistic fracture mechanics results for scaled 50hz and 60hz heavy duty gas turbine rotor disks. In *Proceedings of ASME Turbo Expo 2018*, pages GT2018–75561, 2018. doi:10.1115/GT2018-75561.

[8] Annis, C. Probabilistic life prediction isn't as easy as it looks. *Journal of ASTM International*, 1(2):11557, 2004. ISSN 1546962X. doi:10.1520/JAI11557.

[9] Asquith, G. The role of component testing. *AGARD, AGARD/SMP Review Damage Tolerance for Engine Structures. 3: Component Behaviour and Life Management 19 p(SEE N 90-27704 22-07)*, 1990.

[10] Berger, C., Mayer, K. H., Oberparleiter, W., and Scarlin, R. B. Initiation of fatigue cracks at non-metallic inclusions in large forgings. *Fracture 84*, pages 2107–2116, 1984. doi:10.1016/B978-1-4832-8440-8.50213-1.

[11] Berger, C. and Maldfeld, E. Fehler in Gasturbinenscheiben bruchmechanisch bewerten: Prof. Dr.-Ing. habil. Dr.e.h. Horst Blumenauer zum 65. Geburtstag. *Materialprüfung*, 42:S. 26–30, 2000. URL tubiblio.ulb.tu-darmstadt.de/14949/.

[12] Bitzek, E. and Gumbsch, P. Mechanisms of dislocation multiplication at crack tips. *Acta Materialia*, 61(4):1394–1403, 2013. ISSN 13596454. doi:10.1016/j.actamat.2012.11.016.

[13] Chaboche, J. L. Continuum damage mechanics: Part I: General concepts. *Journal of Applied Mechanics*, 55(1):59–64, 1988. ISSN 00218936. doi:10.1115/1.3173661.

[14] Chapetti, M. D. and Guerrero, A. O. Estimation of notch sensitivity and size effect on fatigue resistance. *Procedia Engineering*, 66:323–333, 2013. ISSN 18777058. doi:10.1016/j.proeng.2013.12.087.

[15] Chen, B., Jiang, J., and Dunne, F. P. Microstructurally-sensitive fatigue crack nucleation in ni-based single and oligo crystals. *Journal of the Mechanics and Physics of Solids*, 106:15–33, 2017. ISSN 00225096. doi:10.1016/j.jmps.2017.05.012.

[16] Chen, B., Jiang, J., and Dunne, F. P. Is stored energy density the primary mesoscale mechanistic driver for fatigue crack nucleation? *International Journal of Plasticity*, 101:213–229, 2018. ISSN 07496419. doi:10.1016/j.ijplas.2017.11.005.

[17] Coffin, L. F., JR. *A study of the effects of cyclic thermal stresses on a ductile metal*, volume 853. Knolls Atomic Power Laboratory, Schenectady, New York, 1953.

[18] Craig McClung, R., Lee, Y.-D., Enright, M. P., and Liang, W. New methods for automated fatigue crack growth and reliability analysis. *Journal of Engineering for Gas Turbines and Power*, 136(6):185, 2014. ISSN 0742-4795. doi:10.1115/1.4026140.

[19] Deyber, S., Alexandre, F., Vaissaud, J., and Pineau, A. Probabilistic life of da 718 for aircraft engine disks. In E.A. Loria, editor, *Superalloys 718, 625, 706 and derivatives*, volume v1, page 14 p. TMS, Pittsburgh, United States, 2005. URL hal.archives-ouvertes.fr/hal-00833002.

[20] Domokos, G., Kun, F., Sipos, A. Á., and Szabó, T. Universality of fragment shapes. *Scientific reports*, 5:9147, 2015. doi:10.1038/srep09147.

[21] Donald Kramer. Materials laboratory factual report: Report no. 17-034, 2017.

[22] Enright, M. P. and McClung, R. C. A probabilistic framework for gas turbine engine materials with multiple types of anomalies. *Journal of Engineering for Gas Turbines and Power*, 133(8):355, 2011. ISSN 0742-4795. doi:10.1115/1.4002675.

[23] Enright, M. P., McClung, R. C., Liang, W., Lee, Y.-D., Moody, J. P., and Fitch, S. A tool for probabilistic damage tolerance of hole features in turbine engine rotors. In *Proceedings of ASME Turbo Expo 2012*, pages 447–458, 2012. ISBN 978-0-7918-4473-1. doi:10.1115/GT2012-69968.

[24] Enright, M. P., Moody, J. P., and Sobotka, J. C. Optimal automated fracture risk assessment of 3d gas turbine engine components. In *Proceedings of ASME Turbo Expo 2016*, 2016. ISBN 978-0-7918-4984-2. doi:10.1115/GT2016-58091.

[25] EricksonKirk, M., Bass, B. R., Dickson, T., Pugh, C., Santos, T., and Williams, P. Probabilistic fracture mechanics — models, parameters, and uncertainty treatment used in favor version 04.1 (nureg-1807), 2007.

[26] FKM. Richtlinie nichtlinear: Rechnerischer bauteilfestigkeitsnachweis unter expliziter erfassung nichtlinearen werkstoff-verformungsverhaltens, 2016.

[27] Foth, J. and Oberparleiter, W. *Fehlstelleneinfluß II; Untersuchung des rißauslösenden Einflusses natürlicher makroskopischer Fehlstellen und Fehlergruppen in größeren Schmiedestücken bei betriebsähnlichen Spannungen und Temperaturen; Abschlußbericht Teil I: Versuchsergebnisse*, volume 302. FVV, Frankfurt/M., 1987.

[28] Glinka, G. Energy density approach to calculation of inelastic strain-stress near notches and cracks. *Engineering Fracture Mechanics*, 22(3):485–508, 1985. ISSN 00137944. doi:10.1016/0013-7944(85)90148-1.

[29] Guan, X., Zhang, J., Zhou, S., Rasselkorde, E. M., and Abbasi, W. Probabilistic modeling and sizing of embedded flaws in ultrasonic non-destructive inspections for fatigue damage prognostics and structural integrity assessment. *NDT & E International*, 61:1–9, 2014. ISSN 09638695. doi:10.1016/j.ndteint.2013.09.003.

[30] Gumbsch, P., Riedle, J., Hartmaier, A., and Fischmeister, H. F. Controlling factors for the brittle-to-ductile transition in tungsten single crystals. *Science (New York, N.Y.)*, 282(5392):1293–1295, 1998. doi:10.1126/science.282.5392.1293.

[31] Heinrich, D., Mayer, K.-H., Müller, G., and Prestel, W. Manual and mechanized ultrasonic inspection of large components in respect of flaw estimation by fracture mechanics. *Nuclear Engineering and Design*, 112:127–137, 1989. ISSN 00295493. doi:10.1016/0029-5493(89)90151-9.

[32] Hu, D., Wang, T., Ma, Q., Liu, X., Shang, L., Li, D., Pan, J., and Wang, R. Effect of inclusions on low cycle fatigue lifetime in a powder metallurgy nickel-based superalloy fgh96. *International Journal of Fatigue*, 118:237–248, 2019. ISSN 01421123. doi:10.1016/j.ijfatigue.2018.09.019.

[33] Huron, E. S. and Roth, P. G. The influence of inclusions on low cycle fatigue life in a p/m nickel-base disk superalloy. *Superalloys*, pages 359–368, 1996. doi:10.7449/1996/Superalloys_1996_359_368.

[34] Jeal R. Damage tolerance concepts for critical engine components. In *60th SMP-AGARD Meeting*, 1985.

[35] Jestrich, H. A., Prestel, W., Heinrich, D., and Schmalenbeck, W. Die bedeutung der ersatzreflektorgröße für die bruchmechanik, untersucht an schweren sehmiedestücken für turbomaschinen. In *DGZfP Conf*, volume 29, 1986.

[36] Jiang, J., Yang, J., Zhang, T., Zou, J., Wang, Y., Dunne, F., and Britton, T. B. Microstructurally sensitive crack nucleation around inclusions in powder metallurgy nickel-based superalloys. *Acta Materialia*, 117:333–344, 2016. ISSN 13596454. doi:10.1016/j.actamat.2016.07.023.

[37] Kadau, K., Germann, T. C., Lomdahl, P. S., and Holian, B. L. Microscopic view of structural phase transitions induced by shock waves. *Science (New York, N.Y.)*, 296(5573):1681–1684, 2002. doi:10.1126/science.1070375.

[38] Kadau, K., Gravett, P. W., and Amann, C. Probabilistic fracture mechanics for heavy-duty gas turbine rotor forgings. *Journal of Engineering for Gas Turbines and Power*, 140(6):062503, 2018. ISSN 0742-4795. doi:10.1115/1.4038524.

[39] Kadau, K., Ross, C. W., Patel, C. B., and Amann, C. Method for analysis of 3d features using a 2d probabilistic analysis, 2018. URL `patents.google.com/patent/WO2015200158A1/en`. US Patent 9,857,242 B2.

[40] Kern, T.-U., Ewald, J., and Maile, K. Evaluation of ndt-signals for use in the fracture mechanics safety analysis. *Materials at High Temperatures*, 15(2): 107–110, 1998. ISSN 0960-3409. doi:10.1080/09603409.1998.11689587.

[41] Kiefer, J. Sequential minimax search for a maximum. *Proceedings of the American Mathematical Society*, 4(3):502, 1953. ISSN 00029939. doi:10.2307/2032161.

[42] Knop, M. On the glinka and neuber methods for calculating notch tip strains under cyclic load spectra. *International Journal of Fatigue*, 22(9):743–755, 2000. ISSN 01421123. doi:10.1016/S0142-1123(00)00061-X.

[43] Kun, F. and Herrmann, H. J. A study of fragmentation processes using a discrete element method. *Computer Methods in Applied Mechanics and Engineering*, 138 (1-4):3–18, 1996. ISSN 00457825. doi:10.1016/S0045-7825(96)01012-2.

[44] Lin, T. H. and Ito, Y. M. Fatigue crack nucleation in metals. In *Proceedings of the National Academy of Science*, volume 62, pages 631–635. 1968.

[45] Mäde, L., Gottschalk, H., Schmitz, S., Beck, T., and Rollmann, G. Probabilistic lcf risk evaluation of a turbine vane by combined size effect and notch support modeling. In *Proceedings of ASME Turbo Expo 2017*, page V07AT32A004, 2017. doi:10.1115/GT2017-64408.

[46] Mäde, L., Schmitz, S., Gottschalk, H., and Beck, T. Combined notch and size effect modeling in a local probabilistic approach for lcf. *Computational Materials Science*, 142:377–388, 2018. ISSN 09270256. doi:10.1016/j.commatsci.2017.10.022.

[47] Manson, S. S. Behavior of materials under conditions of thermal sterss: Naca report 1170, 1954.

[48] Mayer, K. H., Berger, C., Heinrich, D., and Scarlin, B. Evaluation by fracture mechanics of ultrasonic indications in turbine and generator rotors. *Nuclear Engineering and Design*, 137(3):277–289, 1992. ISSN 00295493. doi:10.1016/0029-5493(92)90251-P.

[49] Mayer, K. H., Berger, C., Gnirss, G., Heinrich, D., and Prestel, W. Investigations by non-destructive inspection to determine the size of natural defects in large forgings of turbogenerators. *Nuclear Engineering and Design*, 144(1): 155–170, 1993. ISSN 00295493. doi:10.1016/0029-5493(93)90017-4.

[50] Mayer, K. H., Prestel, W., Weber, D., and Weiss, M. In-service inspection and defect assessment of steam turbine rotors. *International Journal of Pressure Vessels and Piping*, 66(1-3):281–292, 1996. ISSN 03080161. doi:10.1016/0308-0161(95)00102-6.

[51] McDowell, D., Gall, K., Horstemeyer, M., and Fan, J. Microstructure-based fatigue modeling of cast a356-t6 alloy. *Engineering Fracture Mechanics*, 70(1): 49–80, 2003. ISSN 00137944. doi:10.1016/S0013-7944(02)00021-8.

[52] Mises, R. v. Mechanik der festen körper im plastisch- deformablen zustand. *Nachrichten von der Gesellschaft der Wissenschaften zu Göttingen, Mathematisch-Physikalische Klasse*, 1913:582–592, 1913. URL eudml.org/doc/58894.

[53] Molski, K. and Glinka, G. A method of elastic-plastic stress and strain calculation at a notch root. *Materials Science and Engineering*, 50(1):93–100, 1981. ISSN 00255416. doi:10.1016/0025-5416(81)90089-6.

[54] Mooshofer, H., Boehm, R., Heinrich, W., Fendt, K., Goldammer, M., Kolk, K., and Vrana, J. Amplitude-based defect sizing of saft-results - from imaging to quantitative measurement. In *ECNDT*, 2018.

[55] Mooshofer, H., Schörner, K., Nespoli, N., Vrana, J., and Kolk, K. Validierung von saft für die herstellungsprüfung von turbinenscheiben. In *DACH-Jahrestagung*, 2019.

[56] Murakami, Y. *Metal fatigue: Effects of small defects and nonmetallic inclusions*. Academic Press, Amsterdam, second edition edition, 2019. doi:10.1016/C2016-0-05272-5.

[57] Nakao, M. Brittle fracture of turbine rotor in nagasaki, 1970. URL shippai.org/fkd/en/hfen/HA1000601.pdf.

[58] Nakao, M. Fracture of turbine shaft in wakayama, 1972. URL shippai.org/fkd/en/hfen/HA1000602.pdf.

[59] Naragani, D., Sangid, M. D., Shade, P. A., Schuren, J. C., Sharma, H., Park, J.-S., Kenesei, P., Bernier, J. V., Turner, T. J., and Parr, I. Investigation of fatigue crack initiation from a non-metallic inclusion via high energy x-ray diffraction microscopy. *Acta Materialia*, 137:71–84, 2017. ISSN 13596454. doi:10.1016/j.actamat.2017.07.027.

[60] Nitta, A. and Kobayashi, H. Burst of steam turbine rotor in nuclear power plant, 1969. URL shippai.org/fkd/en/hfen/HB1031029.pdf.

[61] Nitta, A. and Kobayashi, H. Burst of steam turbine rotor in fossil power plant, 1974. URL shippai.org/fkd/en/hfen/HB1031027.pdf.

[62] Oberparleiter, W. *Fehlstelleneinfluß I: Untersuchung des rißauslösenden Einflusses natürlicher makroskopischer Fehlstellen in größeren Schmiedestücken unter Zugschwellenbeanspruchung und bei niedrigen Lastspielzahlen N<25.000: Abschlußbericht*, volume 248. FVV, Frankfurt, 1983.

[63] Paris, P. and Erdogan, F. A critical analysis of crack propagation laws. *Journal of Basic Engineering*, 85(4):528–533, 1963. ISSN 0021-9223. doi:10.1115/1.3656900.

[64] Pineau, A. and Antolovich, S. D. Probabilistic approaches to fatigue with special emphasis on initiation from inclusions. *International Journal of Fatigue*, 93:422–434, 2016. ISSN 01421123. doi:10.1016/j.ijfatigue.2016.09.002.

[65] Polák, J., Mazánová, V., Heczko, M., Petráš, R., Kuběna, I., Casalena, L., and Man, J. The role of extrusions and intrusions in fatigue crack initiation. *Engineering Fracture Mechanics*, 185:46–60, 2017. ISSN 00137944. doi:10.1016/j.engfracmech.2017.03.006.

[66] Polák, J. and Man, J. Experimental evidence and physical models of fatigue crack initiation. *International Journal of Fatigue*, 91:294–303, 2016. ISSN 01421123. doi:10.1016/j.ijfatigue.2016.02.021.

[67] Prasannavenkatesan, R., Zhang, J., McDowell, D. L., Olson, G. B., and Jou, H.-J. 3d modeling of subsurface fatigue crack nucleation potency of primary inclusions in heat treated and shot peened martensitic gear steels. *International Journal of Fatigue*, 31(7):1176–1189, 2009. ISSN 01421123. doi:10.1016/j.ijfatigue.2008.12.001.

[68] Radaelli, F., Amann, C., Kadau, K., Schmitz, S., and Vöse, M. Computer-implemented method for the probabilistic estimation of a probability of failure of a component, a data processing system, a computer program product and a computer-readable storage medium, 2019. URL patentscope.wipo.int/search/en/detail.jsf?docId=WO2020089402. Patent WO/2020/089402.

[69] Radaelli, F., Kadau, K., Amann, C., and Gumbsch, P. Probabilistic fracture mechanics framework including crack nucleation of rotor forging flaws. In *Proceedings of ASME Turbo Expo 2019*, pages GT2019–90418, 2019. doi:10.1115/GT2019-90418.

[70] Radaelli, F., Amann, C., Aydin, A., Varfolomeev, I., Gumbsch, P., and Kadau, K. A probabilistic model for forging flaw crack nucleation processes. *Journal of*

Engineering for Gas Turbines and Power, 143(10):185, 2021. ISSN 0742-4795. doi:10.1115/1.4051426.

[71] Radaelli, F., Amann, C., Aydin, A., Varfolomeev, I., Gumbsch, P., and Kadau, K. A probabilistic model for forging flaw crack nucleation processes for heavy duty gas turbine rotor operations. In *Proceedings of ASME Turbo Expo 2022*, pages GT2020–14606, 2022.

[72] Ramanujan Aiyangar, S., Hardy, G. H., Seshu Aiyar, P. V., and Wilson, B. M. *Collected papers of Srinivasa Ramanujan*. AMS Chelsea Pub, Providence, RI, 2000. ISBN 9780821820766.

[73] Rathi, G, M., and Jakhade, N. A. An overview of forging processes with their defects. *International Journal of Scientific and Research Publications*, 4(6):1–7, 2014.

[74] Rezaul Karim, M., Kadau, K., Narasimhachary, S., Radaelli, F., Amann, C., Dayal, K., Silling, S., and Germann, T. C. Crack nucleation at forging flaws studied by non-local peridynamics simulations. *Mathematics and Mechanics of Solids*, 1961:108128652110572, 2021. ISSN 1081-2865. doi:10.1177/10812865211057211.

[75] Rezaul Karim, M., Kadau, K., Narasimhachary, S., Radaelli, F., Amann, C., Dayal, K., Silling, S., and Germann, T. C. Crack nucleation from non-metallic inclusions in aluminum alloys described by peridynamics simulations. *International Journal of Fatigue*, 153:106475, 2021. ISSN 01421123. doi:10.1016/j.ijfatigue.2021.106475.

[76] Riemelmoser, F. O., Gumbsch, P., and Pippan, R. Dislocation modelling of fatigue cracks: An overview. *Materials Transactions*, 42(1):2–13, 2001. doi:10.2320/matertrans.42.2.

[77] Romano, S., Miccoli, S., and Beretta, S. A new fe post-processor for probabilistic fatigue assessment in the presence of defects and its application to am parts. *International Journal of Fatigue*, 125:324–341, 2019. ISSN 01421123. doi:10.1016/j.ijfatigue.2019.04.008.

[78] Roth, P. G. *Probabilistic Rotor Design System (PRDS): Gas Turbine Engine Design*. Air Force Research Laboratory, Cincinnati, Ohio, 1998.

[79] Sangid, M. D. The physics of fatigue crack initiation. *International Journal of Fatigue*, 57:58–72, 2013. ISSN 01421123. doi:10.1016/j.ijfatigue.2012.10.009.

[80] Scarlin, R. B., Berger, C., Mayer, K. H., and Oberparleiter, W. Fatigue crack initiation and propagation from inclusions in steel forgings. In *European Conference on Fracture (ECF5)*, 1984.

[81] Schäfer, B., Sonnweber-Ribic, P., ul Hassan, H., and Hartmaier, A. Micromechanical modeling of fatigue crack nucleation around non-metallic inclusions in martensitic high-strength steels. *Metals*, 9(12):1258, 2019. doi:10.3390/met9121258.

[82] Schmitz, S. *A local and probabilistic model for low-cycle fatigue: New aspects of structural analysis*. PhD thesis, Università della Svizzera Italiana, Lugano (Switzerland), 2014.

[83] Schmitz, S., Gottschalk, H., Rollmann, G., and Krause, R. Risk estimation for lcf crack initiation. In *Proceedings of ASME Turbo Expo 2013*, volume 7A, pages GT2013–94899, 2013. doi:10.1115/GT2013-94899.

[84] Schmitz, S., Rollmann, G., Gottschalk, H., and Krause, R. Probabilistic analysis of lcf crack initiation life of a turbine blade under thermomechanical loading. In *International Conference on Low Cycle Fatigue*, Berlin, 2013. DVM. ISBN 9783981451627. doi:10.48550/arXiv.1310.0629.

[85] Schmitz, S., Seibel, T., Beck, T., Rollmann, G., Krause, R., and Gottschalk, H. A probabilistic model for lcf. *Computational Materials Science*, 79:584–590, 2013. ISSN 09270256. doi:10.1016/j.commatsci.2013.07.015.

[86] Schörner, K., Mooshofer, H., Zimmer, A., Vrana, J., and Kolk, K. Praxiserfahrungen beim einsatz der saft- software von siemens. In *DACH-Jahrestagung*, 2019.

[87] Schwant, R. C. and Timo, D. P. Inspection and life evaluation of general electric turbine rotors. *ASME Paper*, 1984.

[88] Schwant, R. C. and Timo, D. P. Life assessment of general electric large steam turbine rotors. *Proceedings of the Seminar on Life Assessment and Improvement of Turbo-Generator Rotors for Fossil Plants*, 1984.

[89] Siegele, D., Reißig, L., Sguaizer, Y., Schüler, J., Burdack, M., and Varfolomeev, I. Investigation to the extension of flaws under cyclic loading: Iwm report v 373/2011, 2013.

[90] SINTAP. *Structural integrity assessment procedures for European industry*. Final procedure edition.

[91] Smith, K. N., Watson, P., and Topper, T. H. A stress-strain function for the fatigue of metals. *Journal of Materials*, 5(4):767–778, 1970.

[92] Socie, D. F. and Morrow, J. Review of contemporary approaches to fatigue damage analysis. In Burke, J. J. and Weiss, V., editors, *Risk and Failure Analysis for Improved Performance and Reliability*, pages 141–194. Springer US, Boston, MA, 1980. ISBN 978-1-4684-7811-2. doi:10.1007/978-1-4684-7811-2_8.

[93] Soille, P. and Vincent, L. M. Determining watersheds in digital pictures via flooding simulations. In *Proceedings of SPIE*, volume 1360, pages 240–250, 1990. doi:10.1117/12.24211.

[94] Stojmenovic, M. and Nayak, A. Direct ellipse fitting and measuring based on shape boundaries. In Mery, D. and Rueda, L., editors, *Advances in Image and Video Technology*, volume 4872 of *Lecture Notes in Computer Science*, pages 221–235, Berlin, Heidelberg, 2007. Springer Berlin Heidelberg. ISBN 978-3-540-77128-9. doi:10.1007/978-3-540-77129-6_22.

[95] Tryon, R. G. and Cruse, T. A. A reliability-based model to predict scatter in fatigue crack nucleation life. *Fatigue & Fracture of Engineering Materials and Structures*, 21(3):257–267, 1998. ISSN 8756-758X. doi:10.1046/j.1460-2695.1998.00024.x.

[96] U.S. Department of Transportation Federal Aviation Administration. Ac 33.14-1—damage tolerance for high energy turbine engine rotors: U.s.d. of t.f.a., 3/7/17.

[97] U.S. National Transportation Safety Board. Safety recommendation: A-06-60 through -64, 2006.

[98] U.S. National Transportation Safety Board. Powerplant group chairman's factual report: Ntsb no: Dca17fa021, 2017.

[99] Varfolomeev, I., Moroz, S., Siegele, D., Kadau, K., and Amann, C. Study on fatigue crack initiation and propagation from forging defects. *Procedia Structural Integrity*, 7:359–367, 2017. ISSN 24523216. doi:10.1016/j.prostr.2017.11.100.

[100] Vollrath, K. *Simulation in the forging industry.* Forging industry information service. Industrieverb. Massivumformung, Hagen, special ed. edition, 2013. ISBN 978-3-928726-31-3.

[101] Vrana, J., Zimmer, A., Lohman, H.-P., and Heinrich, W. Evolution of the ultrasonic inspection over the past decades on the example of heavy rotor forgings. In *19th World Conference on Non-Destructive Testing*, 2016. doi:10.13140/RG.2.1.5017.5603.

[102] Vrana, J., Kadau, K., and Amann, C. Smart data analysis of the results of ultrasonic inspections for probabilistic fracture mechanics. In *MPA-Seminar*. MPA, 2017.

[103] Vrana, J., Schörner, K., Mooshofer, H., Kolk, K., Zimmer, A., and Fendt, K. Ultrasonic computed tomography – pushing the boundaries of the ultrasonic inspection of forgings. *Steel Research International*, 89(4):1700448, 2018. doi:10.1002/srin.201700448.

[104] Vrana, J., Zimmer, A., Schörner, K., Mooshofer, H., and Kolk, K. Erfahrungen bei der einführung der saft prüfung in die serienfertigung großer schmiedeteile. In *DACH-Jahrestagung*, 2019.

[105] Weichert, C. *Auswirkungen eines dreiachsigen Spannungszustandes auf das Verformungsverhalten und das Rissinitiierungsverhalten von Gruppenfehlstellen*. Dissertation, Universität Stuttgart, Stuttgart, Germany, 2004.

[106] Zerbst, U., Madia, M., Klinger, C., Bettge, D., and Murakami, Y. Defects as a root cause of fatigue failure of metallic components. ii: Non-metallic inclusions. *Engineering Failure Analysis*, 98:228–239, 2019. ISSN 13506307. doi:10.1016/j.engfailanal.2019.01.054.

[107] Zhang, T., Jiang, J., Shollock, B. A., Britton, T. B., and Dunne, F. P. Slip localization and fatigue crack nucleation near a non-metallic inclusion in polycrystalline nickel-based superalloy. *Materials Science and Engineering: A*, 641: 328–339, 2015. ISSN 09215093. doi:10.1016/j.msea.2015.06.070.

[108] Zhang, T., Jiang, J., Britton, B., Shollock, B., and Dunne, F. Crack nucleation using combined crystal plasticity modelling, high-resolution digital image correlation and high-resolution electron backscatter diffraction in a superalloy containing non-metallic inclusions under fatigue. *Proceedings. Mathematical, physical, and engineering sciences*, 472(2189):20150792, 2016. ISSN 1364-5021. doi:10.1098/rspa.2015.0792.

[109] Zhu, S. P., Foletti, S., and Beretta, S. Evaluation of size effect in low cycle fatigue for q&t rotor steel. *Procedia Structural Integrity*, 7:368–375, 2017. ISSN 24523216. doi:10.1016/j.prostr.2017.11.101.

[110] Zhu, S.-P., Foletti, S., and Beretta, S. Evaluation of size effect on strain-controlled fatigue behavior of a quench and tempered rotor steel: Experimental and numerical study. *Materials Science and Engineering: A*, 735:423–435, 2018. ISSN 09215093. doi:10.1016/j.msea.2018.08.073.

[111] Zimmer, A., Vrana, J., Meiser, J., Maximini, W., Blaes, N., Thompson, D. O., and Chimenti, D. E. Evolution of the ultrasonic inspection of heavy rotor forgings over the last decades. In *AIP Conference Proceedings*, pages 1631–1638. AIP, 2010. doi:10.1063/1.3362264.

A. Size Distribution of DARWIN Data

UT indications are typically indications in the millimeter size scale. The Siemens Energy material database with all the UT inspections on rotor steel forgings was used to infer the TFS from KSR indications. Due to confidentiality reasons I may not publish those figures, but as comparison I will illustrate the similarity with inspection data on hard alpha anomalies in titanium alloys used in aero-engine disks. This data is available through the DARWIN program. The curves shown in Figure A.1a are exceedance rates over anomaly areas, just as extracted from DARWIN. They are produced from the same UT inspection data with 18 different PODs applied to them (see [1] for more details on the PODs).

POD curves typically start with values equal to zero for very small particles on the left — these particles are never detected — and grow to values close to one for large particles — which are basically always detected. For this reason, the 18 different curves from Figure A.1 collapse to the same line on the left hand and also on the right hand of the plot. In Figure A.1b the exceedance rates are converted into probability densities by taking the negative gradient of the exceedance. By fitting a power law function to the right tail of the curves — similar results would apply to the left tail, which is in fact parallel to the right tail — it is found that also those size distributions obey a power law with an exponent of -1.63, which is astonishingly close to the one found for the NMIs discussed in Section 3.5 and displayed in Figure 3.17.

Extrapolating such UT inspection results — that only apply to detectable indications in the millimeter scale — to the smaller scale, might be interesting to simulate LCF lives of materials initiating from small inclusions rather than from surface intrusion/extrusion mechanisms. However, this goes far beyond the scope of the present research and could be an interesting topic for further research.

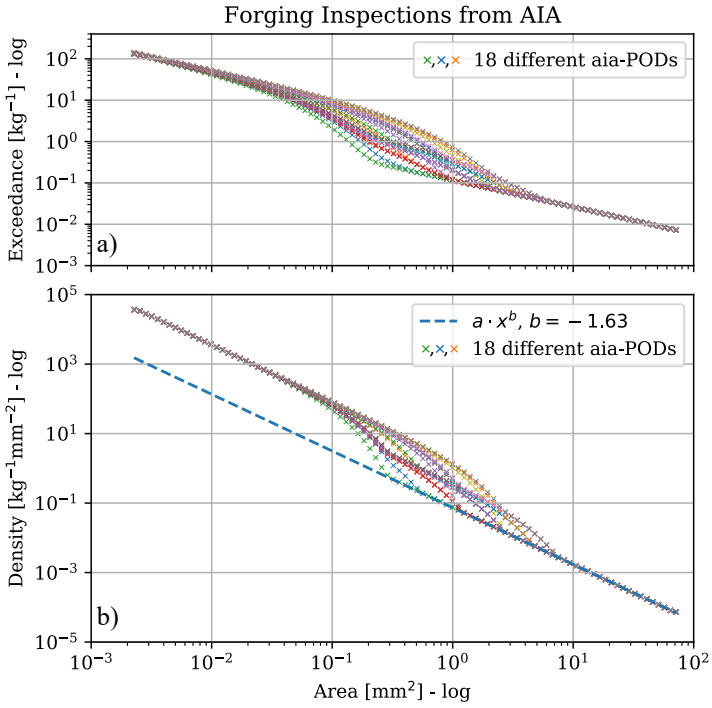

Figure A.1.: (a) Flaw size exceedance rates of hard alpha inclusions in titanium alloys as they are reported in the DARWIN program using a series of different PODs [1]. (b) Corresponding density plots inferred from the exceedance rate. The fitted line shows that the size distributions follow a power law with exponent $b = -1.6$.